Fakultät für Physik
Technische Universität München

Automation of Multi-Loop Amplitude Calculations

Stephan Jahn

Vollständiger Abdruck der von der Fakultät für Physik der Technischen Universität München zur Erlangung des akademischen Grades eines

Doktors der Naturwissenschaften (Dr. rer. nat.)

genehmigten Dissertation.

Vorsitzender:
Prof. Dr. Lothar Oberauer

Prüfende der Dissertation:
1. Hon.-Prof. Dr. Wolfgang F. L. Hollik
2. Prof. Dr. Andreas Weiler

Die Dissertation wurde am 28.11.2019 bei der Technischen Universität München eingereicht und durch die Fakultät für Physik am 17.01.2020 angenommen.

This Thesis is based on the author's work conducted at the Max Planck Institute for Physics (Werner-Heisenberg-Institut) in Munich from May 2015 until November 2019. Parts of this work have already been published or are in preparation for publication:

Refereed Research Papers

- L. Chen, G. Heinrich, S. Jahn, S. P. Jones, M. Kerner, J. Schlenk et al., *Photon pair production in gluon fusion: Top quark effects at NLO with threshold matching*, 1911.09314.
- S. Borowka, G. Heinrich, S. Jahn, S. P. Jones, M. Kerner and J. Schlenk, *A GPU compatible quasi-Monte Carlo integrator interfaced to pySecDec*, *Comput. Phys. Commun.* **240** (2019) 120 [1811.11720].
- G. Heinrich, S. Jahn, S. P. Jones, M. Kerner and J. Pires, *NNLO predictions for Z-boson pair production at the LHC*, *JHEP* **03** (2018) 142 [1710.06294].
- S. Borowka, G. Heinrich, S. Jahn, S. P. Jones, M. Kerner, J. Schlenk et al., *pySecDec: a toolbox for the numerical evaluation of multi-scale integrals*, *Comput. Phys. Commun.* **222** (2018) 313 [1703.09692].

Conference Proceedings

- S. Borowka, G. Heinrich, S. Jahn, S. P. Jones, M. Kerner and J. Schlenk, *Numerical Multi-loop Calculations: Sector Decomposition & QMC Integration in pySecDec*, published in A. Blondel et al., *Theory report on the 11th FCC-ee workshop*, 1905.05078.
- HL-LHC Collaboration and HE-LHC Working Group (P. Azzi et al.), *Standard Model Physics at the HL-LHC and HE-LHC*, 1902.04070.
- S. Jahn, *Numerical evaluation of multi-loop integrals*, *PoS* **LL2018** (2018) 019 [1811.11722].
- S. Jahn, *Integral symmetries with pySecDec*, *PoS* **CORFU2017** (2018) 132.
- S. Jahn, *SecDec: a toolbox for the numerical evaluation of multi-scale integrals*, *PoS* **RADCOR2017** (2018) 017 [1802.07946].
- S. Borowka, G. Heinrich, S. Jahn, S. P. Jones, M. Kerner and J. Schlenk, *Numerical evaluation of two-loop integrals with pySecDec*, *Acta Phys. Polon. Supp.* **11** (2018) 375 [1712.05755].
- S. Borowka, G. Heinrich, S. Jahn, S. P. Jones, M. Kerner and J. Schlenk, *Multi-loop calculations: numerical methods and applications*, *J. Phys. Conf. Ser.* **920** (2017) 012003 [1704.03832].
- S. Borowka, G. Heinrich, S. Jahn, S. P. Jones, M. Kerner, J. Schlenk et al., *Numerical multi-loop calculations: tools and applications*, *J. Phys. Conf. Ser.* **762** (2016) 012073 [1604.00267].

Abstract

Particles colliders like the Large Hadron Collider (LHC) allow insights to the fundamental laws of physics. Precision calculations for scattering processes beyond the one-loop order in perturbation theory are particularly important to profit from current and upcoming high-precision measurements at the LHC and future colliders.

We present various contributions to realize an automated multi-loop amplitude generator as well as its application in the context of precision calculations for hadron colliders. To be precise, we discuss the challenges and possible solutions when extending the public tree-level and one-loop amplitude generator GoSam to higher loop-orders. In particular, the partial implementation of an automated treatment of the Dirac matrix γ_5 in the context of dimensional regularization is introduced. We further describe the decomposition of a general amplitude into form factors which are the objects our amplitude generator computes.

We also describe the program pySecDec, a toolbox for the numerical evaluation of multi-scale integrals. pySecDec is a complete rewrite of the program SecDec designed to be most suitable for usage within amplitude calculations. We show how pySecDec is embedded in our amplitude generator to numerically evaluate the occurring master integrals in an optimized way. Recent developments in improving the numerical integration using Quasi Monte Carlo (QMC) lattice rules on Graphics Processing Units (GPUs) are also considered.

The automated tools are applied to compute the two-loop virtual correction to the process $gg \to \gamma\gamma$ including the full top-quark mass dependence. We further combine our calculation of the partonic NLO amplitude with the production via a $t\bar{t}$ bound-state close to the top-quark pair-production threshold in a non-relativistic quantum chromodynamics (NRQCD) framework. Distinct features of the diphoton invariant-mass distribution in the threshold region can be used for a precise determination of the top-quark mass.

We further study the inclusive production cross-section of a Z-boson pair at next-to-next-to-leading order (NNLO) in perturbative QCD. This process provides an important window to studies of the electroweak sector of the Standard Model and can be an important background to electroweak Higgs boson decays. For the NNLO infrared subtraction, we employ a recently developed scheme based on the N-jettiness variable.

Zusammenfassung

Teilchenbeschleuniger wie der "Large Hadron Collider"(LHC) erlauben Einblicke in die fundamentalen Gesetze der Physik. Präzisionsrechnungen für Streuprozesse über die Einschleifenordnung in Störungstheorie hinaus sind insbesondere wichtig um von aktuellen und zukünftigen hoch präzisen Messungen am LHC und zukünftigen Beschleunigern zu profitieren.

Wir präsentieren diverse Beiträge um einen Mehrschleifen-Amplitudengenerator zu realisieren, sowie dessen Anwendung im Kontext von Präzisionsrechnungen für Hadroncollider. Um genau zu sein: Wir diskutieren die Herausforderungen und mögliche Lösungen der Probleme, die sich bei der Verallgemeinerung des öffentlich zugänglichen Null- und Einschleifen-Amplitudengenerators GoSam zu höheren Schleifenordnungen ergeben. Insbesondere stellen wir die teilweise Implementierung einer automatisierten Behandlung der Dirakmatrix γ_5 im Kontext dimensionaler Regularisierung vor. Außerdem beschreiben wir die Zerlegung einer allgemeinen Amplitude in Formfaktoren, welches die Objekte sind, die unser Amplitudengenerator berechnet.

Auch beschreiben wir das Programm pySecDec, ein Werkzeugkasten zur numerischen Auswertung von Multiskalenintegralen. pySecDec ist eine komplette Neufassung des Programms SecDec, insbesondere konstruiert um in Amplitudenrechnungen eingesetzt werden zu können. Wir zeigen, wie pySecDec in unseren Amplitudengenerator zur optimierten Auswertung der auftretenden Masterintegrale eingebettet ist. Neue Entwicklungen zur Verbesserung der numerischen Integration unter Benutzung von quasi-Monte-Carlo (QMC) Gitterregeln auf Grafikprozessoren (Graphics Processing Units - GPUs) werden auch in Betracht gezogen.

Die automatisierten Werkzeuge werden zur Berechnung der virtuellen Zweischleifenkorrekturen zum Prozess $gg \to \gamma\gamma$ inklusive voller Topquark-Massenabhängigkeit angewendet. Desweiteren kombinieren wir unsere Rechnung der partonischen NLO-Amplitude mit der Produktion über einen gebundenen $t\bar{t}$-Zustand nahe der Top-Antitop-Quarkpaarproduktionsschwelle unter den Modellannahmen nichrelativistischer Quantenchromodynamik (NRQCD). Die besondere Struktur der invarianten Massenverteilung des Zweiphotonsystems in der Schwellenregion kann zur genauen Bestimmung der Topquarkmasse genutzt werden.

Zusätzlich untersuchen wir den inklusiven Produktionswirkungsquerschnitt eines Z-Bosonpaares zu 2. Ordnung (next-to-next-to-leading order (NNLO)) in perturbativer QCD. Dieser Prozess liefert wichtige Einblicke zur Untersuchung des elektroschwachen Sektors des Standardmodells und kann ein wichtiger Hintergrund zu elektroschwachen Zerfällen des Higgsbosons sein. Zur Infrarotsubtraktion wenden wir ein kürzlich entwickeltes, auf der N-jettinessvariable basierendes NNLO-Schema an.

Contents

Part I

Precision Calculations in Collider Physics

1 Introduction

High-energy particle collisions are a tool for studying the fundamental laws of nature. Currently, the most important facility is the Large Hadron Collider (LHC) located at CERN near Geneva in Switzerland. It is a proton-proton collider where the center-of-mass energy of the two protons has reached 13 TeV.

Particle physics at high-energy colliders is well described by the so-called Standard Model (SM) of particle physics. The Standard Model is a Quantum Field Theory (QFT) composed of the three lepton families $(\boldsymbol{\nu_\ell}, \boldsymbol{\ell})$, $\boldsymbol{\ell} = (e, \mu, \tau)$, the three generations of quarks $(\mathbf{u}, \mathbf{d})$, $\mathbf{u} = (u, c, t)$, $\mathbf{d} = (d, s, b)$, and the scalar Higgs doublet $\left(\phi^+, \phi^0\right)$, under the gauge group $SU(3)_c \times SU(2)_L \times U(1)_Y$. It combines the theory of the electroweak interaction [1–4], the Higgs mechanism [5–10], and Quantum Chromodynamics (QCD) - the theory of the strong interaction [11–14]. The representations of the fundamental fermion and Higgs fields in the Standard Model (see e.g. [15]) are listed in Table 1.1. The Higgs potential is constructed such that the Higgs field has a nonzero vacuum expectation value. Since this vacuum expectation value breaks three of the generators of the electroweak gauge group $SU(2)_L \times U(1)_Y$, three Goldstone bosons arise due to the Goldstone theorem [16, 17] (see also [18]) while the fourth scalar field is associated with the physical Higgs boson. The Goldstone bosons can be removed from the theory by a gauge transformation leading to longitudinal polarization-states for the three electroweak gauge bosons $W^\pm$ and Z^0 (denoted as Z boson in this Thesis), while the gauge boson of the electromagnetic force, the photon (sometimes denoted as γ), remains massless. The fermion mass terms arise from the Yukawa interaction terms. With its discovery in 2012 [19, 20], evidence for all elementary particles of the Standard Model has been established. The electric charge related to the symmetry group $U(1)_{\text{em}}$ after electroweak symmetry breaking is given by the Gell-Mann–Nishijima formula [21–23]

$$Q = I_3 + \frac{1}{2}Y, \tag{1.1}$$

where I_3 denotes the isospin of the gauge group $SU(2)_L$ and Y the hypercharge of the gauge group $U(1)_Y$.

Despite the good description of high-energy collisions, there are also phenomena that are left unexplained within the Standard Model. For example, it does not account for neutrino masses which would require terms involving right-handed neutrinos. Right-handed neutrino fields should however be included to explain e.g. the observation of neutrino oscillations. Another related and yet unsolved question is whether neutrinos are Majorana particles; i.e. whether they are their own antiparticles. A review of neutrino phenomenology is given in [24].

$SU(2)_L$	$\begin{pmatrix}\boldsymbol{\nu_\ell}\\ \boldsymbol{\ell}\end{pmatrix}_L$	$\boldsymbol{\ell}_R$	$\begin{pmatrix}\mathbf{u}\\ \mathbf{d}\end{pmatrix}_L$	$\mathbf{u}_R$	$\mathbf{d}_R$	$\begin{pmatrix}\phi^+\\ \phi^0\end{pmatrix}$
Y	-1	-2	$+\frac{1}{3}$	$+\frac{4}{3}$	$-\frac{2}{3}$	$+1$
$SU(3)_c$	$\mathbf{1}$	$\mathbf{1}$	$\mathbf{3}$	$\mathbf{3}$	$\mathbf{3}$	$\mathbf{1}$

Table 1.1: Representations of the fundamental fermion fields and the Higgs field in the Standard Model of particle physics. The first row denotes the doublets and singlets in the fundamental representation of the group $SU(2)_L$. The numbers in the second row denote the hypercharges Y. The last row denotes whether the fields transform as a triplet ($\mathbf{3}$) or as a singlet ($\mathbf{1}$) under the color group $SU(3)_c$.

Another issue is raised by the observation of gravitational effects which cannot be explained by only the visible matter. The proposal of additional so-called "dark matter" goes back to a publication in 1933 [25]. Today, it is still not clear how to extend the Standard Model such that dark matter is consistently included. Note that the Standard Model does not even provide a description of gravity and it is also not clear how to consistently include the gravitational force.

Within the Standard Model, the couplings of all charged leptons to the electroweak gauge bosons are the same. There are however hints from B-meson decays indicating a possible flavor universality violation [26–31] (see also e.g. [32, 33] and references therein).

Extensions of the Standard Model typically involve the introduction of new fields which manifest themselves at colliders as deviations from Standard-Model predictions and, if the collision energy is high enough, as new particles. A difficulty when implementing beyond-the-standard-model (BSM) particles is the so-called hierarchy problem. Since there is no direct evidence for BSM-particles from the LHC, such particles, if they exists, would likely have masses larger than $\Lambda \gtrsim 10$ TeV. The physical Higgs boson mass receives quantum corrections that are proportional to the mass of the heaviest particle in the theory which couples to the Higgs boson. Consequently, the physical Higgs boson mass would obtain corrections of $\mathcal{O}(\Lambda)$. This naively suggests $m_H^{\text{naive}} \approx \Lambda$ unless the there is a cancellation of multiple $\mathcal{O}(\Lambda)$ contributions such that the observed Higgs boson mass $m_H \approx 125$ GeV [34] is recovered. That can either be achieved by fine-tuning the parameters of the theory or by implementing mechanism which implies the cancellations.

Having mentioned some of the open questions on the one hand, we observe that the Standard Model of particle physics describes the collisions at LHC very well on the other hand. The idea of particle colliders is (i) to test the Standard Model prediction with experimental observations and (ii) to find further hints on how to extend it to describe yet unaccounted phenomena. To achieve these goals, precise theory calculations are becoming increasingly important to match the experimental accuracy, especially in view of the high-luminosity upgrade of the LHC (HL-LHC) [35], which will be installed by 2025. Increasing the precision of theory predictions is mainly governed by computing higher orders in a perturbative expansion of the full theory. The resulting mathematical

expressions become increasingly complicated with higher orders, in particular with the number of loops that have to be computed to reach the targeted order. Most of the nowadays important calculations could not be managed without advanced computer programs.

The computation of in principle any one-loop Standard-Model (and also many extensions) amplitude is solved in the sense that automated programs to compute physical cross-sections are publicly available. In addition to the calculation of the virtual loop correction, a next-to-leading order (NLO) calculation in general also requires renormalization of ultraviolet divergences and a subtraction scheme for infrared singularities. In this Thesis, we focus on the development of automated tools targeted to the computation of multi-loop virtual contributions and their applications in phenomenological studies.

This Thesis is structured as follows. The theoretical background is introduced in Part I. A mathematical description of proton collisions as occurring at the LHC is given in Chapter 2.

Part II is dedicated to the presentation of automated tools which implement routines needed to perform some of the steps in the calculations introduced in Part I. In particular, we present the programs GoSam and pySecDec. The public version of GoSam is a program that generates code to evaluate tree-level and one-loop partonic amplitudes for in principle any given partonic process. We summarize the existing public version and report on a private extension to higher loop-orders in Chapter 3. The program pySecDec numerically evaluates parameter integrals, such as Feynman parametrized loop-integrals, in the context of dimensional regularization. It is for example used to evaluate the master integrals in our aforementioned automated multi-loop amplitude generator. We summarize the program pySecDec in Chapter 4.

Phenomenological applications of the tools developed in Part II are presented in Part III. We present the calculation of the production of two photons in the gluon-fusion channel $gg \to \gamma\gamma$ with full top-quark mass dependence at NLO(QCD) in combination with an all-order resummation near the top-quark pair-production threshold in Chapter 5. Diphoton production is an important process at the LHC due to its large cross-section. The shape of the differential cross-section near the top-quark production threshold can serve a precise measurement of the top-quark mass and width. We further present a calculation of the inclusive cross-section for the production of two Z bosons in proton-proton collisions $pp \to ZZ$ at next-to-next-to-leading order (NNLO) in (QCD) in Chapter 6. This process is an important window to access the electroweak sector of the Standard Model and also an important background to Higgs boson studies.

We summarize the developments and results presented in this Thesis in Part IV.

2 Theoretical Framework for Hadron-Hadron Collisions

In this Chapter, we outline the theoretical framework to describe observations made at high-energy hadron colliders like the LHC, which is a proton-proton collider. We first summarize perturbative calculations involving only elementary particles in the final state with a focus on higher-order corrections in quantum chromodynamics (QCD) in Section 2.1. We then describe, in Section 2.2, how elementary particle scattering is embedded in a more complete description of the experiment where the final state consists only of particles which are long-lived enough to reach a detector.

2.1 Cross-Sections in Perturbation Theory

A hadron can be described as bound state of QCD with asymptotically free constituent particles - the *partons* (quarks q, antiquarks $\bar{q}$, and gluons g); i.e. for large momentum transfer, the partons can be considered as the degrees of freedom involved in the scattering process. The parton density functions (PDFs) $f_p(x)$ describe the probability to scatter with a certain type of parton $p \in \{q, \bar{q}, g\}$ with a certain fraction of the hadron momentum x. The differential cross-section to produce the final state X from a hadron collision is computed as the sum over all possible *partonic subprocesses*,

$$\mathrm{d}\sigma^X = \sum_{a,b} \int_0^1 \mathrm{d}x_a \int_0^1 \mathrm{d}x_b \; f_a(x_a) \; f(x_b) \; \mathrm{d}\hat{\sigma}^{ab\to X}(x_a P_A, x_b P_B), \tag{2.1}$$

where P_A and P_B denote the momenta of the initial hadrons, a and b denote the partons in the partonic initial state, $x_a, x_b \in (0, 1)$ denote the momentum fractions of the interacting partons such that $p_{a,b} \equiv x_{a,b} P_{A,B}$, the $f_{a,b}(x)$ denote the parton density functions (PDFs), and $\mathrm{d}\hat{\sigma}^{ab\to X}(x_a P_a, x_b P_b)$ denotes the partonic cross-section which is discussed in detail in the following. Note that the factorization in Equation (2.1) has corrections which are suppressed by the inverse of the momentum transfer. These corrections are therefore usually neglected in the context of high-energy collisions.

The differential cross-section of the process $a(p_a) + b(p_b) \to X^{(n)}(P_n) \equiv f_1(p_1) + ... + f_n(p_n)$ is computed as (see e.g. [15]),

$$\mathrm{d}\hat{\sigma}^{ab\to X^{(n)}} = \frac{(2\pi)^4 \, \delta^4(p_a + p_b - P_n)}{4\sqrt{(p_a \cdot p_b)^2 - m_a^2 m_b^2}} \; |\mathcal{M}_n|^2 \; \mathrm{d}\Phi_n, \tag{2.2}$$

with $P_n \equiv p_1 + ... + p_n$, the p_i denoting the four-momenta of the final-state particles f, the matrix element $\mathcal{M}_n$ (also called *scattering amplitude* or *hard matrix element*) computed e.g. in perturbation theory from Feynman diagrams, and the phase-space of the final-state particles

$$\mathrm{d}\Phi_n = \prod_{i=1}^{n} \frac{\mathrm{d}^3 p_i}{2\,(2\pi)^3\, p_i^0}. \tag{2.3}$$

The matrix element has a perturbative expansion in the coupling constants of the underlying theory. In this Thesis, we only consider quantum chromodynamics (QCD) corrections; i.e. higher-order terms in the strong coupling $\alpha_s \equiv g_s^2/4\pi$,

$$\mathcal{M}_n = \alpha_s^{n_\mathrm{B}/2} \left(\mathcal{M}_n^{(0)} + \alpha_s\, \mathcal{M}_n^{(1)} + \alpha_s^2\, \mathcal{M}_n^{(2)} + ... \right), \tag{2.4}$$

where n_B is the number of QCD-couplings g_s in the lowest-order amplitude. Computing the expansion of $\mathcal{M}_n$ with Feynman diagrams, each order involves diagrams with one more loop compared to the previous order. The lowest order is called *tree-level* if it has zero loops. A process where only diagrams with at least one loop contribute is called *loop-induced*.

In many cases, the leading-order (LO) approximation turns out to be inaccurate to describe LHC phenomenology. It is now standard to compute the hard matrix element to at least next-to-leading order (NLO) in the the strong coupling α_s, which involves the calculation of one-loop diagrams. In order to obtain a meaningful result, the partonic process with one extra particle in the final state $X^{(n+1)}$, the *real radiation*, has to be considered as well. Why different *multiplicities* have to be considered and the subtleties to properly define the final-state X in terms of n-particle final-states $X^{(n)}$ are explained in Section 2.1.3.

Making NLO standard is possible owing to fully automated tools; a summary in the context of presenting the one-loop provider (OLP) GoSam is given in Section 3.1. In the following, we discuss specific aspects and subtleties of higher-order calculations.

2.1.1 Dimensional Regularization

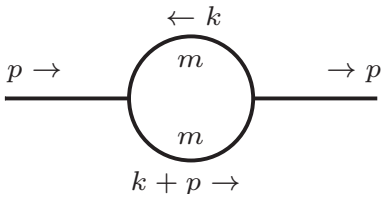

Figure 2.1: A one-loop bubble diagram with equal-mass propagators.

A higher-order calculation using the Feynman-diagram approach involves the calculation of loop integrals. These arise because the momentum of a propagator has to be integrated over, if it is not fixed by momentum conservation. Some loop integrals are naively divergent in four spacetime dimensions. Consider for example the scalar one-loop bubble with two equal mass propagators depicted in Figure 2.1,

$$\mathcal{I}_{\text{bub}} = \frac{1}{2\pi} \int_{-\infty}^{+\infty} \frac{\mathrm{d}^4 k}{(2\pi)^4} \frac{1}{[k^2 - m^2 + i\delta]\,[(k+p)^2 - m^2 + i\delta]}, \tag{2.5}$$

where p is the momentum going through the bubble, m is the mass of the particle running in the loop, k is the loop momentum, and the $i\delta$ is to be understood as the Feynman prescription that ensures causality of the propagator. The integral diverges in the ultraviolet (UV) limit $k^2 \to \infty$ as,

$$\mathcal{I}_{\text{bub}} \overset{k^2 \to \infty}{\sim} \lim_{\Lambda_\uparrow \to \infty} \int_{\Lambda_\downarrow}^{\Lambda_\uparrow} \mathrm{d}|k| \frac{|k|^3}{|k|^4} \sim \lim_{\Lambda_\uparrow \to \infty} \log(\Lambda_\uparrow), \tag{2.6}$$

where we have introduced the upper and lower cutoffs $\Lambda_{\uparrow,\downarrow}$. Loop integrals can also develop infrared (IR) singularities in the limit where the momentum of a massless propagator goes to zero. The massive bubble defined above, however, is infrared finite.

We could perform calculations with the cutoff parameters introduced above in the hope that they cancel in physical results. Unfortunately, such a regularization is neither Lorentz nor gauge invariant, which leads to violation of the Ward identities; i.e. it introduces cutoff dependent corrections to the gauge boson propagators which propagate longitudinal degrees of freedom.

In order to deal with these divergences, it is convenient to shift the spacetime dimension [36] from 4 to $4 - 2\varepsilon$, which modifies Equation (2.6) to

$$\mathcal{I}^{4-2\varepsilon}_{\text{bub}} \overset{k^2 \to \infty}{\sim} \int_{\Lambda_\downarrow}^{\infty} \frac{\mathrm{d}|k|}{|k|^{1+2\varepsilon}}. \tag{2.7}$$

If we assume $\varepsilon > 0$, then the integral converges in the ultraviolet limit $k^2 \to \infty$.

As mentioned earlier, loop integrals can also diverge in the infrared limit; i.e. in the limit where the momentum of a propagator goes to zero. To regularize the infrared limit by shifting the spacetime dimension, $\varepsilon < 0$ would be needed to make the integral converge. Although both conditions can obviously not be satisfied at the same time, it is still possible (and common practice) to simultaneously express both types of singularities as $1/\varepsilon$ poles. This works because IR-singularities can be regularized by adding nonzero masses to all propagators, while the UV-behavior of loop integrals can be described in terms of Euler Beta functions which have an analytic continuation via the complex plane to values of $\varepsilon < 0$. Therefore, the UV-poles can be calculated assuming $\varepsilon > 0$ and adding nonzero masses to all propagators. Then, the original integral (without the IR-regulating masses) can be computed assuming $\varepsilon < 0$ since the UV-behavior is already expressed in terms of its analytic continuation.

2.1.2 Renormalization of Ultraviolet Poles

The ultraviolet limit in momentum space corresponds to short-distance effects. An associated divergence arises e.g. in quantum electrodynamics because the elementary particles are treated pointlike which gives rise to a divergence in their field energy due to the Coulomb potential (see e.g. [18]). This divergence, however, does not lead to observable effects.

In practice, ultraviolet divergences are removed from physical observables by adding counterterms to the Lagrangian. In a renormalizable theory, the required counterterms take the same form as the terms already present in the unrenormalized Lagrangian such that subtraction of all singularities can be achieved by a redefinition of the *bare* model parameters and fields. For example, the renormalized QCD-Lagrangian reads (see e.g. [37])

$$\begin{aligned}
\mathcal{L}_{\text{QCD}} = &-\frac{1}{4} Z_A (\partial_\mu \boldsymbol{A}_\nu - \partial_\nu \boldsymbol{A}_\mu)^2 + i Z_q \bar{q} \boldsymbol{\partial\!\!\!/} q - Z_q Z_m \bar{q} m q + Z_\eta \partial_\mu \eta^\dagger \partial^\mu \eta \\
&+ Z_g Z_A^{\frac{3}{2}} \frac{g_s}{2} \mu_R^\varepsilon f^{abc} (\partial_\mu A_\nu^a - \partial_\nu A_\mu^a) A_b^\mu A_c^\nu + i Z_g Z_\eta Z_A^{\frac{1}{2}} g_s \mu_R^\varepsilon f^{abc} \eta_a^\dagger \partial_\mu A_b^\mu \eta_c \\
&- Z_g Z_q Z_A^{\frac{1}{2}} g_s \mu_R^\varepsilon \bar{q} \boldsymbol{A\!\!\!/} q - Z_g Z_A^2 \frac{g_s^2}{4} \mu_R^{2\varepsilon} f^{abc} f^{ade} A_b^\mu A_c^\nu A_\mu^d A_\nu^e + \mathcal{L}_{\text{gauge fix}}, \\
\boldsymbol{A}^\mu \equiv t_a A_a^\mu, &\quad \boldsymbol{\eta} \equiv t_a \eta_a,
\end{aligned} \tag{2.8}$$

where A_a^μ denotes the gluon field, the t_a denote the generators of the gauge group $SU(3)_c$ associated with color, q denotes the quark fields in fundamental representation of $SU(3)_c$, m denotes their mass matrix, μ_R is an arbitrary mass scale which is introduced to keep the coupling constant g_s dimensionless in the context of dimensional regularization, η denotes the Faddeev-Popov ghost field associated with the gluon field, $\mathcal{L}_{\text{gauge fix}} \equiv -\frac{1}{2\xi}(\partial^\mu \boldsymbol{A}_\mu)^2$ is the R_ξ gauge fixing term with the gauge parameter ξ, and the $Z_X = 1 + \delta Z_X$ are the renormalization constants which relate the bare (unrenormalized) parameters and fields to the physical ones as

$$g_{s0} = \mu_R^\varepsilon Z_g g_s, \quad m_0 = Z_m m, \quad \eta_0 = q_0 = Z_q^{\frac{1}{2}} q, \quad A_0^\mu = Z_A^{\frac{1}{2}} A^\mu, \quad Z_\eta^{\frac{1}{2}} \eta. \tag{2.9}$$

There is some freedom in the precise definition of the renormalization constants: In addition to the UV-singularities, also finite pieces can be subtracted which gives rise to multiple *renormalization schemes*. Commonly used schemes are the minimal subtraction (MS) scheme where only the UV-pole terms are subtracted, a modified version ($\overline{\text{MS}}$) which removes the commonly appearing factor $(1/\varepsilon + \log(4\pi) - \gamma_E)$ where γ_E is the Euler–Mascheroni constant, and the on-shell scheme where the real part of the resummed propagator's pole is defined to be at the physical mass and to have unit residue.

2.1.3 Cancellation of Infrared Poles

As opposed to the ultraviolet limit, the infrared limit corresponds to long-distance effects. Infrared divergences are classified into *soft* and *collinear* divergences. A soft

divergence can occur in the limit where a massless external-state particle approaches zero momentum. A collinear divergence can occur if the spatial momenta of two massless particles become collinear. States with an additional soft or collinear particle are indistinguishable from the state without it. This must be accounted for when computing physical observables by summing over all processes with indistinguishable external states. In experiments, the energy resolution and the spatial resolution of the detector set lower bounds to what extent multi-particle states are distinguishable. In case of strongly interacting particles (e.g. gluons) in the final state of the hard matrix element, the scale $\Lambda_{QCD} \approx 0.2\,\text{GeV}$ [38, 39] sets a lower limit to the validity of perturbative QCD. External QCD-particles are discussed in detail in Section 2.2.

The formal definition of an observable cross-section with fixed initial state and at least m external particles is

$$\hat{\sigma}^{ab\to X} = \sum_{n=m}^{\infty} \int \mathrm{d}\Phi_n \, \frac{\mathrm{d}\hat{\sigma}^{ab\to X^{(n)}}}{\mathrm{d}\Phi_n} \, F_n(p_a, p_b, p_1, ..., p_n), \tag{2.10}$$

where $X = \{X^{(m)}, X^{(m+1)}, ...\}$ is a set of final states that become indistinguishable in infrared limits, $\frac{\mathrm{d}\hat{\sigma}^{ab\to X^{(n)}}}{\mathrm{d}\Phi_n}$ is the n-particle cross-section defined in Equation (2.2), and the functions $F_n(p_a, p_b, p_1, ..., p_n)$ define an observable. The Kinoshita-Lee-Nauenberg (KLN) [40, 41] theorem ensures that in cross-sections as defined in (2.10) all final-state infrared divergences cancel if the observable is *infrared and collinear safe*; i.e. if the functions F_n defining the observable satisfy (see e.g. [42])

$$F_n(p_a, p_b, p_1, ..., p_i, ..., p_n) \xrightarrow{p_i \to 0} F_{n-1}(p_a, p_b, p_1, ..., p_{i-1}, p_{i+1}, ..., p_n), \tag{2.11}$$

$$F_n(p_a, p_b, p_1, ..., p_i, ..., p_j, ..., p_n) \xrightarrow{\vec{p}_i \to \vec{p}_j} F_{n-1}(p_a, p_b, p_1, ..., p_i + p_j, ..., p_n), \tag{2.12}$$

where $\vec{p}_i$ and $\vec{p}_j$ denote the three-momenta of the particles going collinear, and

$$F_m(p_a, p_b, p_1, ..., p_i, ..., p_j, ..., p_m) \xrightarrow{\vec{p}_i \to \vec{p}_j \text{ or } p_j \to 0 \text{ or } p_j \to 0} 0. \tag{2.13}$$

The remaining collinear singularities between final and initial state partons ($p_j = p_{a,b}$ in (2.12)) are absorbed by renormalizing the parton density functions using QCD factorization [43], such that the production cross-section of the final state X with hadronic initial states is calculated as

$$\begin{aligned}
\sigma^X &= \sum_{a,b} \int_0^1 \mathrm{d}x_a \int_0^1 \mathrm{d}x_b \;\; f_a^0(x_a) \;\; f_b^0(x_b) \;\; \hat{\sigma}^{ab\to X}(x_a P_A, x_b P_B, \mu_R^2), \\
&= \sum_{a,b} \int_0^1 \mathrm{d}x_a \int_0^1 \mathrm{d}x_b \;\; f_a(x_a, \mu_F^2) \;\; f_b(x_b, \mu_F^2) \\
&\qquad \{\hat{\sigma}^{ab\to X}(x_a P_A, x_b P_B, \mu_R^2) + \hat{\sigma}_C^{ab\to X}(x_a P_A, x_b P_B, \mu_R^2, \mu_F^2)\},
\end{aligned} \tag{2.14}$$

where f_a^0 and f_b^0 denote the bare parton density functions, P_A and P_A denote the four-momenta of the initial-state hadrons, $\hat{\sigma}^{ab\to X}$ denotes the cross-section with partonic initial states (see Equation (2.10)) which we refer to as the *partonic subprocesses*, and $\hat{\sigma}_C^{ab\to X}$ denotes a factorization-scheme dependent collinear counterterm which cancels the initial-state collinear divergences.

Note that the renormalized PDFs $f_p(x, \mu_F^2)$ depend on the factorization scale μ_F and also on a factorization scheme. The factorization scale μ_F conceptually describes the separation between *soft* and *collinear* splittings, which are considered as part of the hadron, and *hard* splittings, which are considered as part of the hard matrix element. It formally arises in the renormalization of the bare parton density functions similar to the occurrence of the renormalization scale μ_R in Section 2.1.2. The PDFs capture nonperturbative effects of the hadronic bound state below the scale Λ_{QCD}. It is nevertheless possible to perturbatively evolve them between different scales using the Dokshitzer-Gribov-Lipatov-Altarelli-Parisi (DGLAP) [44–46] equations.

Since a process with an extra external particle has a higher leading power of at least one coupling constant, only the first term in the sum of Equation (2.10) has to be considered to compute the cross-section to leading order (LO) in all couplings. We introduce the shorthand notation

$$\mathrm{d}\hat{\sigma}_{LO} \equiv \mathrm{d}\hat{\sigma}^{ab\to X^{(m)}}, \tag{2.15}$$

where the matrix element $\mathcal{M}_m$ is replaced by only the first term in Equation (2.4). Collecting all contributions at the next-to-leading order in the strong coupling α_s from Equation (2.10), we find the contributions at next-to-leading order (NLO) in α_s to be

(i) the tree-level contribution $\mathrm{d}\hat{\sigma}_{LO}$,
(ii) the real-radiation contribution

$$\mathrm{d}\hat{\sigma}_R \equiv \mathrm{d}\hat{\sigma}^{ab\to X^{(m+1)}}, \tag{2.16}$$

with an additional final-state parton and again taking only the first term of the perturbatively expanded matrix element $\mathcal{M}_{m+1}$, and
(iii) the (UV renormalized) virtual contribution

$$\mathrm{d}\hat{\sigma}_V \equiv \mathrm{d}\hat{\sigma}^{ab\to X^{(m)}}, \tag{2.17}$$

with the matrix element replaced by the second term in Equation (2.4).

Making the cancellation of singularities covered by the KLN theorem manifest is difficult because of the different phase-space of the individual contributions. At NLO, the singularities in the real contribution $\mathrm{d}\hat{\sigma}_R$ originate from the phase space integral with $m+1$ final-state particles while the singularities in the virtual contribution $\mathrm{d}\hat{\sigma}_V$ come from the loop integrals.

One possible solution is to introduce suitable *local* IR subtraction terms $\mathrm{d}\hat{\sigma}_A$, such that the partonic NLO cross-section can schematically be written as

$$\hat{\sigma}_{NLO} = \int_m \mathrm{d}\hat{\sigma}_{LO} + \int_{m+1} \left(\mathrm{d}\hat{\sigma}_R|_{\varepsilon=0} - \mathrm{d}\hat{\sigma}_A|_{\varepsilon=0}\right) + \left[\int_m \left(\mathrm{d}\hat{\sigma}_V + \int_1 \mathrm{d}\hat{\sigma}_A\right)\right], \tag{2.18}$$

where ε denotes the dimensional regulator and where we use the shorthand notation

$$\int_n \mathrm{d}\hat{\sigma}_\bullet \equiv \int \mathrm{d}\Phi_n \, \frac{\mathrm{d}\hat{\sigma}_\bullet}{\mathrm{d}\Phi_n}. \tag{2.19}$$

The differential subtraction terms $\mathrm{d}\hat{\sigma}_A$ should be chosen such that the one-fold integral $\int_1 \mathrm{d}\hat{\sigma}_A$ can be performed analytically. Then, the subtraction term can be used to render the $(m+1)$-parton phase-space integral finite in $D = 4$ dimensions and, at the same time, manifestly subtract the poles in the dimensional regulator ε from the virtual contribution. Note that the square bracket in Equation (2.18) is not finite and the remaining poles cancel against the collinear counterterm $\hat{\sigma}_C^{ab\to X}$. The subtraction term $\mathrm{d}\hat{\sigma}_A$ is not unique because it may contain an arbitrary finite contribution in addition to the infrared poles. The explicit definition of the subtraction terms defines a *subtraction scheme*. Common subtraction schemes include Catani-Seymour [42] and FKS (Frixione, Kunszt, Signer) [47, 48].

Another possibility is to separate ("slice") the real-radiation phase-space integral into a singular an a nonsingular region. If the singular integral can be computed or sufficiently well approximated analytically, then it can act as a *global* subtraction term for the virtual contribution. The NLO cross-section schematically reads

$$\hat{\sigma}_{NLO} = \hat{\sigma}_{LO} + \int_{\text{nonsingular}} \mathrm{d}\hat{\sigma}_R|_{\varepsilon=0} + \left[\int_{\text{singular}} \mathrm{d}\hat{\sigma}_R + \int \mathrm{d}\hat{\sigma}_V\right] \tag{2.20}$$

in that case. This method is presented in [49] for general NLO(QCD) calculations. An NNLO(QCD) slicing method for colorless final states is the so-called q_T-subtraction [50], which has been generalized to colored final-states in [51]. Recently, a slicing method was generalized to higher orders [52–55] where the phase-space is divided according to the N-jettiness variable [56, 57]. We apply this method in the calculation of the NNLO corrections to the process $pp \to ZZ + X$ as described in Section 6.3.

2.1.4 Dirac Algebra in Dimensional Regularization

The Dirac algebra,

$$2g^{\mu\nu} = \{\gamma^\mu, \gamma^\nu\} \equiv \gamma^\mu\gamma^\nu + \gamma^\nu\gamma^\mu, \tag{2.21}$$

has to be generalized to D dimensions when dimensional regularization is applied. The Lorentz indices have to be considered D dimensional such that

$$g^\mu_\mu = D. \tag{2.22}$$

Generalizing the four dimensional definition of γ_5,

$$\gamma_5 \equiv i\gamma^0\gamma^1\gamma^2\gamma^3 = \frac{i}{4!}\varepsilon_{\mu\nu\rho\sigma}\gamma^\mu\gamma^\nu\gamma^\rho\gamma^\sigma, \tag{2.23}$$

where $\varepsilon_{\mu\nu\rho\sigma}$ denotes the totally antisymmetric Levi-Civita tensor, to D dimensions is not straightforward. It can be shown (see e.g. [58]) that there is no $D \neq 4$ dimensional

generalization of γ_5 which simultaneously maintains the properties

$$\gamma_5^2 = \mathbb{1}, \tag{2.24}$$
$$\{\gamma^\mu, \gamma_5\} = 0, \tag{2.25}$$

and cyclicity of the trace such that the four-dimensional relation

$$\mathrm{Tr}\left(\gamma_\mu\gamma_\nu\gamma_\rho\gamma_\sigma\gamma_5\right) = 4i\varepsilon_{\mu\nu\rho\sigma}, \tag{2.26}$$

is recovered in the limit $D \to 4$: If we use cyclicity of the trace and either (2.21) or (2.25) to bring γ_τ and γ^τ next to each other in the expression

$$\kappa^{\mu\nu\rho\sigma}\mathrm{Tr}\left(\gamma_\tau\gamma_\mu\gamma_\nu\gamma_\rho\gamma_\sigma\gamma^\tau\gamma_5\right), \tag{2.27}$$

with $\kappa^{\mu\nu\rho\sigma}$ some tensor which is zero when two indices are equal, then we find

$$(D-4)\,\kappa^{\mu\nu\rho\sigma}\mathrm{Tr}\left(\gamma_\mu\gamma_\nu\gamma_\rho\gamma_\sigma\gamma_5\right) = 0 \tag{2.28}$$

after simplifying $\gamma_\tau\gamma^\tau = D$ as implied by (2.21) and (2.22).

In order to deal with γ_5 in this work, we follow the scheme suggested in [59] which is equivalent to the schemes described in [36, 60] but avoids the explicit splitting of Lorentz indices into 4 and $D-4$ dimensional components: The four-dimensional definition of γ_5 as denoted in the last term of (2.23) is maintained also in D dimensions. The contraction with the Levi-Civita tensor, however, is formally only performed *after* renormalization while the Gamma algebra is carried out in D dimensions. In addition, all occurrences of $\gamma^\mu\gamma_5$ in the Lagrangian have to be replaced by $\frac{1}{2}\left(\gamma^\mu\gamma_5 - \gamma_5\gamma^\mu\right)$ which is equivalent to removing the $(D-4)$ dimensional γ^μ-matrices from $\gamma^\mu\gamma_5$. Without this modification, the free Fermion propagator maintains its four-dimensional form such that Fermion loops are not regularized [58].

The four-dimensional anticommutator relation in (2.25) generalizes to

$$\begin{aligned} \{\gamma^\mu, \gamma_5\} &= 0 \quad \mu \in \{0,1,2,3\} \\ [\gamma^\mu, \gamma_5] &= 0 \quad \text{otherwise,} \end{aligned} \tag{2.29}$$

where $[\gamma^\mu, \gamma_5] \equiv \gamma^\mu\gamma_5 - \gamma_5\gamma^\mu$ denotes the commutator. The axial Ward identities are broken in this scheme due to the non-anticommuting γ_5, which is fixed by an additional finite renormalization of the axial current.

2.2 Event Simulation

Hadron collisions involve physics at many scales. Different approximations with limited ranges of validity are required for a full description. In particular in the case of strongly interacting particles in the final state of the hard process, further processing is needed for a full description of an event consisting only of particles long-lived enough to be detectable in an experiment. In this Chapter, we describe the ingredients for a Monte

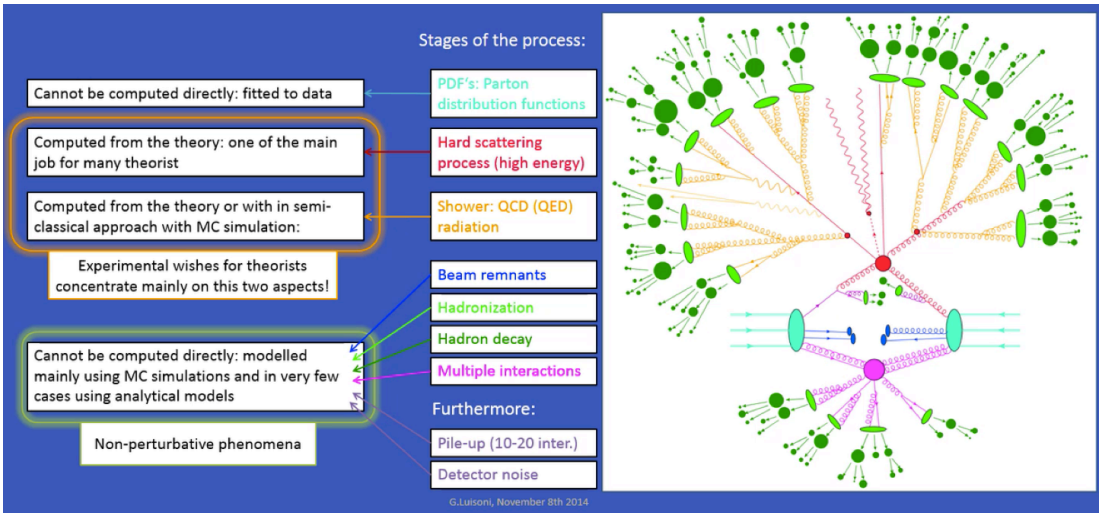

Figure 2.2: Schematic picture of a Proton-Proton collision. *Figure by Gionata Luisoni*

Carlo event generator from two initial protons to the particles entering a detector. A possible event is shown schematically in Figure 2.2.

The main ingredient to describe hadron collisions is the partonic cross-section, also referred to as hard matrix element. It describes the scattering of two partons, the constituent particles of the hadron, to a partonic final state. A detailed discussion is given in Section 2.1.

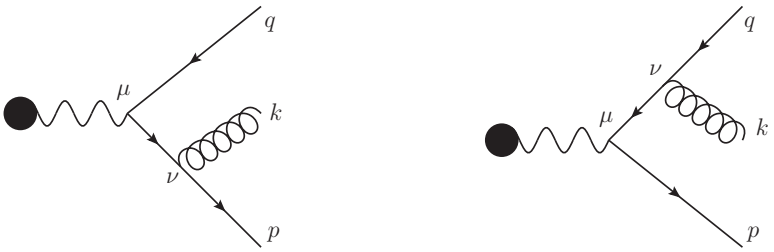

Figure 2.3: Feynman diagrams describing quark-antiquark production from a virtual vector boson (indicated by the blob connected to the quark line) in association with a gluon. $\mathcal{M}^{\mu\nu}_{V,q\bar{q}g}$ corresponds to the quark line in these diagrams with the vector bosons stripped off and ignoring color.

Another important ingredient is the so-called *parton shower* which we explain in the following. Consider for example the matrix element of quark-antiquark production

associated with a gluon from a virtual vector boson $V^\star$ as depicted in Figure 2.3,

$$\begin{aligned}\mathcal{M}^{\mu\nu}_{V,q\bar{q}g} =&\bar{u}(p)\gamma^\nu \frac{\not{p}+\not{k}-m}{(k+p)^2-m^2}\gamma^\mu v(q) + \bar{u}(p)\gamma^\mu \frac{\not{q}-\not{k}-m}{(k+q)^2-m^2}\gamma^\nu v(q)\\ =&\bar{u}(p)\gamma^\nu \frac{\not{p}+\not{k}-m}{2k^0p^0(1-\beta_p\cos\theta_{kp})}\gamma^\mu v(q) + \bar{u}(p)\gamma^\mu \frac{\not{q}-\not{k}-m}{2k^0q^0(1-\beta_q\cos\theta_{kq})}\gamma^\nu v(q)\end{aligned} \tag{2.30}$$

where k is the four-momentum of the gluon, p and q denote the four-momenta of the quark and the antiquark, θ_{kq} and θ_{kp} are the angles between the three-momenta of the gluon and the (anti-)quark respectively, and

$$\beta_l \equiv \sqrt{1-\frac{m^2}{(l^0)^2}}, \quad l \in \{q,p\}.$$

The differential cross-section of the process $V^\star \to q(p)+\bar{q}(q)+g(k)$ is computed from the phase-space integral over the spin-summed squared matrix according to Equation (2.2). That calculation is discussed in great detail in e.g. [39]. As can already be guessed from (2.30), the phase-space integral is (logarithmically) divergent where the divergence comes from the limit where the gluon becomes soft ($k^0 \to 0$) and, if the quark is massless, from the limit where it becomes collinear with the radiating quark line ($\theta_{kp} \to 0$ or $\theta_{kq} \to 0$). Since our example process can be seen as the real-radiation contribution to the process $V^\star \to q(p) + \bar{q}(q)$, the infrared divergences would cancel against the virtual correction to that process as discussed in Section 2.1.3. Yet, the probability to radiate additional soft or collinear gluons can be large and should be taken into account for an accurate description.

Considering multiple gluon emissions in the soft-collinear limit and summing the leading logarithmic terms to all orders gives a finite expression which can be taken as an approximation of the splitting probability. That expression can be used to formulate the non-emission probability between the two scales μ_0 and μ_1 which is known as the Sudakov Form Factor [61],

$$\Delta(\mu_0,\mu_1) = \exp\left(-\int_{\mu_0}^{\mu_1} \mathrm{d}t\, P(t)\right), \tag{2.31}$$

where $P(t)$ is the probability density of an emission at the scale t. The term *scale* corresponds to off-shellness of the propagator of the radiating particle. Similarly, an electromagnetic shower should be attached to electrically charged final-state particles and photons. The decays of Higgs bosons, electroweak gauge bosons, and massive quarks are usually considered within the hard matrix element such that only massless quarks, gluons, photons, and leptons enter into the shower evolution.

Modern parton shower algorithms usually consider one emitter particle while a second *spectator* particle takes the recoil to ensure both, momentum conservation and on-shellness, at the same time in every splitting. The parton shower evolution amounts to

estimating effects of higher perturbative order than the hard matrix element in soft and collinear regions of phase-space. Fixed-order calculations are unreliable in these regions due to large logarithms appearing at all orders which are effectively resummed by the parton shower evolution. Special care has to be taken to avoid double counting when matching a higher-order calculation of the hard matrix element with a shower. Two standard methods exist at NLO: (i) The MC@NLO [62] method, where the shower is performed separately on the (IR subtracted) real radiation and Born-plus-virtual matrix elements. (ii) The POWHEG [63, 64] method, where the first emission in the shower is performed using the full real-radiation matrix-element rather than its soft-collinear approximation. No generic method to match a parton shower to a partonic NNLO calculation is currently known.

However, perturbation theory of the strong interaction is no longer valid below the scale $\Lambda_{QCD} \approx 0.2\,\text{GeV}$ [38, 39]. The parton shower picture therefore only makes sense down to approximately that scale. Below Λ_{QCD}, empiric hadronization models are applied to describe the formation of primary hadrons that decay to the final hadrons which can be detected. For phenomenological studies, however, it is common practice to omit modeling the hadronization. That is motivated as follows: If the focus lies on inclusive observables; i.e. observables with an arbitrary distribution of quarks and gluons in the final state, then the hadronization should have no effect. Exclusive observables involving strongly interacting particles are typically defined in terms of *jets*. Forming a jet, which is defined by a jet clustering algorithm, essentially amounts to undoing the hadronization and showering such that a few hard partons are constructed out of many soft and collinear particles. A jet clustering algorithm iteratively replaces the two closest (according to some metric) particles by a parent particle with a momentum equal to the sum of the four-momenta of the parent particles. Note that this procedure does not lead to an exact on-shell hard parton as generated in the hard matrix element. It is therefore common practice to attach a parton shower to the hard matrix element and then to run a jet clustering algorithm on the showered events. The parton shower can also modify inclusive observables such as invariant-mass or momentum distributions of stable particles due to the modified phase space by the emission of additional particles. Computing the hard matrix element to higher orders, however, also takes these effects into account due to the additional real-radiation contributions.

In addition to the primary process, interactions of the remnants of the initial hadrons form the so-called underlying event.

Part II

Tools for Automated Multi-Loop Calculations

3 The Program GoSam

While the generation of one-loop amplitudes is already automated to a large extent, also in the context of extensions to the Standard Model, two-loop calculations are currently dealt with on a case-by-case basis. There are, however, many automatable steps in multi-loop calculations such that at least a partially automated two-loop amplitude generator seems possible. The organization of this Chapter is as follows: We summarize the workflow of the public one-loop provider GoSam in Section 3.1. Section 3.2 is dedicated to our extension of the program beyond the one-loop order.

3.1 One Loop Order

The public one-loop version of GoSam [65, 66] is a computer program written in multiple programming languages that generates `FORTRAN` code for tree and one-loop level amplitudes in the context of the Standard Model and beyond. We briefly summarize its workflow and how it can be used in the context of phenomenological studies in this section.

An *input card* defines the model (builtin or external Universal FeynRules Output (UFO) [67] or external LanHEP [68]), a partonic initial state, a partonic final state, and the type of correction (e.g. QCD or EW). GoSam calls QGRAF [69] to generate the contributing Feynman diagrams. The Feynman rules defined by the model are inserted using `FORM` [70–74]. The unreduced amplitude is written in terms of spinor products using the `FORM`-package `spinney` [75] and saved as optimized `FORTRAN` code using either the program `haggies` [76] or the code optimization in `FORM` [73]. The reduction of the amplitude to a set of scalar master integrals is done numerically using the techniques developed in [77–80] as implemented in the libraries Golem95C [81–83], Samurai [84, 85], Ninja [86–88], or PJFry [89, 90]. The master integrals are evaluated using OneLOop [91], Golem95C, or `QCDloop` [92, 93]. The workflow described in this paragraph is summarized in Figure 3.1.

GoSam has to be combined with an NLO-capable Monte Carlo event generator for phenomenological studies. Relevant tools include `GenEvA` [94, 95], `HELAC-NLO` [96, 97], `Herwig` [98, 99], `MadGraph5_aMC@NLO` [100], the `POWHEG BOX` [63, 64, 101], `PYTHIA8` [102], `Sherpa` [103], `VINCIA` [104], and `WHIZARD` [105, 106]. In combination with a Monte Carlo event generator, GoSam acts as a *one-loop provider* (OLP); i.e. it provides the virtual loop-tree interference contributions. Other one-loop providers include BlackHat [107], `FeynArts` [108, 109], `MadLoop` [110], `OpenLoops` [111], and `Recola` [112, 113]. There are also event generators with a supplemented NLO process library; i.e. a collection of NLO amplitude codes for predefined processes. Such projects include the `POWHEG BOX` [63, 64, 101], `VBFNLO` [114–116], and `MCFM` [117–119]. The Monte Carlo program

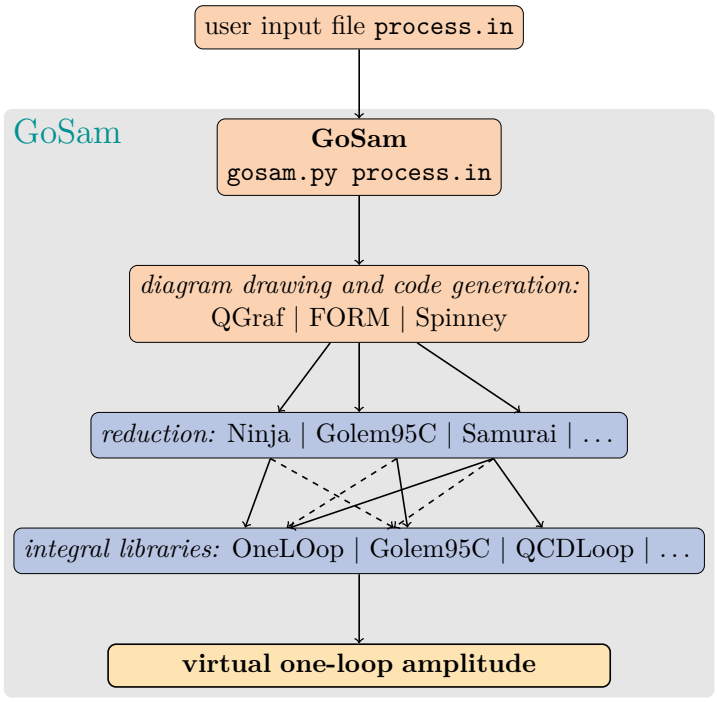

Figure 3.1: Workflow of the public one-loop version of the program GoSam. Figure taken from [66].

provides the tree-level contribution, the real radiation, a framework for the infrared subtraction, and a phase-space integrator. The events generated in this way can, depending on the Monte Carlo program, optionally be combined with a parton shower and hadronization. As already suggested by the term "one-loop provider", it provides the (renormalized) one-loop corrections to the process under consideration. This interplay is visualized in Figure 3.2. The interface between Monte Carlo programs and one-loop providers has been standardized in the Binoth Les Houches Accord (BLHA) [120, 121] to allow for easy combination of any MC with any OLP.

3.2 Extension Beyond One Loop Order

In the following, we describe our extension of the program GoSam beyond one-loop order. We begin, in Section 3.2.1, with a summary of the new challenges to be addressed for calculations beyond the one-loop order. Input and workflow of our multi-loop amplitude generator are summarized in Section 3.2.2. Subsequent sections are dedicated to explain the individual steps of the calculation in more detail. In particular, we point out the processing of the diagrams in Section 3.2.3, summarize Laporta's integration-by-parts (IBP) reduction algorithm [122] in Section 3.2.4, and comment on the numerical

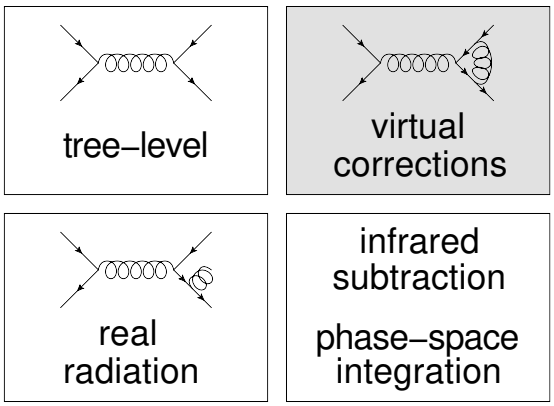

Figure 3.2: Visualization of the basic ingredients for NLO event generation. The Monte Carlo program (fields with white background) provides the Born (tree-level) amplitude, the real radiation corrections and a framework for the infrared subtraction as well as the phase-space integration, while the one-loop provider (field with gray background) provides the Born-virtual interference.

evaluation of the amplitude in Section 3.2.5. A summary of the program is shown in Figure 3.3.

3.2.1 Challenges

The highly automated evaluation of one-loop amplitudes was made possible by the reduction methods developed in [77–80]. All one-loop integrals appearing in the amplitude can be related and expressed as a linear combinations of a small ($\sim$30) set of process-independent so-called *master integrals*. Since the set of master integrals is known, highly optimized routines for the numerical evaluation of the master integrals and for finding the coefficients of the master integrals when expressing the amplitude as a linear combination of them can be developed.

A complete set of master integrals is currently not known for generic amplitudes beyond the one-loop level. Therefore, the first step after processing the diagrams is usually running Laporta's algorithm [122] to reduce the number of integrals to be computed. Using Laporta's approach raises two issues with the processing of the diagrams as done in the one-loop program. First, Laporta's algorithm requires all numerators to be expressed as D-dimensional inverse propagators. Therefore, dimension splitting as implemented in the one-loop code using `spinney` can no longer be applied to simplify the spinor traces. Second, in a one-loop integral, all scalar products involving the loop momentum and external momenta along the loop can be expressed in terms of the naturally appearing propagators of the loop. In contrast, starting from the two-loop level, the occurring propagators are in general insufficient to express all scalar products involving at least one loop momentum. The set of appearing propagators has to

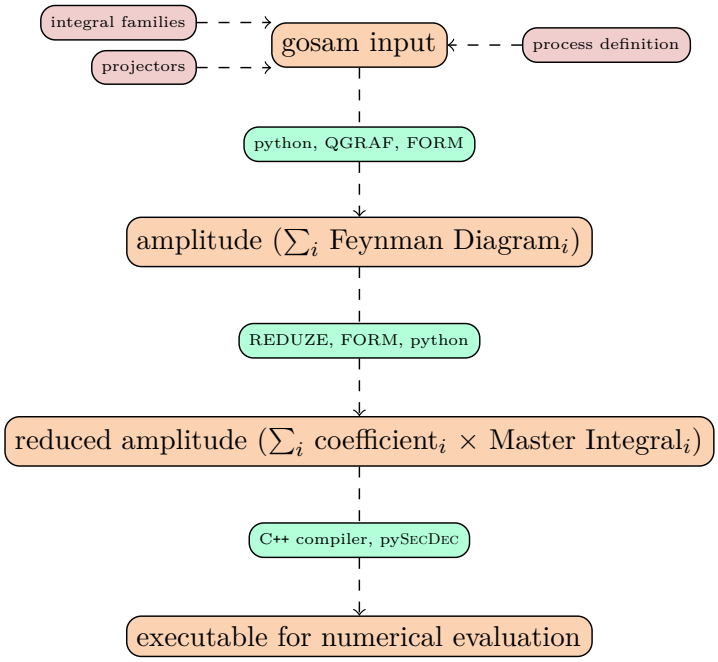

Figure 3.3: Workflow of the multi-loop extension of the program GoSam.

be extended to form an *integral family*; i.e. a list of propagators such that all scalar products can be expressed as linear combinations of them. The choice of *auxiliary* propagators is not unique and can decide whether the reduction to or evaluation of the master integrals is feasible or not. The same applies for the master integrals, which also leave some freedom of choice.

The next issue is how to obtain solutions for the master integrals. It is usually desirable to have analytic representations without left-over integrations of the master integrals for several reasons. First, analytic results are often orders of magnitude faster to numerically evaluate than a numerical integration and usually give more stable and more accurate results. Second, knowing an analytic expression for the amplitude eases studying analytical properties of the amplitude such as symmetries or kinematic limits.

On the one hand, new insights in the analytical structure of loop integrals are currently being explored, for example using the method of differential equations [123–129]. Currently, an important research aspect is how to choose the master integrals such that analytical solutions are feasible. However, analytical approaches beyond one-loop are currently not fully automated and therefore not (yet) suitable for automated amplitude generators. It may nevertheless be possible in the near future to automatically include known analytical solutions for at least some of the required integrals by looking them up in a public database. The idea of searching public articles by Feynman graphs rather

than conventional keys like author(s), title, year, etc. already led to the development `Loopedia` [130].

On the other hand, numerical and seminumerical methods are highly automatable and public tools which can numerically compute loop integrals are available. In practice, the choice of basis is, however, critical for numerical and analytical approaches alike. Unfortunately, integrals with helpful properties for analytical approaches are often suboptimal for numerical methods. Finite master integrals [131–133] have been found to be a particularly good choice [134] in combination with the sector decomposition approach [135, 136]. Other (semi-)numerical methods include direct numerical integration [137], numerical extrapolation [138], numerical differential equations [139], and the Mellin-Barnes approach [140–144]. A review of (semi-)numerical techniques is given in [145]. Recently, sector decomposition has been combined with analytic integration of approximated integrands obtained by Taylor expansions [146].

3.2.2 User Input and Workflow

The user input consists of a runcard defining the process similar to the runcards used in the one-loop version, a set of integral families, and a list of projection operators. The key concepts concerning the input are described in this section. Details about input files, syntax, and invocation of GoSam are given in Appendix A.

The structure of the runcards is mostly equivalent to the ones used in the public one-loop version of GoSam. It defines the external states of the process, the perturbative orders to be computed, and some technical details like e.g. the output directory. The main new feature is the extension of the `order` option to higher loop orders.

The integral families have to be chosen such that all appearing diagrams can be matched to at least one family; i.e. it should be possible to find a momentum routing for each diagram such that there is at least one integral family which contains the resulting propagators. We require the integral families as input because the choice of auxiliary propagators is critical for feasibility but we are not aware of an algorithm to automatically generate useful ones.

To understand the projectors, remember that a general amplitude with v external vector particles, f external fermions, and possibly external scalar particles takes the form

$$\begin{aligned}\mathcal{M}(p_1,...,p_v,q_1,...,q_f) = w(q_1)\dots w(q_f)\ \mathcal{A}^{\mu_1\dots\mu_v}_{i_1\dots i_f}(p_1,...,p_v,q_1,...,q_f)\ \epsilon^{(*)}_{\mu_1}(p_{v_1})\dots\epsilon^{(*)}_{\mu_v}(p_v),\\ w(q_f)\in\{\bar{u}(q_j),u(q_j),\bar{v}(q_j),v(q_j)\},\end{aligned} \tag{3.1}$$

where the p_j denote the momenta of the vector particles, the $\epsilon_{\mu_j}(p_j)$ denote the corresponding polarization vectors, the q_j denote the fermion momenta, and the $w(q_f)$ denote the Dirac spinors; i.e. the solutions of the Dirac equation in momentum space. The amputated amplitude $\mathcal{A}^{\mu_1\dots\mu_v}_{i_1\dots i_f}(p_1,...,p_v,q_1,...,q_f)$ can be decomposed into a finite process-dependent set of linear independent tensors $\mathcal{T}_j$,

$$\mathcal{A}^{\mu_1\dots\mu_v}_{i_1\dots i_f}(p_1,...,p_v,q_1,...,q_f) = \sum_j a_j \mathcal{T}_j{}^{\mu_1\dots\mu_v}_{i_1\dots i_f}, \tag{3.2}$$

where the a_j are scalar *form factors*. Our program is designed to compute user-defined contractions of the amplitude such that

$$\mathcal{P}_j{}^{i_1\ldots i_f}_{\mu_1\ldots\mu_v}(p_1,...,p_v,q_1,...,q_f)\ \mathcal{A}^{\mu_1\ldots\mu_v}_{i_1\ldots i_f}(p_1,...,p_v,q_1,...,q_f) \equiv a_j, \tag{3.3}$$

where the $\mathcal{P}_j$ are user-defined *projection* operators. The ultimate goal would be to automatically generate helicity amplitudes (or something similar) like at the one-loop order. However, using the spinor-helicity formalism like in the one-loop setup relies on dimension splitting which cannot be applied straightforwardly in combination with D-dimensional integration-by-parts (IBP) reduction. We have not been able to find a practical and fully automatable solution to this problem yet. For now, we require the user to provide the projection operators $\mathcal{P}_j$ for the given process. The set of relevant Lorentz structures can be reduced by removing structures transverse to the momentum of an external vector particle; i.e. by imposing the Ward identity

$$p_{j\,\mu_j}\ \mathcal{A}^{\mu_1\ldots\mu_j\ldots\mu_v}_{i_1\ldots i_f} = 0. \tag{3.4}$$

However, special care has to be taken when constructing projection operators for the remaining tensor structures because (3.4) in general only holds if the other indices are contracted with transverse momenta for non-abelian gauge bososons. Fixing a gauge of external massless vector particle allows for further reduction by imposing transversality as in (3.4) not only to the momentum p_j but also to another momentum of the problem. Examples of projectors for the processes studied in this Thesis are provided in Part III.

3.2.3 Processing of the Diagrams

The Feynman diagrams are generated with QGRAF using the same model files as for the one-loop version. Also the routines that insert the Feynman rules diagram-by-diagram are recycled from the one-loop program. Fermion traces, however, are no longer treated within the spinor-helicity formalism. Instead, the open indices of the amputated amplitude are contracted with the projection operators and the resulting spinor traces are reduced to scalar products following the procedure suggested in [147]:

(i) Replace the chiral projectors by their definitions in terms of γ_5,

$$P_{\substack{L\\R}} = \frac{1}{2}(\mathbb{1} \mp \gamma_5). \tag{3.5}$$

(ii) Replace γ_5 according to [59]

$$\gamma_5 = \frac{i}{4!}\varepsilon_{\mu\nu\rho\sigma}\gamma^\mu\gamma^\nu\gamma^\rho\gamma^\sigma. \tag{3.6}$$

A shortcut is applied to axial vertices,

$$\frac{1}{2}\left(\gamma^\mu\gamma_5 - \gamma_5\gamma^\mu\right) = \frac{i}{3!}\varepsilon^{\mu\nu\rho\sigma}\gamma_\nu\gamma_\rho\gamma_\sigma, \tag{3.7}$$

for performance reasons [147].

(iii) Contract pairs of the Levi-Civita tensor using

$$\varepsilon^{\mu\nu\rho\sigma}\,\varepsilon_{\alpha\beta\kappa\lambda} = \det\begin{pmatrix} \delta^\mu_\alpha & \delta^\mu_\beta & \delta^\mu_\kappa & \delta^\mu_\lambda \\ \delta^\nu_\alpha & \delta^\nu_\beta & \delta^\nu_\kappa & \delta^\nu_\lambda \\ \delta^\rho_\alpha & \delta^\rho_\beta & \delta^\rho_\kappa & \delta^\rho_\lambda \\ \delta^\sigma_\alpha & \delta^\sigma_\beta & \delta^\sigma_\kappa & \delta^\sigma_\lambda \end{pmatrix}, \tag{3.8}$$

which is conveniently built into FORM as the contract command. It has been pointed out [147] that particular pairs of epsilon tensors must be formed if there are products of more than two Levi-Civita tensors. This issue is not addressed in our preliminary version of the program yet. It is, however, not important for the processes considered in this Thesis because there only products of at most two Levi-Civita tensors can appear.

(iv) Reduce the traces, which are now free of γ_5, to scalar products using only D-dimensional relations. An automated renormalization procedure, and therefore also the additional finite renormalization as required by the Larin scheme [59], is currently not implemented yet.

We rely on the external program Reduze 2 [148] to match each diagram to one of the input integral families. The scalar products are rewritten in terms of inverse propagators of the integral family the diagram was matched to. We currently rely on Reduze 2 to generate substitution rules for the scalar products as well.

The amplitude after processing of the Feynman diagrams as described above gives rise to expressions for the form factors of the form

$$a_j = \sum_k c_{jk}\mathcal{I}_k, \tag{3.9}$$

where the c_{jk} are rational polynomials in the kinematic invariants and the dimensional regulator, and the $\mathcal{I}_k$ are scalar loop integrals of the form

$$\int \mathrm{d}^D k_1 \ldots \mathrm{d}^D k_l \; \frac{1}{P_1^{\nu_1}\ldots P_n^{\nu_n}}, \tag{3.10}$$

where D is the spacetime dimension, the $k_1, \ldots, k_l$ are the loop momenta, and the $P_1, \ldots, P_n$ are quadratic propagators with their associated (possibly negative) powers $\nu_1, \ldots, \nu_n$.

3.2.4 Integration by Parts (IBP) Reduction

The integrals $\mathcal{I}_k$ in Equation (3.9) are not all independent such that the amplitude can in general be written in terms of fewer integrals. GoSam relies on the the integral *reduction* program Reduze 2 [148], the successor of Reduze [149], to find a representation in terms of the linear independent *master integrals*. Reduze is an implementation of Laporta's algorithm [122] which we briefly review in the following. Other public implementations of Laporta's algorithm include AIR [150], FIRE [151–154], LiteRed [155, 156], and Kira [157, 158].

The idea of Laporta's algorithm is to generate and partially solve a linear system of integration-by-parts (IBP) identities [159, 160]

$$0 = \int \mathrm{d}^D k_1 \ldots \mathrm{d}^D k_l \; \frac{\partial}{\partial k^\mu} \, q^\mu \, \frac{1}{P_1^{\nu_1} \ldots P_n^{\nu_n}}, \tag{3.11}$$

where q^μ is a loop or an external momentum. Working out the derivatives leads to a linear system of equations relating integrals of the form (3.10). By defining a metric considering simplicity of the integrals, one can attempt to triangulate the system using Gaussian forward elimination. Since loop integrals do typically not evaluate to rational polynomials, the triangulation is only possible up to a basis set of integrals - the master integrals. After application of Gaussian backsubstitution, all non-master integrals in the amplitude, and therefore also the amplitude itself, can be expressed as a linear combination of only the master integrals.

Our current implementation expresses the amplitude in terms of the master integrals which `Reduze` chooses by default. Alternatively, the user can provide a reduction obtained in a different way, which turns out to be necessary in cutting-edge problems: As already mentioned in Section 3.2.1, the master integrals are not unique and their choice is crucial for the success of further attempts to evaluating them. It has been pointed out [134] that finite master integrals [131–133] are a particularly good choice when pursuing numerical evaluation with the sector decomposition approach. We additionally find that integrals with a mass dimension close to zero should be preferred. That is because the mass dimension translates into the unregulated exponent of the second Symanzik polynomial $\mathcal{F}$, which contains all poles in the interior of the integration region which are regulated by a deformation of the integration contour. Since the deformation has to be small enough, the contour may still come close to a root of $\mathcal{F}$ and a large power of $\mathcal{F}$ can lead to large cancellations in the vicinity of the root. Sector decomposed integrands coming from dimensionless integrals, instead, can only have integrable singularities due to terms proportional to powers of $log\,(\mathcal{F})$ for values of the Feynman parameters where the second Symanzik polynomial $\mathcal{F}$ is zero.

3.2.5 Numerical Evaluation of the Amplitude

Since the multi-loop GoSam is still in development, we usually run GoSam only for the generation and analytical simplification of the amplitude in terms of the master integrals. GoSam can also produce `C++` code that numerically evaluates the coefficients and the integrals via an interface to the program pySecDec, which is described in detail in Section 4. That interface, however, only evaluates each master integral with a user-defined accuracy without taking the importance or difficulty of each individual integration into account.

A preliminary version of an optimized algorithm is implemented in an unpublished version of pySecDec and described in Section 4.7. The long-term goal is to modify GoSam and pySecDec such that code using the optimized algorithm is generated automatically. At the moment, we insert the coefficients produced by GoSam into the optimized sampling algorithm of pySecDec by hand for each process.

4 The Program pySecDec

In this Chapter, we describe the computer program pySecDec [161, 162], a toolbox for parametric and loop integrals in the context of dimensional regularization. Other public implementations also using the sector decomposition approach include `sector_decomposition` [163] supplemented with `CSectors` [142] and `FIESTA` [164–167].

pySecDec is a complete rewrite of its predecessor SecDec [168–170] using the programming languages `python` and `C++`. The algebraic part is processed with a mixture of a dedicated simple algebra module supplemented with `sympy` [171] and `FORM` [70–74]. The numerical integration can in principle be performed with any numerical integrator that can be called from `C++`. We provide easy-to-use interfaces to the `CQuad` integrator [172] as implemented in the GNU scientific library (GSL) [173], the integrators in the `CUBA` [174, 175] library, and our implementation [162] (see also Section 4.6) of a Quasi Monte Carlo integrator capable of running on GPUs [176].

In contrast to SecDec, pySecDec fully relies on open-source software which removes restrictions on the level of parallelization due to the number of available licenses.

The main motivation behind rewriting SecDec was the ability to use it for numerically evaluating the master integrals in an amplitude calculation where the master integrals were not known analytically.

The key task of pySecDec is to compute integrals of the form

$$\mathcal{P}\left(\vec{\varepsilon}\right) \int_0^1 \mathrm{d}x_1 ... \int_0^1 \mathrm{d}x_N \prod_{j=1}^{m} f_j\left(\vec{x},\vec{a}\right)^{b_j + \sum_k c_{jk}\varepsilon_k}, \tag{4.1}$$

where $\vec{\varepsilon} = \varepsilon_1, ..., \varepsilon_K$ are analytic regulators, $\mathcal{P}$ is a prefactor that can be expanded in a Laurent series around $\vec{\varepsilon} = \vec{0}$ with a finite number of singular terms, the f_i are polynomials in the integration variables $\vec{x} = x_1, ..., x_m$ and additional variables $\vec{a}$, and the b_j and c_{jk} are numeric constants. Feynman parametrized loop integrals take this form as discussed in Section 4.1. The workflow for computing a single integral is depicted in Figure 4.1.

This Chapter is structured as follows. The Feynman parametrization of a loop integral is discussed in Section 4.1. The resolution of singularities with the sector decomposition approach is discussed in Section 4.2 for singularities at zero and in Section 4.3 for singularities at unity. The deformation of the integration contour to avoid singularities in the interior of the integration domain is discussed in Section 4.4. An algorithm to identify equivalent integrals is presented in Section 4.5. The Quasi Monte Carlo integrator is described in Section 4.6. An algorithm that optimizes the evaluation of multiple integrals is described in Section 4.7.

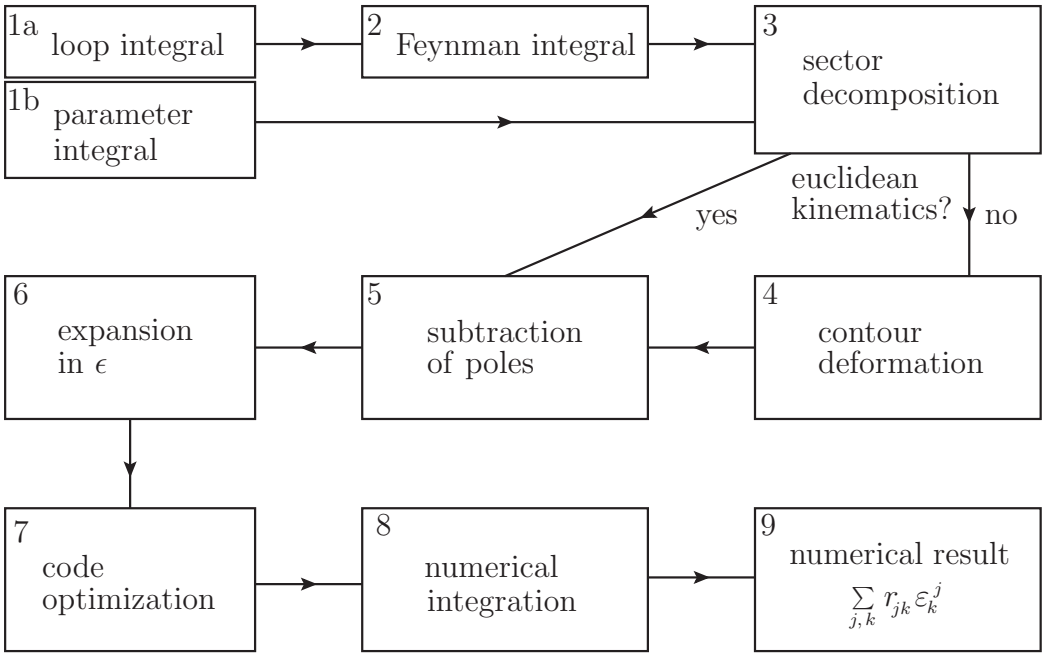

Figure 4.1: Workflow of the program pySecDec when used to compute a single integral. Steps 1 to 6 are performed in `python`, step 7 is done using `FORM`, while step 8 calls code from an automatically generated integral-specific `C++` library.

4.1 Feynman Parametrization

A general L-loop integral in D dimensions of tensor rank R with N propagators P_j raised to powers ν_j can be written as

$$G^{\mu_1\cdots\mu_R}_{l_1\cdots l_R} = \prod_{l=1}^{L} \int \mathrm{d}^D\kappa_l \frac{k_{l_1}^{\mu_1}\cdots k_{l_R}^{\mu_R}}{\prod_{j=1}^{N} P_j^{\nu_j}}, \quad \mathrm{d}^D\kappa_l = \frac{\mathrm{d}^D k_l}{i\pi^{\frac{D}{2}}}, \quad D = d_0 - d_\varepsilon\varepsilon, \tag{4.2}$$

where d_0 and d_ε are numeric constants, ε denotes the dimensional regulator, and the powers ν_j are polynomials in the regulator. The propagators can be quadratic,

$$P_j = p_j^2 - m_j^2 + i\delta, \tag{4.3}$$

or linear,

$$P_j = p_j\cdot q_j - m_j^2 + i\delta, \tag{4.4}$$

in the loop momenta where the p_j are linear combinations of external and loop momenta, the q_j are linear combinations of only external momenta, the m_j are the masses of the propagators, and the $i\delta$ denotes the Feynman prescription. If all unregulated

powers $\nu_j|_{\varepsilon=0}$ are positive, then such an integral can be brought into the form (4.1) as follows:

(i) Convert the product in the denominator to a sum by introducing Feynman parameters according to the formula (proof given in e.g. [18]),

$$\frac{1}{\prod_{j=1}^{N} P_j^{\nu_j}} = \frac{\Gamma(N_\nu)}{\prod_{j=1}^{N}\Gamma(\nu_j)} \int_0^1 \prod_{j=1}^{N} \mathrm{d}x_j\, \delta(1-\sum_{j=1}^{N} x_j) \frac{\prod_{j=1}^{N} x_j^{\nu_j-1}}{\left(\sum_{j=1}^{N} x_j P_j\right)^{N_\nu}}, \tag{4.5}$$

$$N_\nu \equiv \sum_{j=1}^{N} \nu_j,$$

which leads to

$$\begin{aligned} G^{\mu_1\dots\mu_R}_{l_1\dots l_R} =& \frac{\Gamma(N_\nu)}{\prod_{j=1}^{N}\Gamma(\nu_j)} \int_0^1 \left[\prod_{j=1}^{N} \mathrm{d}x_j\, x_j^{\nu_j-1}\right] \delta\big(1-\sum_{j=1}^{N} x_j\big) \\ & \int \prod_{l=1}^{L} \mathrm{d}^D\kappa_l\; k_{l_1}^{\mu_1}\dots k_{l_R}^{\mu_R} \left[\sum_{j,l=1}^{L} k_j\, M_{jl}\, k_l - 2\sum_{j=1}^{L} k_j\cdot Q_j + J + i\delta\right]^{-N_\nu}, \end{aligned} \tag{4.6}$$

where the matrix M, the vector Q, and the scalar J are determined by comparing the coefficients of the loop momenta with the sum in the denominator of (4.6).

(ii) Express the loop momenta in the numerator as partial derivatives by the Q_j.

(iii) Shift the loop momenta according to

$$k_l \to k_l - v_l, \quad v_l = \sum_{j=1}^{L} M^{-1}_{lj} Q_j, \tag{4.7}$$

which removes the linear term from the denominator.

(iv) Perform the integral over the loop momenta $\mathrm{d}^D\kappa_l$ analytically, e.g. by Wick rotating the loop momenta to Euclidean space, diagonalizing the symmetric matrix M with a unitary transformation, and solving the resulting integral on a loop-by-loop basis where the integration of a single loop momentum is described in e.g. [18].

After performing the loop integrations the integral takes the form [136, 142]

$$\begin{aligned} G^{\mu_1\cdots\mu_R}_{l_1\cdots l_R} =& (-1)^{N_\nu} \frac{1}{\prod_{j=1}^{N}\Gamma(\nu_j)} \\ & \int_0^1 \left[\prod_{k=1}^{N} \mathrm{d}x_k\, x_k^{\nu_k-1}\right] \delta(1-\sum_{j=1}^{N} x_j)\; \mathcal{N}^{\mu_1\cdots\mu_R}_{l_1\cdots l_R} \frac{\mathcal{U}^{N_\nu-(L+1)D/2-R}}{\mathcal{F}^{N_\nu-LD/2}}, \end{aligned} \tag{4.8}$$

where

$$\mathcal{U} = \det(M) \quad \text{and} \quad \mathcal{F} = \mathcal{U} \left[\sum_{j,l=1}^{L} Q_j \, M_{jl}^{-1} \, Q_l - J - i\delta \right] \tag{4.9}$$

are the Symanzik polynomials, and

$$\mathcal{N}_{l_1 \cdots l_R}^{\mu_1 \cdots \mu_R} = \sum_{m=0}^{\lfloor R/2 \rfloor} \left(-\frac{1}{2} \right)^m \mathcal{F}^m \, \Gamma\left(N_\nu - LD/2 - m\right) \sum_{\substack{i_1,\ldots,i_R = 1,\ldots,R \\ +\text{permutations}}} \tilde{g}_{l_{i_1} \cdots l_{i_{2m}}}^{\mu_{i_1} \cdots \mu_{i_{2m}}} \, \tilde{Q}_{l_{i_{2m}} \cdots l_{i_R}}^{\mu_{i_{2m}} \cdots \mu_{i_R}}, \tag{4.10}$$

is a polynomial resulting from the numerator structure with

$$\tilde{g}_{l_1 \cdots l_{2m}}^{\mu_1 \cdots \mu_{2m}} \equiv \prod_{j=1}^{m} \tilde{g}_{l_{2j-1} \, l_{2j}}^{\mu_{2j-1} \, \mu_{2j}}, \quad \tilde{g}_{l_j \, l_k}^{\mu_j \, \mu_k} \equiv \tilde{M}_{l_j l_k} \, g^{\mu_j \mu_k}, \tag{4.11}$$

$$\tilde{Q}_{l_{2m} \cdots l_R}^{\mu_{2m} \cdots \mu_R} \equiv \prod_{j=2m}^{R} \tilde{Q}_{l_j}^{\mu_j}, \quad \tilde{Q}_{l_j}^{\mu_j} \equiv \sum_{l=1}^{L} \tilde{M}_{l_j l} \, Q_l^{\mu_j}, \tag{4.12}$$

where

$$\tilde{M} \equiv \det(M) \, M^{-1}$$

denotes the adjugate matrix of M and $g^{\mu\nu}$ denotes the metric tensor, and where $\lfloor x \rfloor \equiv \max\{k \in \mathbb{Z} | k \leq x\}$ denotes the floor operation.

If we try to use formula (4.5) for an inverse propagator, e.g. $\nu_n = -1$, then we find that the integral diverges at the zero border. However, we can use partial derivatives (see also [177] and references therein) to raise propagators to the numerator,

$$\frac{P_n}{\left(\sum_{j=1}^{N} x_j P_j\right)^{K+1}} = -\frac{1}{K} \frac{\partial}{\partial x_n} \frac{1}{\left(\sum_{j=1}^{N} x_j P_j\right)^{K}}. \tag{4.13}$$

We can split the negative integer part $\hat{\nu}_j$ off the power of each propagator,

$$\tilde{\nu}_j \equiv \nu_j + \hat{\nu}_j, \quad \hat{\nu}_j \equiv \max\left(0, -\left\lfloor \nu_j|_{\varepsilon=0} \right\rfloor\right), \tag{4.14}$$

such that the product of propagators is split up as

$$\frac{1}{\prod_{j=1}^{N} P_j^{\nu_j}} = \frac{\prod_{j=1}^{N} P_k^{\hat{\nu}_j}}{\prod_{j=1}^{N} P_j^{\tilde{\nu}_j}}. \tag{4.15}$$

The denominator of (4.15) can be Feynman parametrized according to (4.5), while the numerator can be expressed in terms of derivatives by repeated application of (4.13).

The generalization of (4.5) to drop the restriction $\nu_j|_{\varepsilon=0} \geq 0$ reads

$$\begin{aligned}\frac{1}{\prod_{j=1}^{N} P_j^{\nu_j}} =& \frac{\Gamma(N_\nu)}{\prod_{j=1}^{N}\Gamma(\tilde{\nu}_j)} \int_0^1 \left[\prod_{k=1}^{N} \mathrm{d}x_k\, x_k^{\tilde{\nu}_k-1}\right] \delta(1-\sum_{j=1}^{N} x_j) \\ & \left[\prod_{n=1}^{N} \left(-\frac{\partial}{\partial x_n}\right)^{\hat{\nu}_n}\right] \left(\sum_{j=1}^{N} x_j P_j\right)^{-N_\nu} \Bigg|_{x_j=0 \text{ if } \tilde{\nu}_j=0} .\end{aligned} \tag{4.16}$$

This modification leaves the second line of (4.6) unchanged such that steps (ii) to (iv) of the procedure described above can be applied in exactly the same way. The generalization of (4.8) reads

$$\begin{aligned}G_{l_1\cdots l_R}^{\mu_1\cdots\mu_R} =& (-1)^{N_\nu} \frac{1}{\prod_{j=1}^{N}\Gamma(\tilde{\nu}_j)} \int_0^1 \left[\prod_{k=1}^{N} \mathrm{d}x_k\, x_k^{\tilde{\nu}_k-1}\right] \delta(1-\sum_{j=1}^{N} x_j) \\ & \left[\prod_{n=1}^{N} \left(-\frac{\partial}{\partial x_n}\right)^{\hat{\nu}_n} \mathcal{N}_{l_1\cdots l_R}^{\mu_1\cdots\mu_R} \frac{\mathcal{U}^{N_\nu-(L+1)D/2-R}}{\mathcal{F}^{N_\nu-LD/2}}\right]_{x_j=0 \text{ if } \tilde{\nu}_j=0} .\end{aligned} \tag{4.17}$$

The derivatives in the second line of (4.17) are computed using

$$\frac{\partial}{\partial x_k}\left(\frac{\mathcal{U}^n\,\mathcal{N}}{\mathcal{F}^m}\right) = \frac{\mathcal{U}^{n-1}}{\mathcal{F}^{m+1}}\mathcal{N}', \tag{4.18}$$

where we have omitted the indices of the numerator for brevity and where the new numerator $\mathcal{N}'$ is given by

$$\mathcal{N}' = n\,\mathcal{F}\left(\frac{\partial\mathcal{U}}{\partial x_k}\right)\mathcal{N} - m\left(\frac{\partial\,\mathcal{F}}{\partial x_k}\right)\mathcal{U}\,\mathcal{N} + \mathcal{F}\,\mathcal{U}\left(\frac{\partial\mathcal{N}}{\partial x_k} + \frac{\partial\mathcal{N}}{\partial F}\frac{\partial\,\mathcal{F}}{\partial x_k} + \frac{\partial\mathcal{N}}{\partial U}\frac{\partial\mathcal{U}}{\partial x_k}\right). \tag{4.19}$$

Computing the derivative using (4.18) ensures that the parameter integral remains in a factorized form.

Note that (4.19) allows to calculate only the derivatives explicitly while $\mathcal{U}$ and $\mathcal{F}$ can be left symbolic, which can significantly simplify the numerator. In fact, the numerator does not encode any singularities such that $\mathcal{U}$ and $\mathcal{F}$ can be kept symbolic throughout the entire calculation until numerical values of the integrand are required.

Given the corresponding graph of a loop integral, the procedure above suggests to assign a momentum routing in order to obtain an integral of the form (4.2). Alternatively, it is also possible to compute the Symanzik polynomials $\mathcal{U}$ and $\mathcal{F}$ directly from the graphical representation, see e.g. [178]. While a numerator in terms of explicit loop momenta only makes sense with a well defined momentum routing, a numerator arising from inverse propagators can be constructed using partial derivatives as described above independent of the method used to obtain $\mathcal{U}$ and $\mathcal{F}$. Both methods for constructing the Symanzik polynomials are implemented in pySecDec within classes

`LoopIntegralFromPropagators` and `LoopIntegralFromGraph`. Examples how to perform the Feynman parametrization with pySecDec are provided in Appendix B.2.

Finally, we have to integrate out the δ-distribution in (4.17) in order to arrive at a parameter integral of the form (4.1). Introducing poles at the upper integration limits can be avoided by exploiting the homogeneity of $\mathcal{U}$ and $\mathcal{F}$ [136]. Alternatively, the Cheng-Wu theorem [179] (see also [177]) can be applied, which results in an integral with integration boundaries zero to infinity. In that case, the integral is mapped back to the unit hypercube in the sector decomposition step which is described in Section 4.2.1.

4.2 Overlapping Singularities at Zero

Integrals of the form (4.1) have poles in the regulators ε_k if some of the b_j are sufficiently small. Consider for example the parameter integral,

$$\mathcal{I} = \int_0^1 \mathrm{d}x \int_0^1 \mathrm{d}y \; (x+y)^{-2+\varepsilon} \, f(x,y), \tag{4.20}$$

where f is a product of exponentiated polynomials and a function that is regular when either x or y or both are set to zero. The integrand has an overlapping singularity at the origin $x = y = 0$, which is integrable for $\varepsilon > 0$. Our goal is to expand the integrand in a Laurent series around the singularity in $\varepsilon = 0$ at the integrand level. This is done in two steps that are further described in the following subsections, (i) Sector Decomposition and (ii) Subtraction of Poles.

4.2.1 Sector Decomposition

The Sector Decomposition step transforms an integral with an overlapping singularity into a sum of integrals with separated singularities. To illustrate this, we separate the integral in (4.20) into two regions, $x > y$ and $x < y$,

$$\begin{aligned}\mathcal{I} &= \int_0^1 \mathrm{d}x \int_0^1 \mathrm{d}y \; (x+y)^{-2+\varepsilon} \, f(x,y) [\underbrace{\Theta(x-y)}_{x>y} + \underbrace{\Theta(y-x)}_{x<y}] \\ &\equiv \underbrace{\int_0^1 \mathrm{d}x \int_0^x \mathrm{d}y \; (x+y)^{-2+\varepsilon} \, f(x,y)}_{\mathcal{I}_{x>y}} + \underbrace{\int_0^1 \mathrm{d}y \int_0^y \mathrm{d}x \; (x+y)^{-2+\varepsilon} \, f(x,y)}_{\mathcal{I}_{x<y}} .\end{aligned} \tag{4.21}$$

Next, we substitute the integration variables as,

$$\begin{aligned} y &\to xy \quad \text{in} \quad \mathcal{I}_{x>y}, \\ x &\to xy \quad \text{in} \quad \mathcal{I}_{x<y}, \end{aligned} \tag{4.22}$$

which leads to

$$\begin{aligned}\mathcal{I}_{x>y} &= \int_0^1 \mathrm{d}x \int_0^1 \mathrm{d}y\, x^{-1+\varepsilon}\,(1+y)^{-2+\varepsilon}\, f(x,xy)\\ \mathcal{I}_{x<y} &= \int_0^1 \mathrm{d}x \int_0^1 \mathrm{d}y\, y^{-1+\varepsilon}\,(x+1)^{-2+\varepsilon}\, f(yx,y).\end{aligned} \tag{4.23}$$

The originally overlapping singularity is now separated into two integrals with a singularity in only one variable each. The remappings described above are graphically represented in Figure 4.2.

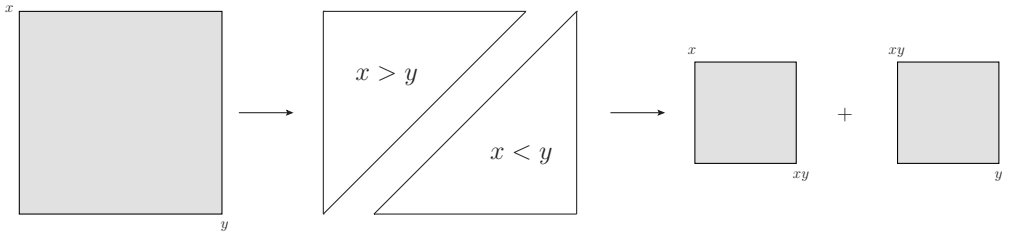

Figure 4.2: Graphical representation of the remappings described by Equations (4.21) and (4.23).

In general, the Sector Decomposition algorithm generates integrals with factorizing monomials containing all singularities at the zero integration boundary times a finite remainder. In particular, the finite remainder is free of singularities in a vicinity of all integration variables close to zero. An iterative algorithm to achieve this factorization based on decomposing the integration region and remapping the resulting integrals back to the unit hypercube is described in [135, 136]. That algorithm, however, can run into an infinite recursion since iterated application can lead to an incompletely decomposed integral that has already been encountered in an earlier iteration. Alternatively, an algorithm based on algebraic geometry that is guaranteed to terminate has been suggested in [180, 181] and refined in [170, 182, 183]. The original iterative as well as both geometric decomposition algorithms are implemented in pySecDec. The refined geometric algorithm however requires infinity as upper integration boundaries such that it can currently only be selected for loop integrals in combination with eliminating the δ-distribution using the Cheng-Wu theorem [179] (see also [177]).

4.2.2 Subtraction of Poles

Given the factorization of the poles, the integrals in (4.23) schematically take the form

$$\mathcal{G}_1 = \int_0^1 \mathrm{d}t\, t^{-1+\varepsilon} g(t), \tag{4.24}$$

where t is either x or y and the dependence on the other integration variable is suppressed for brevity. The pole of such an integral can be extracted by adding and subtracting $g(0)$,

$$\begin{aligned}\mathcal{G}_1 &= \int_0^1 \mathrm{d}t\, t^{-1+\varepsilon} \left(g(0) + g(t) - g(0)\right) && (4.25)\\ &= \underbrace{\int_0^1 \mathrm{d}t\, t^{-1+\varepsilon} g(0)}_{=\frac{1}{\varepsilon}g(0)} + \underbrace{\int_0^1 \mathrm{d}t\, t^{-1+\varepsilon} \left(g(t) - g(0)\right),}_{\text{finite for } \varepsilon\to 0\text{, expand integrand in } \varepsilon} && (4.26)\end{aligned}$$

which is possible because g has no singularity at $t = 0$ by construction. The pole in the regulator ε can be extracted from the first term of (4.26) by performing the integration analytically. The integrand in the second term of (4.26) approaches the (by construction finite) derivative of g at zero for $t \to 0$ and $\varepsilon \to 0$. We can therefore Taylor expand the integrand in the regulator which leaves integrals that can be performed numerically after applying this procedure to all integration variables and given numerical values for all other variables. In case of higher poles, the procedure can be extended to adding and subtracting the first few terms of the Taylor expansion of $g(t)$ around zero [136]; i.e.

$$\begin{aligned}\mathcal{G}_n &= \int_0^1 \mathrm{d}t\, t^{-n+\varepsilon} g(t)\\ &= \int_0^1 \mathrm{d}t\, t^{-n+\varepsilon} \left(\sum_{k=0}^{n-1} g^{(k)}(0)\frac{t^k}{k!} + g(t) - \sum_{k=0}^{n-1} g^{(k)}(0)\frac{t^k}{k!}\right) && (4.27)\\ &= \int_0^1 \mathrm{d}t\, t^{-n+\varepsilon} \left(\sum_{k=0}^{n-1} g^{(k)}(0)\frac{t^k}{k!}\right) + \int_0^1 \mathrm{d}t\, t^{-n+\varepsilon} \left(g(t) - \sum_{k=0}^{n-1} g^{(k)}(0)\frac{t^k}{k!}\right),\end{aligned}$$

where $g^{(n)}$ denotes the n^{th} derivative of g. Again, the poles can be extracted from the first term by explicit integration while the integrand of the second term can be Taylor expanded in ε since it approaches the finite value of $g^{(n)}(0)$ in the limit $t \to 0$, $\varepsilon \to 0$.

4.3 Singularities at Unity

So far, we have only dealt with singularities of general parameter integrals as defined in (4.1) coming from the zero boundary in Section 4.2. Singularities in the interior of the integration domain are discussed in Section 4.4. In this section, we describe the treatment of singularities from the entire border of the integration domain. A similar discussion to the one below has been published in [184].

Loop integrals usually have no singularities originating from $x_j = 1$: The $\mathcal{U}$ polynomial is always positive semidefinite in the integration domain while the kinematic dependent $\mathcal{F}$ polynomial often has a so-called Euclidean region (all Mandelstam variables negative and all masses positive), where it is positive semidefinite as well. However, integrals without Euclidean region or a special choice of kinematics can lead to a vanishing $\mathcal{F}$ polynomial after sector decomposition when an $x_j = 1$.

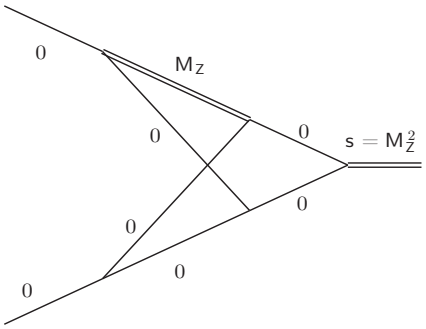

Figure 4.3: A vertex diagram where splitting the integration domain as denoted in equation 4.29 maps a singularity in the interior of the integration domain to an end point of the integration. Figure taken from [185].

We have been notified [185] of an integral that could not be computed with earlier versions of SecDec because of the treatment of this kind of singularities. Before inspecting the loop integral, first consider a simple toy integral that reproduces the problem,

$$\lim_{\delta\to 0} \int_0^1 \mathrm{d}x \int_0^1 \mathrm{d}y \ (x - y - i\delta)^{-2+\varepsilon}\,, \tag{4.28}$$

where the $-i\delta$ prescription is to be understood analogous to the Feynman prescription in loop integrals. The integrand has a regulated singularity along the line $x = y$. The $-i\delta$ shifts the singularity away from the real axis which regulates the integral in the interior of the integration domain. On the border, however, the limit $\delta \to 0$ forces the endpoints of the integral back to the real axis and thus into the singularity. Therefore, the singular endpoints $x = y = 0$ and $x = y = 1$ are purely regulated by the ε which becomes manifest as $1/\varepsilon$ poles.

Versions one to three of SecDec split the integration domain as

$$\int_0^1 \mathrm{d}x_j = \int_0^{\frac{1}{2}} \mathrm{d}x_j \; + \int_{\frac{1}{2}}^1 \mathrm{d}x_j \;, \tag{4.29}$$

and then map the integration boundaries back to the unit interval by the substitutions $x_j = z_j/2$ and $x_j = 1 - z_j/2$, respectively. More details about the previous split can be found in the SecDec-1 paper [168].

Although splitting all integration variables at 1/2 for all integration variables seems a natural choice, that is exactly what causes unregulated singularities to remain even after the whole sector decomposition procedure. The reason is that the singular point $x = y = 1/2$ in the interior of the integration domain is mapped to an endpoint (all x_j equal to either one or zero) of the resulting integrals. However, the contour deformation vanishes at the endpoints by construction. The singular point $x = y = 1/2$ that should be avoided by a deformed contour is therefore left unregulated. Note that the contour deformation has to vanish on the endpoints of the original integral only. Consequently, one could in principle track which new endpoints are introduced by the split and allow for a nonzero deformation at those. One would then, however, have to match the nonzero deformation at these artificial endpoints between all split sectors. In particular, the split sectors could then no longer be considered independent of each other.

Instead, we can simply avoid mapping singular points to the border by splitting x and y elsewhere. In pySecDec, we generate random integers $r_j \in [1, 19]$, split the integration domain as

$$\int_0^1 \mathrm{d}x_j = \int_0^{r_j/20} \mathrm{d}x_j \; + \int_{r_j/20}^1 \mathrm{d}x_j, \tag{4.30}$$

and remap the resulting integration borders back to the unit interval substituting $z_j = \frac{r_j}{20} x_j$ and $z_j = 1 - \frac{r_j}{20} x_j$, respectively. The singularity of the integrand at $x = y$ and possible resulting integral domains from the two different splitting procedures are depicted in Figure 4.4.

To summarize, unregulated singularities can remain in the sector decomposed integrals if the integration domain is split such that singular points of the integrand are mapped to endpoints of the integration. Consider for example the three-point function depicted in Figure 4.3. The first analytical calculation is available in [186] where it is called $N3$. Note that the squared mass of the single massive propagator is equal to the Mandelstam invariant s. The $\mathcal{F}$ polynomial can be expressed as,

$$\begin{aligned} \mathcal{F}/m_Z^2 = {} & x_3^2 x_5 + x_3^2 x_4 + x_2 x_3 x_5 + x_2 x_3 x_4 + x_1 x_3 x_5 + x_1 x_3 x_4 \\ & + x_1 x_3^2 + x_1 x_2 x_3 + x_0 x_3 x_4 + x_0 x_3^2 + x_0 x_2 x_3 \\ & - x_1 x_2 x_4 - x_0 x_1 x_5 - x_0 x_1 x_4 - x_0 x_1 x_2 - x_0 x_1 x_3. \end{aligned} \tag{4.31}$$

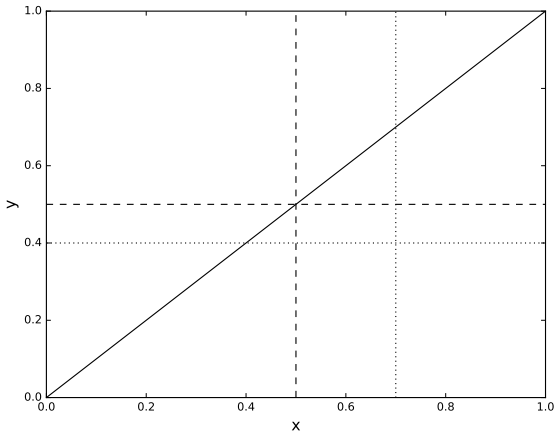

Figure 4.4: Graphical representation of the "$x-y$" problem. The solid line shows the singularity of then integrand at $x = y$. The dashed line shows a split at $x = y = 1/2$ which maps a singular point in the interior of the integration region to end points of the resulting regions. The dotted line shows how the integrand can be split without mapping a point of the singularity to the border of the resulting integrals.

where m_Z is the mass of the Z boson and the x_j are Feynman parameters.

It can easily be verified that $\mathcal{F}$ vanishes for e.g. $x_0 = x_1 = x_2 = x_4 = x_5 = 1$ and $x_3 = 1/2$. A split of x_3 at $1/2$ maps that singularity to the endpoints of the split integrals as described above, which explains why this integral could not be evaluated with earlier versions of SecDec.

4.4 Singularities in the Interior of the Integration Domain (Contour Deformation)

Singularities of the integrand in the interior of the integration domain are avoided by the Feynman prescription $i\delta$ for loop integrals. This prescription can be realized by deforming the integration contour into the complex plane [169, 182, 187–190]. We summarize the method which is implemented in pySecDec and which has been used in SecDec since version 2 of the program.

Consider a polynomial with a Feynman or Feynman-like prescription $i\delta$ as introduced in Section 4.1. That prescription translates into the $\mathcal{F}$ polynomial after Feynman parametrization, see Equation (4.9). We can satisfy the prescription by changing the integral along the real axis, parametrized by the real variables $\vec{x} = x_1, ..., x_m$, to a contour integral in the complex plane, parametrized by the complex variables $\vec{z} = z_1, ..., z_m$. The imaginary part of the deformed second Symanzik polynomial $\mathrm{Im}\left[\mathcal{F}(\vec{z})\right]$ should obtain an additional imaginary part according to the sign of the prescription as

compared to its undeformed version $\mathrm{Im}\left[\mathcal{F}(\vec{x})\right]$. This means

$$\mathrm{Im}\left[\mathcal{F}(\vec{z})\right] \leq \mathrm{Im}\left[\mathcal{F}(\vec{x})\right] \tag{4.32}$$

for the $-i\delta$ prescription in Equation (4.9).

The transformation

$$\vec{z} : [0,1]^m \longrightarrow \mathbb{C}^m, \quad x_k \to z_k\left(\vec{x}\right) \equiv x_k - i\lambda_k\, x_k\left(1-x_k\right)\frac{\partial \mathrm{Re}\left[\mathcal{F}\left(\vec{x}\right)\right]}{\partial x_k} \tag{4.33}$$

fulfils the requirement (4.32) for appropriate fixed values of the real parameters $\vec{\lambda} = \lambda_1, ..., \lambda_m$: That can be seen by Taylor expanding the deformed $\mathcal{F}$ polynomial

$$\begin{aligned}
\mathcal{F}\left(\vec{z}\left(\vec{x}\right)\right) = &+ \mathrm{Re}\left[\mathcal{F}(\vec{x})\right] + i\,\mathrm{Im}\left[\mathcal{F}(\vec{x})\right] \\
&+ \sum_{k=1}^{m} \lambda_k \left[\boxed{-i\left(\frac{\partial\,\mathrm{Re}\left[\mathcal{F}(\vec{x})\right]}{\partial x_k}\right)^2} + \frac{\partial\,\mathrm{Re}\left[\mathcal{F}(\vec{x})\right]}{\partial x_k}\frac{\partial\,\mathrm{Im}\left[\mathcal{F}(\vec{x})\right]}{\partial x_k}\right] x_k(1-x_k) \\
&+ \sum_{k,l=1}^{m} \frac{\lambda_k\lambda_l}{2}\left[-\frac{\partial^2\,\mathrm{Re}\left[\mathcal{F}(\vec{x})\right]}{\partial x_k \partial x_l} \boxed{-i\frac{\partial^2\,\mathrm{Im}\left[\mathcal{F}(\vec{x})\right]}{\partial x_k \partial x_l}} \right] \prod_{j=k,l} \frac{\partial\,\mathrm{Re}\left[\mathcal{F}(\vec{x})\right]}{\partial x_j} x_j(1-x_j) \\
&+ \mathcal{O}(\lambda_j\lambda_k\lambda_l)
\end{aligned} \tag{4.34}$$

around $\lambda_k = 0$. First note that the highlighted term in the second line of (4.34) is (i) the only imaginary contribution at $\mathcal{O}(\lambda_k)$ and (ii) negative in the integration domain $x_k \in [0,1]$ for $\lambda_k > 0$. Second note that an imaginary contribution of indefinite sign only enters at the higher orders in the $\vec{\lambda}$ expansion. The values λ_k can therefore be chosen such that the term at $\mathcal{O}\left(\lambda_k\right)$ with the "correct" sign dominates the overall additional imaginary part. The condition (4.32) can always be fulfilled by decreasing any given values for $\lambda_k > 0$.

pySecDec checks the condition (4.32) at every numerical evaluation of the integrand. It also checks that the real part of selected other polynomials, for example the first Symanzik polynomial $\mathcal{U}$, remain positive after deformation,

$$\mathrm{Re}\left[\mathcal{U}(\vec{z})\right] \geq 0. \tag{4.35}$$

This check can be important when the unregulated power of $\mathcal{U}$ is negative; i.e. $\mathcal{U}$ is in the denominator. If poles coming from complex zeros of $\mathcal{U}$ are crossed by the contour deformation, then their residues are picked up and change the result. Condition (4.35) is sufficient to avoid picking up such residues.

4.5 Symmetry Finder

Compared to SecDec-3, the symmetry finder has been significantly improved. An algorithm that is guaranteed to find all sector symmetries has been adopted from [191].

An independent symmetry finder based on graph isomorphisms using the external program `dreadnaut` [192] is also implemented as a cross-check. Due to its better performance [193], we restrict the discussion in this Thesis to our extension of Pak's algorithm [191]. A detailed explanation of the algorithm based on `dreadnaut` can be found in [193]. We further illustrate, in Section 4.5.2, how our extension of Pak's algorithm can be used to identify matroid symmetries among anisomporphic graphs within the loop integral database `Loopedia` [130]. The following is largely based on [194].

A key concept to finding sector and matroid symmetries is to identify two polynomials with one another when permutations of subsets of variables are allowed. For example,

$$\int_0^1 \mathrm{d}x\,\mathrm{d}y\;(x+2y) = \int_0^1 \mathrm{d}x\,\mathrm{d}y\;(y+2x); \tag{4.36}$$

i.e. the integration variables can be relabelled. Algorithms to find symmetries when all variables are equivalent have been introduced in [191, 192]. Their implementation in pySecDec is discussed in [193]. To find matroid symmetries, arbitrary relabelling of additional parameters (e.g. masses) must be taken into account as well, for example,

$$\int_0^1 \mathrm{d}x\,\mathrm{d}y\;(sx+m_1y+2m_2) \quad \overset{m_1\leftrightarrow m_2}{=\!=\!=} \quad \int_0^1 \mathrm{d}x\,\mathrm{d}y\;(sy+m_2x+2m_1), \tag{4.37}$$

if m_1 and m_2 can be interchanged. In the following, we describe a generalization of the algorithm in [191] that allows for multiple sets of interchangeable ("equivalent") variables.

As a first step, polynomials are expressed as a matrix of exponents and coefficients. Each row corresponds to one term of the polynomial. The first column consists of the coefficients of the terms while the remaining columns store the powers of the occurring variables. An example is shown in Figure 4.5.

$$\begin{aligned} &1\cdot m_1^0\cdot m_2^0\cdot s^1\cdot x^1\cdot y^0\\ &+1\cdot m_1^1\cdot m_2^0\cdot s^0\cdot x^0\cdot y^1\\ &+2\cdot m_1^0\cdot m_2^1\cdot s^0\cdot x^0\cdot y^0 \end{aligned} \quad \equiv \quad \begin{array}{c} \begin{array}{cccccc} \text{coefficient} & m_1 & m_2 & s & x & y \end{array}\\ \left[\begin{array}{cccccc} 1 & 0 & 0 & 1 & 1 & 0\\ 1 & 1 & 0 & 0 & 0 & 1\\ 2 & 0 & 1 & 0 & 0 & 0 \end{array}\right] \end{array}$$

Figure 4.5: Representation of the polynomial $sx + m_1y + 2m_2$ as an integer matrix.

If the coefficient is not an integer, it is sufficient to replace each individual coefficient with a unique index during the canonicalization. Multiple polynomials can be canonicalized simultaneously by multiplication of a label to the coefficient of each polynomial or by adding a column with an index identifying the polynomial. Writing the polynomial as an integer matrix facilitates to tackle the problem without a computer algebra

system. Finding equality of two polynomials under relabelling corresponds to finding equality of their matrices while allowing for permutations of the rows and columns. Rather than generating and trying all permutations, it is much more efficient to bring the polynomials to compare into a canonical form.

To canonicalize a polynomial, we suggest a generalization of the algorithm in [191]. The key idea is to build a canonical representation column by column. In the following detailed description, we assume that the first column of the matrix corresponds to the coefficients, the next n_1 columns to the powers of the first set of equivalent parameters, the next n_2 columns to the powers of the second set of equivalent parameters and so on.

(i) Write the polynomial as an integer matrix, see above.
(ii) Make n_1 copies of the matrix. In the i^{th} copy, swap the column of the i^{th} parameter parameter with the column of the first parameter.
(iii) In all copies, sort rows lexicographically by the columns corresponding to the coefficient and the first parameter.
(iv) Discard all but those copies with the lexicographically smallest columns corresponding to the first parameter.
(v) For all remaining copies of the matrix, make $n_1 - 1$ new copies and swap the column corresponding to the i^{th} parameter with the column corresponding to the second parameter in each i^{th} new copy.
(vi) In all copies, sort rows lexicographically by the columns corresponding to the coefficient and the first two parameters.
(vii) Discard all but those copies with the lexicographically smallest columns corresponding to the second parameter. Note that some of the remaining matrices are likely to appear multiple times. It is strongly advisable to check for and delete repetitions in this step as well.
(viii) Repeat the procedure with the remaining parameters that are equivalent to the first parameter.
(ix) Repeat all previous steps for all remaining matrices for every group of equivalent variables. When considering the j^{th} group of equivalent parameters, always include the coefficient and all $n_{i<j}$ variables in the sorting steps; i.e. a after a column has been included in the sorting, it should be included in all later sortings.
(x) Pick the lexicographically smallest matrix as the canonical representation.

Our generalization to the algorithm in [191] is the second to last step, where we repeat the original algorithm for all sets of equivalent parameters.

4.5.1 Sector Symmetries

As mentioned before, finding sector symmetries is already covered by the original algorithms described in [191, 192] since there is only one set of equivalent parameters - the integration variables. The number of sectors and therefore the complexity of the numerical integration can be significantly reduced for sufficiently symmetric integrals [193].

When code for an integral is created using `make_package` or `loop_package`, pySecDec runs Pak's algorithm by default in order reduce the number of numerical integrations. The symmetry finder is usually run twice: First on the primary sectors and second on all sector decomposed sectors from all primary sectors together. It can only be used to reduce the number of primary sectors when there are no singularities at one as discussed in section 4.3 because then the remappings required when splitting a sector can alter the number of terms such that the problem of establishing symmetries is no longer covered by the algorithms we consider. Solutions to overcome this issue are left for future work.

4.5.2 Matroid Symmetries

`Loopedia` [130] is a database of Feynman integrals that allows to search the database for literature on a given graph rather than conventional search keys like author, title, etc. However, `Loopedia` currently only shows results corresponding to graphs that are isomorphic to the input graph. Articles considering the corresponding integral are missed if they are listed in the database under a different graph that is related by a matroid. We now comment on how to obtain a canonical form of the integrals present in the `Loopedia` database. Given a canonical representation for every graph, `Loopedia` could point the user to other graphs that are related by a matroid symmetry e.g. in the single graph view or in the graph browser.

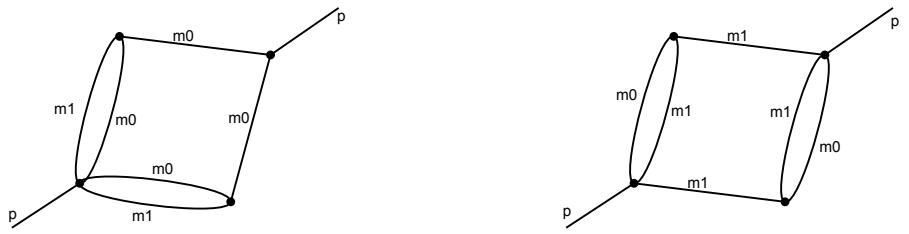

(a) **(b)**

Figure 4.6: Example of anisomorphic graphs corresponding to the same integral.

Matroid symmetries are manifest in Feynman parameterization by comparing the Symanzik polynomials $\mathcal{U}$ and $\mathcal{F}$ under relabellings of the external momenta, the masses, and the Feynman parameters. Our goal is to identify anisomorphic graphs that have an equivalent Feynman parameter representation. Consider for example the two graphs shown in Figure 4.6. Computing their corresponding Symanzik polynomials with

pySecDec, we get

$$
\begin{aligned}
\mathcal{U}_a =& + x_0x_1x_3 + x_0x_1x_4 + x_0x_2x_3 + x_0x_2x_4 + x_0x_3x_4 + x_0x_3x_5 + x_0x_4x_5 + x_1x_3x_5 \\
&+ x_1x_4x_5 + x_2x_3x_5 + x_2x_4x_5 + x_3x_4x_5 \\
\mathcal{F}_a =& + m_1^2x_0x_1x_3x_4 + m_1^2x_0x_1x_3x_5 + m_1^2x_0x_1x_4^2 + m_1^2x_0x_1x_4x_5 + m_1^2x_0x_2x_3x_4 + m_1^2x_0x_2x_3x_5 \\
&+ m_1^2x_0x_2x_4^2 + m_1^2x_0x_2x_4x_5 + m_1^2x_0x_3x_4^2 + 2m_1^2x_0x_3x_4x_5 + m_1^2x_0x_3x_5^2 + m_1^2x_0x_4^2x_5 \\
&+ m_1^2x_0x_4x_5^2 + m_1^2x_1x_3x_4x_5 + m_1^2x_1x_3x_5^2 + m_1^2x_1x_4^2x_5 + m_1^2x_1x_4x_5^2 + m_1^2x_2x_3x_4x_5 \\
&+ m_1^2x_2x_3x_5^2 + m_1^2x_2x_4^2x_5 + m_1^2x_2x_4x_5^2 + m_1^2x_3x_4^2x_5 + m_1^2x_3x_4x_5^2 + m_0^2x_0^2x_1x_3 \\
&+ m_0^2x_0^2x_1x_4 + m_0^2x_0^2x_2x_3 + m_0^2x_0^2x_2x_4 + m_0^2x_0^2x_3x_4 + m_0^2x_0^2x_3x_5 + m_0^2x_0^2x_4x_5 \\
&+ m_0^2x_0x_1^2x_3 + m_0^2x_0x_1^2x_4 + 2m_0^2x_0x_1x_2x_3 + 2m_0^2x_0x_1x_2x_4 + m_0^2x_0x_1x_3^2 + 2m_0^2x_0x_1x_3x_4 \\
&+ 2m_0^2x_0x_1x_3x_5 + 2m_0^2x_0x_1x_4x_5 + m_0^2x_0x_2^2x_3 + m_0^2x_0x_2^2x_4 + m_0^2x_0x_2x_3^2 + 2m_0^2x_0x_2x_3x_4 \\
&+ 2m_0^2x_0x_2x_3x_5 + 2m_0^2x_0x_2x_4x_5 + m_0^2x_0x_3^2x_4 + m_0^2x_0x_3^2x_5 + 2m_0^2x_0x_3x_4x_5 + m_0^2x_1^2x_3x_5 \\
&+ m_0^2x_1^2x_4x_5 + 2m_0^2x_1x_2x_3x_5 + 2m_0^2x_1x_2x_4x_5 + m_0^2x_1x_3^2x_5 + 2m_0^2x_1x_3x_4x_5 + m_0^2x_2^2x_3x_5 \\
&+ m_0^2x_2^2x_4x_5 + m_0^2x_2x_3^2x_5 + 2m_0^2x_2x_3x_4x_5 + m_0^2x_3^2x_4x_5 - p^2x_0x_1x_2x_3 - p^2x_0x_1x_2x_4 \\
&- p^2x_0x_1x_3x_4 - p^2x_0x_2x_3x_5 - p^2x_0x_2x_4x_5 - p^2x_0x_3x_4x_5 - p^2x_1x_2x_3x_5 - p^2x_1x_2x_4x_5 \\
&- p^2x_1x_3x_4x_5 \\
\mathcal{U}_b =& \mathcal{U}_a\left(x_0 \leftrightarrow x_1\right) \\
\mathcal{F}_b =& \mathcal{F}_a\left(x_0 \leftrightarrow x_1, m_0 \leftrightarrow m_1\right);
\end{aligned}
\tag{4.38}
$$

i.e. their Symanzik polynomials $\mathcal{U}$ and $\mathcal{F}$ are equal up to the permutation $x_0 \leftrightarrow x_1$ and $m_0 \leftrightarrow m_1$. The labelling of the Feynman parameters x_0 to x_5 depends on the ordering of the internal and external lines in the input to pySecDec and is therefore arbitrary. The masses m_0 and m_1 are also arbitrary by definition and therefore interchangeable. As a consequence, their Feynman representations are equivalent since the two graphs have the same numbers of loops and propagators.

To identify permutations of the external momentum labels, we keep all scalar products as they are except for squared momenta. Squares of external momenta may be set equal to an internal mass and are therefore considered equivalent to the masses.

In addition to relabellings, any one of the external momenta can be eliminated by momentum conservation. Eliminating a different external momentum leads to in general inequivalent representations of the integral that are not necessarily related by relabelling. To identify all symmetries, in principle all canonical representations with either external momentum eliminated must be considered. However, inserting momentum conservation is the only operation in the canonicalization process that can change the total number of appearing variables and the number of terms. We therefore only consider the representations with the lowest number of variables and, out of those, the representations with the lowest number of terms. Considering these shortest representations only should still identify all matroid symmetries, as long as every vertex connects to at most one external leg.

`Loopedia` considers three different types of masses: Nonzero masses, special masses and general masses. Special masses denote a particular mass for which the integral has been computed. A general mass denotes a mass that can be set to an arbitrary value including zero, while a nonzero mass can take any nonzero value. When searching for symmetries, any relabelling within these three groups of masses must be considered. The squared momenta of the external legs are parameterized as masses out of the same sets as the internal masses; i.e. an internal mass squared and and external momentum squared are interchangeable if they belong to the same class of masses.

After inserting momentum conservation (in all possible ways as discussed in the previous section), the remaining scalar products form the kinematic invariants. These invariants and the Feynman parameters form the remaining sets of equivalent variables where relabellings should be considered.

4.6 Quasi Monte Carlo (QMC) Integration

It has recently been noticed [176], that the numerical integration of sector decomposed functions can be sped up dramatically compared to conventional methods. There are two key new ideas: First, a Quasi Monte Carlo (QMC) algorithm which has a better scaling with the number of samples N than the well known $1/\sqrt{N}$ of Monte Carlo integrators is used. Second, the sector decomposed integrands are evaluated on Graphics Processing Units (GPUs) which is easily possible because only basic arithmetic operations and logarithms are involved.

We briefly summarize the QMC integration method in this section as already published in [184]. We further show that better-than-$1/\sqrt{N}$ scaling is indeed achieved for loop integrals. The reader is referred to Reference [162] for a detailed description of the method and our implementation. An extensive review of the QMC method including proofs of the theorems we use in the following paragraphs can be found e.g. in [195].

4.6.1 Description of the Method

The summary given below is based on the articles [184] and [162]. Consider the $d \in \mathbb{N}$ dimensional integral I_d,

$$\mathrm{I}_d[f] \equiv \int_0^1 \mathrm{d}x_1 ... \int_0^1 \mathrm{d}x_d \; f(\vec{x}), \;\; \vec{x} = (x_1, ..., x_d) \tag{4.39}$$

of a function $f : \; [0,1]^d \to \mathbb{K}, \;\; \mathbb{K} \in \{\mathbb{R}, \mathbb{C}\}$ over the unit hypercube. Shifted rank-1 lattice rules $\bar{Q}_{d,n,m}[f]$ can be used to obtain an unbiased estimate of I_d from a fixed number of sampling points n $\{\vec{x}_j : \vec{x}_j \in [0,1]^d, \;\; j = 1, ..., n\}$ and m random shifts $\{\vec{\Delta}_k \in [0,1)^d : \;\; k = 1, ..., m\}$ as

$$\mathrm{I}_d[f] \approx \bar{Q}_{d,n,m}[f] \equiv \frac{1}{m} \sum_{k=1}^{m} Q_{s,n}^{(k)}[f], \quad Q_{d,n}^{(k)}[f] \equiv \frac{1}{n} \sum_{j=1}^{n} f\left(\left\{ \frac{(j-1)\vec{g}}{n} + \vec{\Delta}_k \right\} \right), \tag{4.40}$$

where $\vec{g} \in \mathbb{N}^d$ is the so-called generating vector and $\{\}$ means taking the fractional part. An unbiased error estimate is given by

$$\sigma^2_{d,n,m}[f] \equiv \mathrm{Var}[\bar{Q}_{d,n,m}[f]] \approx \frac{1}{m(m-1)} \sum_{k=1}^{m} (Q^{(k)}_{s,n}[f] - \bar{Q}_{s,n,m}[f])^2. \tag{4.41}$$

The convergence of the rank-1 lattice rule given in Equation (4.39) depends on the choice of the generating vector $\vec{g}$. In particular, the asymptotic error scaling given below can only be achieved with specific choices of $\vec{g}$. An efficient algorithm to construct good generating vectors is the component-by-component construction [196], where a generating vector in d dimensions is iteratively obtained from a $d-1$ dimensional one by selecting the additional component such that the worst-case error is minimal. Generating vectors obtained in this way are optimized for a fixed lattice size n; i.e. each lattice is associated with its individual optimal generating vector.

It is proven that the error of the QMC estimate of the integral asymptotically scales with the number of lattice points n as $\mathcal{O}(1/n^{s+1})$, where s is the smoothness of the periodically continued integrand[1]

$$\tilde{f} \in C^s(\mathbb{R}^d \to \mathbb{K}), \qquad \tilde{f}(\vec{x}) \equiv f(\{\vec{x}\}). \tag{4.42}$$

Sector decomposed functions are typically infinitely smooth (any derivative is well-defined and finite) but their periodic continuation is typically not. However, there are a number of periodizing transforms implemented via a substitution of the integration variables $\vec{x} \to \vec{z}(\vec{x})$. We focus on the Korobov transform [197–199] of weight α,

$$z_j(x_j) = \int_0^{x_j} \mathrm{d}u\ \omega(u), \qquad \omega(u) = \frac{u^\alpha (1-u)^\alpha}{\int_0^1 \mathrm{d}u'\ u'^\alpha (1-u')^\alpha}, \tag{4.43}$$

and the baker's transform [200] (also known as "tent transformation"),

$$z_j(x_j) = 1 - |2x_j - 1|\,. \tag{4.44}$$

Numerical integration of sector decomposed functions using Sidi's transform [201, 202] of weight α,

$$z_j(x_j) = \int_0^{x_j} \mathrm{d}u\ \omega(u), \qquad \omega(u) = \frac{\sin(\pi u)^\alpha}{\int_0^1 \mathrm{d}u'\ \sin(\pi u')^\alpha}, \tag{4.45}$$

are studied in [203].

The Korobov transform (also Sidi's transform) forces the integrand to go to zero everywhere on the boundary. Due to its structure, it can also be used to map an integral over an integrable divergence (e.g. $1/\sqrt{x}$) to an integral over a finite function.

[1] In fact, the sth derivative of $\tilde{f}$ must be *absolutely continuous*, not only *continuous* as usually suggested by the notation C^s.

Assuming a C^∞ nonperiodic integrand f and an integer weight $\alpha \in \mathbb{N}$, the Korobov transformed and periodically continued integrand $\tilde{f}^{K_\alpha}$ is $C^{\alpha-1}$ for odd α and C^α for even α. This can be seen by examining the derivative of $\tilde{f}^{K_\alpha}$ on the border of the unperiodized transformed integrand f^{K_α}: One finds that the periodization of a high-enough derivative becomes discontinuous. Hence, we expect the relative error of sector decomposed integrals to asymptotically scale like $\mathcal{O}(1/n^\alpha)$ (odd α) or $\mathcal{O}(1/n^{\alpha+1})$ (even α) with the number of QMC lattice points n.

The baker's transform periodizes the integrand by mirroring rather than forcing it to a particular value on the integration boundary. Note that the baker's transform is only C^0 which naively suggests an asymptotic $\mathcal{O}(1/n)$ scaling. However, the asymptotic scaling of the error can be proven to be $\mathcal{O}(1/n^2)$ by considering the baker's transform as a modification of the lattice rather than an integral transform. Further note that the derivative of the baker's transform (where it exists) is plus or minus 2, which leads to a (piecewise) constant Jacobian factor when considered as an integral transform.

4.6.2 Variance Reduction

We improve the plain QMC integration method with an additional variance reducing integral transform similar to the `VEGAS` algorithm [204]. In particular, we consider one-dimensional transforms described by a function $p:\ [0,1] \to [0,1]\,,\ p(0) = 0,\ p(1) = 1$, such that

$$\int_0^1 \mathrm{d}y\ f(y) = \int_0^1 \mathrm{d}x\ \frac{\mathrm{d}p(x)}{\mathrm{d}x}\ f(p(x)). \tag{4.46}$$

As discussed Section 4.6.1, the smoothness of the integrand is crucial for the scaling behavior of the integrand. The `VEGAS` algorithm constructs a piecewise linear function p which leads to a discontinuous derivative $\mathrm{d}p(x)/\mathrm{d}x$ and therefore a discontinuous integrand. Alternatively, we suggest the closed form expression,

$$p(x) \equiv a_2 \cdot x\,\frac{a_0 - 1}{a_0 - x} + a_3 \cdot x\,\frac{a_1 - 1}{a_1 - x} + a_4 \cdot x + a_5 \cdot x^2 + \left(1 - \sum_{i=2}^{5} a_i\right) \cdot x^3, \tag{4.47}$$

with the parameters $a_0, ..., a_5 \in \mathbb{R}$. Note that the ansatz in (4.47) is fulfils $p(0) = 0$ and $p(1) = 1$ regardless of the parameter values. The parameters $a_0, ..., a_5$ are obtained in a fit to the inverse of the cumulative distribution function (CDF),

$$\mathrm{CDF}_f(x) = \int_0^x \mathrm{d}y\ |f(y)| \Big/ \int_0^1 \mathrm{d}y\ |f(y)|; \tag{4.48}$$

To be precise, a set of samples $(x_j, f(x_j))$ is sorted according to x_j and transformed into a set of samples of the CDF $(x_j, CDF_f(x_j))$ by replacing the second entry with the sum of all function values less or equal to x_j. The swapped set of tuples $(x_j, CDF_f(x_j))$ is then used as input data for a least-squares fit as implemented in the GNU Scientific Library [173] to obtain the parameter values $a_0, ..., a_5$. For stability reasons, the restrictions $a_0 \in [1.001, \infty)$, $a_1 \in (-\infty, -0.001]$, and $a_2, a_3 \geq 0$ are imposed.

We find that the ansatz in Equation (4.47) works well for typical functions obtained by sector decomposition. While this ansatz in principle can be applied to other integrals as well, we expect that for other functions it can be beneficial to modify it to improve the fit of the CDF of the corresponding integrand.

4.6.3 Scaling Behavior

It is well known [199] that periodizing transforms often increase the variance of the integrand which makes them impractical in high dimensions. We demonstrate this effect by examining the scaling behavior of the QMC when integrating two finite loop integrals. The integrals are chosen such that the numerical integration over the Feynman parameters is seven and nine dimensional, respectively. We scan the reported integration error of these integrals using the Korobov transform with weight 3 and the baker's transform, with and without the variance reduction technique described in Section 4.6.2. We refer to the Korobov transform with weight 3 as the Korobov transform throughout the following for brevity.

As the seven-dimensional integral, we choose the massless pentabox depicted in Figure 4.7a with on-shell legs evaluated in $D = 6 - 2\varepsilon$ space-time dimensions at the non-Euclidean point $s_{12} = 5$, $s_{23} = -4$, $s_{34} = 2$, $s_{45} = -6$, and $s_{51} = 3$, where the $s_{ij} \equiv (p_i + p_j)^2$ denote the usual Mandelstam invariants.

Our nine dimensional integral is the all-massive four-loop form factor with mass $m \equiv 1$ depicted in Figure 4.7b with one off-shell leg. We set $p_3^2 = 1$ for the numerical evaluation.

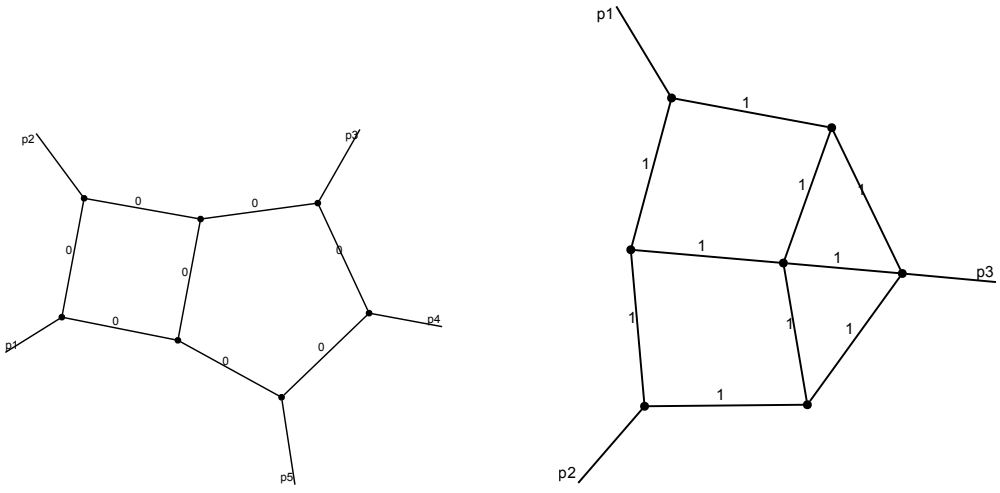

(a) **(b)**

Figure 4.7: Graphical representation of two finite loop integrals leading to a (a) seven and a (b) nine dimensional integral in Feynman parameter space.

The relative error of the finite ($\mathcal{O}(\varepsilon^0)$) real part of the two integrals described above versus the number of lattice points n is shown in Figure 4.8. First, note that the relative error can be orders of magnitude different for neighboring lattices such that assessing the scaling behavior cannot be done straightforwardly with a linear fit. Further note that the scaling becomes better with increasing lattice size. For these two reasons, any attempt of a linear fit would strongly depend on which exact points are included. Rough estimates however show that the asymptotic scaling claimed in Section 4.6.1 is not reached for most of the integrals within the plotted range. The error of the baker-transformed integrand for example reaches better-than-$1/n$ scaling only in the tail of the seven dimensional plot and only without variance reduction (no fit). Within the plotting range, the integration error with variance reduction (fit) is always about at least as good as without, typically up to an order of magnitude better. We further see that the better scaling of the Korobov transformed integrand competes against an increased error with small lattices compared to the baker's transform. The better scaling of the Korobov transform leads to a more accurate result only for large enough lattices and the turnover region moves to larger lattices with an increasing number of dimensions. We also observe that the error is almost independent of the lattice size for small lattices ($n \lesssim 10^4$ for the nine dimensional integral) in combination with the Korobov transform. Despite that region, note that the error scaling is always $1/n$ or better.

The observations stated in the previous paragraph are exemplary for observations we made with other integrals as well. We conclude:

- The better scaling of the Korobov transform can be beneficial in low dimensions $d \lesssim 7$ while the baker's transform performs better in higher dimensions $d \gtrsim 9$ due to the lower error on smaller lattices.
- If the periodizing transform is chosen as suggested above, then the error scales with the lattice size n like $1/n$ or better.
- Using the variance reduction described in Section 4.6.2 can lead to up to an order of magnitude more accurate results. We have however also seen cases where it reduces the accuracy.

4.7 Integral Library for Amplitude Calculations

A major design goal for the development of pySecDec was to allow for the numerical evaluation of the master integrals in amplitude calculations. This use case of the sector decomposition method was pioneered in the NLO(QCD) calculation of the process $gg \to HH$ with full top-quark mass dependence [205, 206]. Therein, the numerical integrands produced by SecDec-3 have been collected into an integral library. The same setup was also used in the NLO(QCD) calculation of the process $gg \to Hg$ with full top-quark mass dependence [207]. An algorithm to minimize the time needed to evaluate the amplitude at one phase-space point with a predefined accuracy has been proposed in [208] and a refined version has been applied in the calculations mentioned above. We review the refined algorithm in this section.

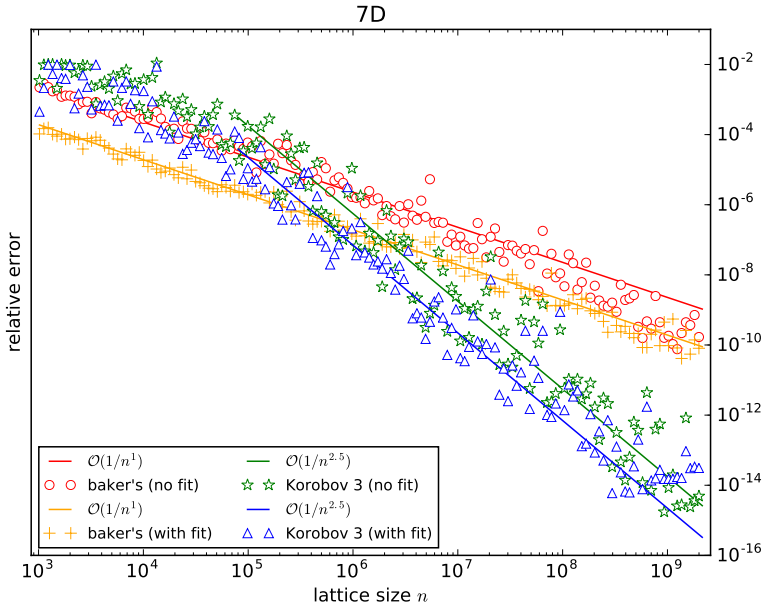

(a)

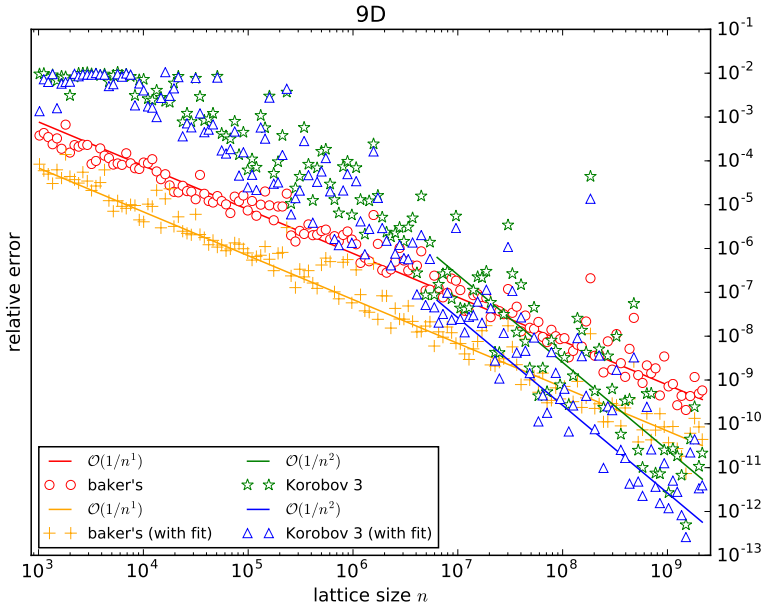

(b)

Figure 4.8: Scaling plots of a (a) seven and a (b) nine dimensional loop integral using different periodizing transforms and optionally the variance reduction (with/no fit) explained in Section 4.6.2. The solid lines are only for guidance and do *not* resemble a fit to the data, see comments in the text.

The goal is to efficiently evaluate a list of expressions A_i of the form

$$A_i = \sum_j k_{ij} \mathcal{I}_j, \tag{4.49}$$

where the k_{ij} are numeric coefficients and the $\mathcal{I}_j$ are integrals to be computed numerically. Such expressions arise e.g. in our multi-loop extension of the program GoSam for the form-factors, see Equation (3.9). Such an algorithm can also be useful to verify an analytic solution of a numerically ill-behaved integral if a reduction rule in terms of numerically better-behaved integrals is known; see also Section 3.2.1.

We assume that the coefficients k_{ij} are evaluated exactly while the integrals $\mathcal{I}_j$ can only be obtained to a numerical accuracy δ_j. The integral error is assumed to scale with the number of sampling points N_j as

$$\delta_j = c_j N_j^{-\alpha_j}, \tag{4.50}$$

where the $c_j > 0$ are constants depending on the intrinsic variance of the integrand and the $\alpha_j > 0$ are integrator-specific scaling exponents. If the integral $\mathcal{I}_j$ is for example computed using a Monte Carlo integrator based on pseudo-random numbers, then $\alpha_j = 1/2$; i.e. the famous $1/\sqrt{N_j}$ Monte Carlo error scaling. We are mostly interested in computing integrals with the QMC integrator (see Section 4.6) where we assume the observed worst-case $\alpha_j = 1$ (see discussion in Section 4.6.3). The time t_j taken to compute the integral $\mathcal{I}_j$ using N_j samples is assumed to be proportional to the number of samples,

$$t_j = d_j N_j, \tag{4.51}$$

where the $d_j > 0$ denote the proportionality constants.

We now specify "efficient" evaluation of the expressions A_i in a more mathematical way: We want to minimize the time,

$$t = \sum_j t_j, \tag{4.52}$$

taken to compute all integrals $\mathcal{I}_j$ such that A_i is known to a certain accuracy

$$\delta_i^2 = \sum_j k_{ij}^2 \delta_j^2, \tag{4.53}$$

where we assumed the integral errors δ_j to be Gaussian distributed as asymptotically guaranteed by the central limit theorem for large N_j.

For reasons that will become clear later, we define the ratios

$$R_{ij} \equiv \frac{t_j}{k_{ij}^2 \delta_j^2} = \frac{d_j}{k_{ij}^2 c_j^2} N_j^{2\alpha_j+1}, \tag{4.54}$$

where the latter formulation is obtained by inserting the definitions of δ_j in (4.50) and of t_j in (4.51) into the expression after the first equal sign.

We are now ready to formulate the optimization problem at hand. The goal is to minimize the run time t_i while the squared error of the amplitude is fixed. We employ the Lagrange-multiplier method to solve this optimization problem under a constraint. The Lagrangian is given by

$$\begin{aligned}\mathcal{L}_i(\{t_j\},\beta_i) &= t_i + \beta_i \left[\sum_j k_{ij}^2 \delta_j^2 - \delta_i^2\right] \\ &= \sum_j t_j + \beta_i \left[\sum_j k_{ij}^2 c_j^2 N_j^{-2\alpha_j} - \delta_i^2\right] \\ &= \sum_j t_j + \beta_i \left[\sum_j k_{ij}^2 c_j^2 \left(\frac{t_j}{d_j}\right)^{-2\alpha_j} - \delta_i^2\right]\end{aligned} \tag{4.55}$$

where β_i denotes the Lagrange multiplier for the condition (4.53). The error goal δ_i on the amplitude is considered as a fixed input parameter.

The extrema are given by setting the gradient of the Lagrangian to zero. In the following, we denote parameters at the optimum and the desired error goals $\hat{\delta}_i$ with a hat. This results in the following system of equations:

$$0 \stackrel{!}{=} \frac{\partial \mathcal{L}}{\partial \hat{t}_j} = 1 - 2\alpha_j \hat{\beta}_i k_{ij}^2 c_j^2 d_j^{2\alpha_j} \hat{t}_j^{-2\alpha_j - 1} \tag{4.56}$$

$$0 \stackrel{!}{=} \frac{\partial \mathcal{L}}{\partial \hat{\beta}_i} = \sum_j k_{ij}^2 c_j^2 \left(\frac{\hat{t}_j}{d_j}\right)^{-2\alpha_j} - \hat{\delta}_i^2. \tag{4.57}$$

We assume that all integrals in an expression A_i are computed with integrators that exhibit the same scaling exponent $\alpha \equiv \alpha_j \forall j$. Eliminating t_j from (4.56) using (4.51) we find by comparison with (4.54)

$$\hat{R}_{ij} = \frac{d_j}{k_{ij}^2 c_j^2} \hat{N}_{ij}^{2\alpha+1} = 2\alpha_i \hat{\beta}_i \equiv \hat{R}_i; \tag{4.58}$$

i.e. the optimized ratios $\hat{R}_{ij}$ are independent of j. Note that the optimal number of samples $\hat{N}_{ij}$ depends on i; i.e. the optimization is specific to a particular expression A_i. Inserting t_j using (4.51) into (4.57), results in

$$\hat{\delta}_i^2 = \sum_j k_{ij}^2 c_j^2 \hat{N}_{ij}^{-2\alpha}, \tag{4.59}$$

where $\hat{\delta}_i$ denotes the error goal for expression A_i.

We could attempt to solve (4.58) and (4.59) for the optimal numbers of samples. In practical applications however, the constants c_j and d_j are typically not known a priori. Instead, we compute the optimal numbers of samples $\hat{N}_{ij}$ from a sample of the integrals $\mathcal{I}_j$ computed with some numbers (not necessarily optimal) of samples $\tilde{N}_j$.

Suppose that the times $\tilde{t}_j$ taken for each integral and the resulting error estimates $\tilde{\delta}_j$ have also been recorded. All quantities derived from the test sample are denoted with a tilde.

We begin by computing the ratios $\tilde{R}_{ij}$ of the test sample as

$$\tilde{R}_{ij} = \frac{\tilde{t}_j}{k_{ij}^2 \tilde{\delta}_j^2}. \tag{4.60}$$

The optimal numbers of samples $\hat{N}_{ij}$ can be rewritten as rescalings of the numbers of samples that were used in the test sample $\tilde{N}_j$,

$$\hat{N}_{ij} \equiv \hat{R}_i^{\frac{1}{2\alpha+1}} \xi_{ij} \tilde{N}_j, \tag{4.61}$$

where we introduce the helper constants $\xi_{ij} > 0$. We find for the helper constants

$$\xi_{ij} = \frac{\hat{N}_{ij}}{\tilde{N}_j} \hat{R}_i^{-\frac{1}{2\alpha+1}} = \tilde{R}_{ij}^{-\frac{1}{2\alpha+1}}, \tag{4.62}$$

by noting that

$$\frac{\hat{R}_i}{\tilde{R}_{ij}} = \frac{\hat{R}_{ij}}{\tilde{R}_{ij}} = \left(\frac{\hat{N}_{ij}}{\tilde{N}_j} \right)^{2\alpha+1} \tag{4.63}$$

which is implied by (4.58) and (4.54).

The optimized ratio $\hat{R}_i$ can be fixed by the error goal $\hat{\delta}_i^2$: By inserting (4.61) into (4.59),

$$\hat{\delta}_i^2 = \hat{R}_i^{\frac{-2\alpha}{2\alpha+1}} \sum_j k_{ij}^2 c_j^2 (\xi_{ij} \tilde{N}_j)^{-2\alpha}, \tag{4.64}$$

we notice that the dependence on the unknown constant $\hat{R}_i$ factorizes out of the sum on the right hand side. We can compute that sum using only known numbers as

$$s_i^2 \equiv \sum_j k_{ij}^2 \tilde{\delta}_j^2 \xi_{ij}^{-2\alpha}, \tag{4.65}$$

where we have eliminated the unknown constants c_j using (4.50). The unknown parameter $\hat{R}_i$ is obtained by dividing the error goal by the sum s_i^2,

$$\hat{R}_i = \left(\frac{\hat{\delta}_i^2}{s_i^2} \right)^{-\frac{2\alpha+1}{2\alpha}}. \tag{4.66}$$

The algorithm to find the optimal numbers of samples $\hat{N}_{ij}$ for a single expression A_i from a test sample is therefore summarized as follows:

1. Compute the ratios $\tilde{R}_{ij}$ according to (4.60).
2. Compute the helper constants ξ_{ij} using the last term in (4.62).

3. Compute the sum s_i^2 using (4.65).
4. Compute the optimal ratio $\hat{R}_i$ using (4.66).
5. The optimal numbers of samples $\hat{N}_{ij}$ are given by (4.61).

The algorithm is further improved by taking into account that integrals, which are already computed to sufficient accuracy or better, should not be recomputed with less samples. The algorithm described above would find $\xi_{ij}\hat{R}_i^{\frac{1}{2\alpha+1}} \leq 1$ for these integrals. We therefore repeatedly refine s_i^2 and $\hat{R}_i$, after having a first estimate from (4.66), as

$$s_i^2 \leftarrow \sum_j k_{ij}^2 \tilde{\delta}_j^2 \begin{cases} (\xi_{ij}\hat{R}_i^{\frac{1}{2\alpha+1}})^{-2\alpha} & \xi_{ij}\hat{R}_i^{\frac{1}{2\alpha+1}} > 1 \\ 1 & \text{else} \end{cases} \tag{4.67}$$

$$\hat{R}_i \leftarrow \hat{R}_i \left(\frac{\hat{\delta}_i^2}{s_i^2}\right)^{-\frac{2\alpha+1}{2\alpha}} \tag{4.68}$$

until the value of $\hat{R}_i$ does not change any more. As a result, less samples for some integrals and therefore less time may be needed to reach the error goal $\hat{\delta}_i^2$.

To simultaneously compute multiple expressions A_i depending on a common set of integrals $\mathcal{I}_j$, we currently run the algorithm described above for each of the expressions separately. The integrals are then evaluated with the maximal number of samples

$$\hat{N}_j \equiv \max_i \hat{N}_{ij}, \tag{4.69}$$

such that all error goals $\hat{\delta}_i^2$ are fulfilled assuming the error scaling (4.59) is valid. An obvious possible improvement would be minimizing the time considering all expressions simultaneously. We leave that task for future investigation.

Part III

LHC Phenomenology

5 Production of Two Photons in the Gluon-Fusion Channel

This Chapter is based on the publication [209].

The production of pairs of photons in hadronic collisions has attracted interest from both, the experimental and the theory side, for several decades. Most prominently, the diphoton final state served as one of the key discovery channels for the Higgs boson [210, 211], which can decay into two photons. As a very clean experimental channel, it is also well suited for precision studies of the Standard Model (SM) and in particular the Higgs sector. For example, there is the possibility to constrain the Higgs boson width from interference effects of the continuum $gg \to \gamma\gamma$ with the signal $gg \to H \to \gamma\gamma$ [212–219]. Furthermore, various new-physics models predict the production of photon pairs, where the study of angular correlations between the decay photons can provide information about the spin of the underlying resonances [220, 221].

Another interesting aspect of diphoton production is the possibility of measuring the top-quark mass via the top-quark pair-production threshold effects manifest in the diphoton invariant-mass spectrum [222, 223]. While current LHC measurements [210, 211] are not yet able to provide the necessary statistics for such a threshold scan, the feasibility at the High-Luminosity LHC, and even more so at a future 100 TeV collider, is worth investigating.

This Chapter is structured as follows: A summary of earlier calculations is given in Section 5.1. In Section 5.2, we describe our calculation of the NLO corrections including both, massless and massive fermion loops. Section 5.3 contains a description of our treatment of the top-quark pair-production threshold region. In Section 5.4, we present our numerical results and an outlook on the possibility to measure the top-quark mass from the diphoton spectrum.

5.1 Introduction

Direct diphoton production[1] in hadronic collisions occurs via the leading-order ($\mathcal{O}(\alpha_s^0)$) process $q\bar{q} \to \gamma\gamma$. The next-to-leading order corrections to this process, including fragmentation contributions, have been calculated and implemented in the public program `Diphox` [224].

We only consider the loop-induced gluon-fusion channel $gg \to \gamma\gamma$ in this Thesis, which enters as a next-to-next-to-leading order ($\mathcal{O}(\alpha_s^2)$) correction to the $pp \to \gamma\gamma$ cross-section. The process $gg \to \gamma\gamma$ has been calculated at LO including both, massless and

[1] We denote by "direct photons" the photons produced directly in the hard-scattering process, as opposed to photons originating from a hadron-fragmentation process.

massive quark loops, in [212] and is included in `Diphox` at the one-loop order for massless quark loops. Even though the $gg \to \gamma\gamma$ contribution is a higher-order correction to the total $pp \to \gamma\gamma$ cross-section, its contribution is similar in size to the LO result at the LHC, due to the large gluon luminosity. A calculation that also includes the effects of transverse-momentum resummation to direct photon production is implemented in the program `ResBos` [225].

NLO(QCD) corrections to the gluon-fusion channel with massless quarks, i.e. $\mathcal{O}(\alpha_s^3)$ corrections, were first calculated in [226, 227] and implemented in the code 2γ`MC` [227] as well as in `MCFM` [118]. Very recently, the NLO(QCD) corrections to the gluon-fusion channel including massive top-quark loops have become available [228], where the master integrals have been calculated numerically based on the numerical solution of differential equations [139, 229]. Analytic results for the planar two-loop box integrals with massive top quarks have been presented in [230, 231]. Regarding the non-planar contributions, 3-point topologies containing elliptic integrals were calculated in [232, 233]. Other 3-point topologies have been calculated earlier in the context of Higgs production and decay [234, 235].

The NNLO(QCD) corrections to the process $pp \to \gamma\gamma$ were first calculated in [236], including the $gg \to \gamma\gamma$ contribution at order α_s^2 with massless quark loops; for a phenomenological study see also [237]. The NNLO(QCD) corrections to $pp \to \gamma\gamma$ have also been calculated and implemented in `MCFM` [238], supplemented by the gg initiated loops proportional to n_f at LO and NLO for five massless quark flavors and at LO for massive top-quark loops. Diphoton production at NNLO with massless quarks is also available in Matrix [239].

The aim of this work is twofold: First, we provide an independent calculation of the QCD corrections to the process $gg \to \gamma\gamma$ including massive top-quark loops (see Figure 5.1) confirming the results of [228] for the central scale choice. Second, we combine our results with a threshold resummation as advocated in [223] such that the top-quark pair-production threshold region in the diphoton invariant-mass spectrum can be predicted with high accuracy. The calculation can thus serve as a starting point for investigating the possibility of a top-quark mass measurement from the diphoton invariant-mass spectrum.

5.2 Building Blocks of the Fixed-Order Calculation

We consider the following scattering process,

$$g(p_1, \lambda_1, a_1) + g(p_2, \lambda_2, a_2) \to \gamma(p_3, \lambda_3) + \gamma(p_4, \lambda_4), \tag{5.1}$$

with on-shell conditions $p_j^2 = 0, j = 1, ..., 4$. The helicities λ_i of the external particles are defined by taking the momenta of the gluons p_1 and p_2 (with color indices a_1 and a_2, respectively) as incoming and the momenta of the photons p_3 and p_4 as outgoing. The Mandelstam invariants associated with Equation (5.1) are defined by

$$s = (p_1 + p_2)^2, \qquad t = (p_2 - p_3)^2, \qquad u = (p_1 - p_3)^2. \tag{5.2}$$

5.2.1 Projection Operators

We define the tensor amplitude $\mathcal{M}_{\mu_1\mu_2\mu_3\mu_4}$ by extracting the polarization vectors from the amplitude $\mathcal{M}$,

$$\mathcal{M} = \varepsilon^{\mu_1}_{\lambda_1}(p_1)\,\varepsilon^{\mu_2}_{\lambda_2}(p_2)\,\varepsilon^{\mu_3,\star}_{\lambda_3}(p_3)\,\varepsilon^{\mu_4,\star}_{\lambda_4}(p_4)\,\mathcal{M}_{\mu_1\mu_2\mu_3\mu_4}(p_1,p_2,p_3,p_4), \tag{5.3}$$

where the $\varepsilon^{\mu_i}_{\lambda_i}$ denote the polarization vectors. The amplitude is computed through projection onto a set of Lorentz structures related to linear polarization states of the external massless bosons. An appropriate set of D-dimensional projection operators is constructed following the approach proposed in [240] which we will summarize briefly in the following.

A physical polarization vector $\varepsilon(p)$ of a massless vector boson with (on-shell) momentum p fulfils the transversality and (imposed) normalization conditions,

$$\varepsilon(p)\cdot p = 0, \quad \varepsilon(p)\cdot\varepsilon(p) = -1. \tag{5.4}$$

These conditions fix two components of the polarization vectors in four space-time dimensions. We explicitly construct a basis of the space of polarization states defined by (5.4) for the external massless vector bosons in the following. First, we introduce a polarization basis vector ε_X valid for both initial-state gluons, which can be written in terms of the linearly independent momenta of the process

$$\varepsilon^{\mu}_X = c_1^X\, p_1^\mu + c_2^X\, p_2^\mu + c_3^X\, p_3^\mu, \tag{5.5}$$

where the constants c_i^X are determined by the system of equations

$$\varepsilon_X\cdot p_1 = 0, \qquad \varepsilon_X\cdot p_2 = 0, \qquad \varepsilon_X\cdot\varepsilon_X = -1. \tag{5.6}$$

Note that the definitions above constitute a gauge choice in which the reference momentum of either incoming gluon is set to be the momentum of the other gluon. A polarization vector ε_T for both outgoing photons can be constructed analogously,

$$\varepsilon_T\cdot p_3 = 0, \qquad \varepsilon_T\cdot p_4 = 0, \qquad \varepsilon_T\cdot\varepsilon_T = -1. \tag{5.7}$$

A third basis vector ε_Y, pointing out of the scattering plane, is needed to span the space of all possible polarization vectors for this process,

$$\varepsilon_Y\cdot p_i = 0, \qquad i\in\{1,\ldots,4\}\,. \tag{5.8}$$

In four dimensions, such a vector can be constructed using the Levi-Civita tensor,

$$\varepsilon^{\mu}_Y = \varepsilon^{\mu\nu\rho\sigma} p_{1\nu}\, p_{2\rho}\, p_{3\sigma}. \tag{5.9}$$

Since we consider only QCD corrections to a QED process, neither γ_5 nor Levi-Civita tensors are introduced by the relevant Feynman rules. Consequently, a completely D-dimensional tensor decomposition of this scattering amplitude can be expressed solely in terms of metric tensors and external momenta. Therefore, a contraction of the tensor

amplitude with an odd number of ε_Y evaluates to zero. A product of two Levi-Civita tensors, however, can be rewritten in terms of metric tensors (see (3.8)) which has a straightforward D-dimensional continuation. For a detailed discussion of the subtleties related to the manipulation of Levi-Civita tensors in the construction of projectors for more general cases we refer to Reference [240].

Applied to the scattering process (5.1), this construction leads to eight projectors

$$\varepsilon^{\mu}_{[X,Y]}\varepsilon^{\nu}_{[X,Y]}\varepsilon^{\rho}_{[T,Y]}\varepsilon^{\sigma}_{[T,Y]}, \tag{5.10}$$

where the square bracket $[\cdot,\cdot]$ means either entry and where only the combinations containing an even number of ε_Y are considered. Let us emphasize again that, in order to avoid possible ambiguities in the application of these projectors, all pairs of Levi-Civita tensors are replaced according to the contraction rule (3.8) *before* being used for the projection of the amplitude. Then, the aforementioned projectors are expressed solely in terms of external momenta and metric tensors whose open Lorentz indices are all set to be D-dimensional.

The usual helicity amplitudes can be constructed as circular polarization states from the linear ones as

$$\begin{aligned} \varepsilon_{\pm}(p_1)^{\mu} &= \frac{1}{\sqrt{2}}\left(\varepsilon_X^{\mu} \pm i\varepsilon_Y^{\mu}\right), \qquad & \varepsilon_{\pm}(p_2)^{\nu} &= \frac{1}{\sqrt{2}}\left(\varepsilon_X^{\nu} \mp i\varepsilon_Y^{\nu}\right), \\ \varepsilon_{\pm}(p_3)^{\rho} &= \frac{1}{\sqrt{2}}\left(\varepsilon_T^{\rho} \pm i\varepsilon_Y^{\rho}\right), \qquad & \varepsilon_{\pm}(p_4)^{\sigma} &= \frac{1}{\sqrt{2}}\left(\varepsilon_T^{\sigma} \mp i\varepsilon_Y^{\sigma}\right). \end{aligned} \tag{5.11}$$

Analytic results for the LO amplitudes of (5.1) were obtained quite some time ago for massless quark-loop contributions [241–243] and with massive quark-loop contributions [244, 245]. With the linear-polarization projectors defined in (5.10), we recomputed these LO amplitudes analytically with both, massless and massive quark loops. We have implemented the analytic expressions for the LO amplitude in our computational setup for the NLO(QCD) corrections to the considered process, which we describe below.

5.2.2 UV Renormalization

The bare scattering amplitudes of the process (5.1) denoted by $\hat{\mathcal{M}}$ contain poles in the dimensional regulator $\epsilon \equiv (4-D)/2$ beyond LO, arising from ultraviolet (UV) as well as soft and collinear (IR) regions of the loop momenta. In our computation, we renormalize these UV divergences using the $\overline{\text{MS}}$ scheme, except for the top-quark mass which is renormalized on-shell.

The bare virtual amplitude $\hat{\mathcal{M}}$ is a function of the bare QCD coupling $\hat{\alpha}_s$ and the bare top-quark mass $\hat{m}_t$. The UV renormalization of $\hat{\mathcal{M}}$ is achieved by renormalizing the gluon wave function and by the replacement

$$\hat{\alpha}_s\,\hat{\mu}^{2\epsilon}\,S_\epsilon = \alpha_s\,\mu_R^{2\epsilon}\,Z_a\ ,\ \hat{m}_t = m_t\,Z_m, \tag{5.12}$$

where $S_\epsilon = (4\pi)^\epsilon\,e^{-\epsilon\gamma_E}$ with the Euler–Mascheroni constant γ_E. The strong coupling is given by $\alpha_s = g_s^2/(4\pi)$ and $\hat{\mu}$ is an auxiliary mass-dimensionful parameter introduced

in dimensional regularization to keep the (bare and renormalized) coupling constants dimensionless. The usual renormalization scale is denoted μ_R, we will use $\hat{\mu} = \mu_R$ in the following.

Both, the bare virtual amplitudes and the UV renormalization constants, are expanded in $a_s \equiv \alpha_s(\mu_R)/(4\pi)$. We may write the renormalization constants as

$$Z_i = 1 + a_s\, \delta Z_i + O(a_s^2), \qquad i = a, A, m. \tag{5.13}$$

Under the $\overline{\text{MS}}$ scheme for α_s with n_f massless quark flavors and top-quark loops renormalized on-shell, the renormalization constants needed in our computation read

$$\begin{aligned}
\delta Z_a &= -\frac{1}{\epsilon}\,\beta_0 + \left(\frac{\mu_R^2}{m_t^2}\right)^{\epsilon} \frac{4}{3\epsilon}\, T_R, \\
\delta Z_A &= \left(\frac{\mu_R^2}{m_t^2}\right)^{\epsilon} \left(-\frac{4}{3\epsilon}\, T_R\right), \\
\delta Z_m &= \left(\frac{\mu_R^2}{m_t^2}\right)^{\epsilon} C_F \left(-\frac{3}{\epsilon} - 4\right),
\end{aligned} \tag{5.14}$$

with

$$\beta_0 = \frac{11}{3} C_A - \frac{4}{3}\, T_R\, n_f. \tag{5.15}$$

We write the scattering amplitude for the process $gg \to \gamma\gamma$ up to second order in a_s in the following form

$$\begin{aligned}
\hat{\mathcal{M}} =& \hat{a}_s \hat{\mathcal{M}}_B(\hat{m}_t) + \hat{a}_s^2 \hat{\mathcal{M}}_V(\hat{m}_t) + \mathcal{O}(\hat{a}_s^3) \\
=& a_s\, \mathcal{M}_{B,\text{ren}}(m_t) + a_s^2\, \mathcal{M}_{V,\text{ren}}(m_t) + \mathcal{O}(a_s^3),
\end{aligned} \tag{5.16}$$

where

$$\begin{aligned}
\mathcal{M}_{B,\text{ren}}(m_t) =& S_\epsilon^{-1} \hat{\mathcal{M}}_B(\hat{m}_t) \\
\mathcal{M}_{V,\text{ren}}(m_t) =& S_\epsilon^{-2} \hat{\mathcal{M}}_V(\hat{m}_t) - \frac{\beta_0}{\epsilon} S_\epsilon^{-1} \hat{\mathcal{M}}_B(\hat{m}_t) + \delta Z_m\, \hat{\mathcal{M}}_{CT}(\hat{m}_t).
\end{aligned} \tag{5.17}$$

Here, $\mathcal{M}_{B,\text{ren}}(m_t)$ and $\mathcal{M}_{V,\text{ren}}(m_t)$ are the one-loop and UV renormalized two-loop amplitudes, respectively, with the Born kinematics given in (5.1). The mass counter-term amplitude $\hat{\mathcal{M}}_{CT}(\hat{m}_t)$ is obtained by inserting a mass counter-term into the heavy quark propagators

$$\Pi_{ab}^{\delta_m}(p) = \frac{i\delta_{ac}}{\not{p} - m}(-i\delta Z_m)\frac{i\delta_{cb}}{\not{p} - m}, \tag{5.18}$$

where a, b, c are color indices in the fundamental representation. The mass counter-term can also be obtained by taking the derivative of the one-loop amplitude with respect to $\hat{m}_t$.

5.2.3 Definition of the IR-subtracted Virtual Amplitude

The UV renormalized virtual amplitude $\mathcal{M}_{V,\text{ren}}$ still contains divergences arising from soft and collinear configurations of the loop momenta, which appear as poles in the dimensional regulator. We employ the FKS subtraction approach [47] to deal with the intermediate IR divergences, as implemented in the POWHEG-BOX-V2 framework [63, 64, 101].

For the process $gg \to \gamma\gamma$, the corresponding integrated subtraction operator is given by

$$I_1(\mu_R^2, s) = \frac{S_\epsilon^{-1}}{\Gamma(1-\epsilon)} \left[\frac{2C_A}{\epsilon^2} + \frac{2\beta_0}{\epsilon} + \frac{2C_A}{\epsilon} \ln\left(\frac{\mu_R^2}{s}\right) \right]. \tag{5.19}$$

To second order in a_s, the UV-renormalized and IR-subtracted virtual amplitude is given by

$$\begin{aligned} \mathcal{M}_B =& \mathcal{M}_{B,\text{ren}}, \\ \mathcal{M}_V =& \mathcal{M}_{V,\text{ren}} + I_1(\mu_R^2, s)\, \mathcal{M}_{B,\text{ren}}. \end{aligned} \tag{5.20}$$

Note that the LO amplitude $\mathcal{M}_{B,\text{ren}}$ needs to be computed to $\mathcal{O}(\epsilon^2)$ as it is multiplied by coefficients containing $1/\epsilon^2$ poles.

In practice, we need to supply only the finite part of the born-virtual interference, under a specific definition [101] in order to combine it with the FKS-subtracted real radiation generated within the GoSam/POWHEG-BOX-V2 framework. Explicitly, we compute

$$\mathcal{V}_{\text{fin}}(\mu_R) = a_s^2(\mu_R)\, \text{Re}\left[\mathcal{M}_V \mathcal{M}_B^\dagger\right]. \tag{5.21}$$

The renormalization-scale dependence of $\mathcal{V}_{\text{fin}}$ can be derived from the above definitions, it is given by

$$\mathcal{V}_{\text{fin}}(\mu_R) = \mathcal{V}_{\text{fin}}(\mu_0) \left(\frac{a_s(\mu_R)}{a_s(\mu_0)}\right)^2 + \left[C_A \log^2\left(\frac{\mu_0^2}{s}\right) - C_A \log^2\left(\frac{\mu_R^2}{s}\right)\right] a_s^2(\mu_R)\, |\mathcal{M}_B|^2, \tag{5.22}$$

where μ_0 denotes an arbitrarily chosen initial renormalization scale.

5.2.4 Evaluation of the Virtual Amplitude

For the two-loop QCD diagrams contributing to our scattering process, there is a complete separation of quark flavors due to the color algebra and Furry's theorem. Consequently we have $n_f + 1$ sets of two-loop diagrams which can be treated independently. The two-loop amplitude has been obtained with the multi-loop extension of the program GoSam (see Chapter 3) where Reduze 2 [148] is employed for the reduction to master integrals. In particular, each of the linearly polarized amplitudes projected out using (5.10) is eventually expressed as a linear combination of 39 massless integrals and 171 integrals, distributed into three integral families, that depend on the

top-quark mass. All massless two-loop master integrals involved are known analytically [226, 243, 246], and we have implemented the analytic expressions into our code. Regarding the two-loop massive integrals which are not yet fully known analytically, we first rotate to an integral basis consisting partly of quasi-finite loop integrals [132]. Our integral basis is chosen such that the second Symanzik polynomial $\mathcal{F}$ appearing in the Feynman representation of each of the integrals is raised to a power n, where $|n| \leq 1$ in the limit $\epsilon \to 0$. This choice improves the numerical stability of our calculation near to the $t\bar{t}$ threshold, where the $\mathcal{F}$ polynomial can vanish. The integrals are then evaluated numerically using pySecDec [161, 162] (see also Chapter 4). Examples of contributing two-loop Feynman diagrams are shown in Figure 5.1.

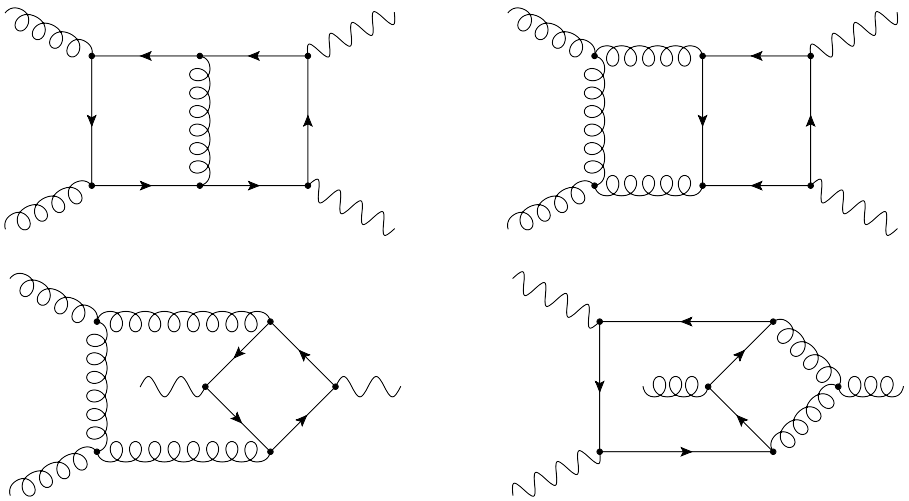

Figure 5.1: Examples of diagrams contributing to the virtual corrections.

The phase-space integration of $\mathcal{V}_{\text{fin}}$ is achieved by reweighting unweighted Born events. The accuracy goal imposed on the numerical evaluation of the virtual two-loop amplitudes in the linear polarization basis in pySecDec is 1 per-mille on both, the relative and the absolute error. We have collected 6898 phase-space points out of which 862 points fall into the diphoton invariant-mass window $m_{\gamma\gamma} \in [330, 360]$ GeV. We further have calculated the amplitudes for 2578 more points restricted to the threshold region.

5.2.5 Computation of the Real-Radiation Contributions

The real-radiation matrix elements are calculated using the interface [247] between GoSam [65, 66] and the `POWHEG-BOX-V2` [63, 64, 101], modified accordingly to compute the real-radiation corrections to loop-induced Born amplitudes. Only real-radiation contributions that contain a closed quark loop at the amplitude level are included. We also include the $q\bar{q}$-initiated diagrams which contain a closed quark loop, even though their contribution is numerically very small. Examples of Feynman diagrams

contributing to the real-radiation amplitude are shown in Figure 5.2. The diagrams in which one of the photons is radiated off a closed fermion loop and the other photon is radiated off an external quark line vanish due to Furry's theorem.

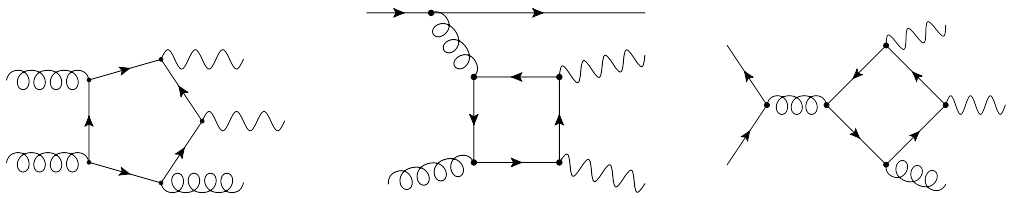

Figure 5.2: Examples of diagrams contributing to the real radiation part.

5.3 The Threshold Region Improved with Non-Relativistic QCD

When the partonic center-of-mass energy is close to the threshold for the production of a $t\bar{t}$ pair, then the top quarks are produced with a non-relativistic velocity $\beta \ll 1$ such that Coulomb interactions between the top quarks can play a significant role. In the case of the top-loop induced contribution to diphoton production, the Coulomb singularity appears in the form of a logarithmic dependence on the velocity, first at two-loop order due to the exchange of a soft gluon between the top quarks in the loop. To overcome this issue and correctly describe the threshold, we employ the so-called non-relativistic QCD (NRQCD) [248–251], which is an effective field theory designed to describe non-relativistic heavy quark-antiquark systems in the threshold region.

5.3.1 NRQCD Amplitude

To the order which we consider here, the amplitude can be expressed as a coherent sum of light quark loop contributions and the top-quark loop contributions,

$$\mathcal{M}(p_i, \lambda_i, a_1, a_2) = 8\alpha_e\alpha_s \, T_R \, \delta^{a_1 a_2} \left[\left(\sum_q Q_q^2 \right) \mathrm{M}_q(s,t) + Q_t^2 \, \mathrm{M}_t(s,t) \right], \tag{5.23}$$

where $\alpha_e = e^2/(4\pi)$ and Q_q denotes the electric charge of quark q. In our computation, the NRQCD expansion of the amplitude M_t near the $t\bar{t}$ threshold is performed according to the formalism explained in more detail in Refs. [223, 252]. Near the production threshold of an intermediate $t\bar{t}$ pair, $m_{\gamma\gamma} \simeq 2m_t$, we define

$$E \equiv m_{\gamma\gamma} - 2m_t, \qquad \beta \equiv \sqrt{1 - 4m_t^2/m_{\gamma\gamma}^2 + i\delta}, \tag{5.24}$$

and the scattering angle θ is given by

$$\cos\theta = 1 + t\,(1-\beta^2)/(2\,m_t^2). \tag{5.25}$$

Close to threshold, the amplitude M_t can be parametrized as [223, 252]

$$\mathrm{M}_t^{\mathrm{NR}} = \mathcal{A}_t(\theta) + \mathcal{B}_t(\beta)\, G(\vec{0};\mathcal{E}) + \mathcal{O}(\beta^3), \tag{5.26}$$

where $\mathcal{E} = E + i\Gamma_t$ includes the top-quark decay width ${\Gamma_t}^2$. Note that the P-wave contribution $\mathcal{B}_{t,P}(\beta)\, G_P(\vec{0};\mathcal{E})$ starts at $\mathcal{O}(\beta^3)$. In this parametrization, the amplitude $\mathrm{M}_t^{\mathrm{NR}}$ is split into two parts: $\mathcal{B}_t(\beta)\, G(\vec{0};\mathcal{E})$ which contains the $t\bar{t}$ bound state effects, and $\mathcal{A}_t(\theta)$ which does not. The term $\mathcal{B}_t(\beta)\, G(\vec{0};\mathcal{E})$ contains the effects from resumming the non-relativistic static-potential interactions, where the Green's function $G(\vec{0};\mathcal{E})$ is obtained by solving the non-relativistic Schrödinger equation describing a color-singlet $t\bar{t}$ bound state,

$$\left(-\frac{\nabla^2}{m_t} + V(r) - \mathcal{E}\right) G(\vec{r};\mathcal{E}) = \delta(\vec{r}), \tag{5.27}$$

with the QCD static potential [254, 255]

$$V(r) = -C_F \frac{\alpha_s(\mu)}{r}\left(1 + \frac{\alpha_s(\mu)}{4\pi}\left(2\beta_0\left(\ln(\mu\, r) + \gamma_E\right) + \frac{31}{9}C_A - \frac{10}{9}n_f\right)\right) + \mathcal{O}(\alpha_s^3)\,. \tag{5.28}$$

The mass m_t appearing in (5.27) is the pole mass of the top quark. $G(\vec{0};\mathcal{E})$ is the $r \to 0$ limit of the Green's function $G(\vec{r};\mathcal{E})$. The real part of the NLO Green's function at $r = 0$ is divergent and therefore has to be renormalized. We adopt the $\overline{\mathrm{MS}}$ scheme thus introducing a scale μ into the renormalized Green's function [256–259]. The coefficient $\mathcal{B}_t(\beta)$ can be obtained from the Wilson coefficients of the $ggt\bar{t}$ and $\gamma\gamma t\bar{t}$ operators [223] in the NRQCD effective Lagrangian for the process $gg \to \gamma\gamma$. The term $\mathcal{A}_t(\theta)$ encompasses the non-resonant corrections, resulting from quark loops with large virtuality which can be systematically computed order by order in α_s.

Both, $\mathcal{A}_t$ and $\mathcal{B}_t$ can be expanded perturbatively in α_s. For the process $gg \to \gamma\gamma$, corrections to $\mathcal{B}_t$ have been calculated up to $\mathcal{O}(\alpha_s)$ and $\mathcal{O}(\beta^2)$ in [223], where explicit expressions of $\mathcal{B}_t$ at the leading order for all relevant helicity configurations can be found. Here we repeat, for completeness, the expressions for the S–wave $t\bar{t}$ resonance we are considering.

For the S–wave, the $\mathcal{B}_t$ coefficients are independent of the scattering angle. We use the notation $G(\beta) \equiv G(\vec{0}; E)$ and

$$\begin{aligned} M_{t,\{\lambda_i\}}^{\mathrm{NR}} &= \mathcal{A}_{t,\{\lambda_i\}}(\theta) + \mathcal{B}_{t,\{\lambda_i\}}(\beta)\, G(\beta) \\ &= M_{t,\{\lambda_i\}}^{\mathrm{NR},(0)} + \frac{\alpha_s}{\pi}\, M_{t,\{\lambda_i\}}^{\mathrm{NR},(1)} + \mathcal{O}(\alpha_s^2). \end{aligned} \tag{5.29}$$

Note that an overall factor of α_s has already been extracted from the amplitude (see Equation (5.23)), such that the $\mathcal{O}(\alpha_s)$ term in the expression (5.29) contains the two-loop amplitude. The NLO part of M_t^{NR}, denoted by $M_t^{\mathrm{NR},(1)}$, can be expanded as

$$M_t^{\mathrm{NR},(1)} = A_t^{(1)}(\theta) + B_t^{(1)}(\beta) G^{(0)}(\beta) + B_t^{(0)}(\beta) G^{(1)}(\beta). \tag{5.30}$$

[2] It has been shown in [253] that in the non-relativistic limit the top width can be consistently included by calculating the cross-section for stable top quarks supplemented by such a replacement up to next-to-leading-order according to the NRQCD power counting.

The expression for $B_t^{(n)}$ can be further expanded in β,

$$B_t^{(n)}(\beta) = b^{(n)} + \beta^2\,\tilde{b}^{(n)} + \mathcal{O}(\beta^3), \tag{5.31}$$

where [223, 260–262]

$$\begin{aligned}
b^{(0)}_{\{\lambda_i\}} &= -\frac{4\pi^2}{m_t^2}\,\lambda_1\lambda_3\,\delta_{\lambda_1\lambda_2}\delta_{\lambda_3\lambda_4},\\
\tilde{b}^{(0)}_{\{\lambda_i\}} &= -\frac{16\pi^2}{3m_t^2}\,\lambda_1\lambda_3\,\delta_{\lambda_1\lambda_2}\delta_{\lambda_3\lambda_4},\\
b^{(1)}_{\{\lambda_i\}} &= b^{(0)}_{\{\lambda_i\}}\,b_1,\ \tilde{b}^{(1)}_{\{\lambda_i\}} = \tilde{b}^{(0)}_{\{\lambda_i\}}\,b_1,\\
b_1 &= C_F\left(-5+\frac{\pi^2}{4}\right) + \frac{C_A}{2}\left(1+\frac{\pi^2}{12}\right) + \frac{\beta_0}{2}\ln\left(\frac{\mu}{2m_t}\right).
\end{aligned} \tag{5.32}$$

The expansion of the Green's function in α_s is given by

$$G(\beta) = G^{(0)}(\beta) + \frac{\alpha_s}{\pi}G^{(1)}(\beta,\mu) + \mathcal{O}(\alpha_s^2), \tag{5.33}$$

where [259, 263]

$$G^{(0)}(\beta) = i\,\frac{m_t^2}{4\pi}(\beta+\beta^3) + \mathcal{O}(\beta^5), \tag{5.34}$$

$$\begin{aligned}
G^{(1)}(\beta,\mu) =& \frac{m_t^2}{8}\,C_F\left(1 - 2\ln(-i\beta) + 2\ln(\frac{\mu}{2m_t}) + \beta^2\,[1 - 4\ln(-i\beta) + 4\ln(\frac{\mu}{2m_t})]\right.\\
&\left. + i\beta^3\frac{16}{3\pi}\,[2c_{us} + 2\ln(-i\beta) - \ln(\frac{\mu}{2m_t})]\right) + \mathcal{O}(\beta^4),
\end{aligned} \tag{5.35}$$

$$c_{us} = -\frac{7}{4} + \ln 2.$$

For $\mathcal{A}_t(\theta)$, we can make use of a partial-wave decomposition in terms of Wigner functions $d^J_{hh'}(\theta)$,

$$\mathcal{A}_{t,\{\lambda_i\}}(\theta) = \sum_{J=0}^{\infty}(2J+1)\mathcal{A}^J_{t,\{\lambda_i\}}d^J_{hh'}(\theta), \tag{5.36}$$

where $h = -\lambda_1 + \lambda_2$ and $h' = \lambda_3 - \lambda_4$.

5.3.2 Matched Amplitude

We would like to retain NRQCD resummation effects and, at the same time, keep the cross-section accurate up to NLO in the fixed-order power counting. We define the "NRQCD-matched" amplitude as [223]

$$\mathrm{M}_t^{\mathrm{match}} \equiv \mathrm{M}_t + \mathcal{B}_t\,G(\vec{0};\mathcal{E}) - \mathrm{M}_{\mathrm{OC}}, \tag{5.37}$$

where the first term is the fixed-order amplitude, the second term describes the threshold according to NRQCD, and the third term $\mathrm{M_{OC}} \equiv \mathcal{B}_t\, G(\vec{0}; E)$ subtracts double-counted contributions included in both, the fixed-order amplitude and NRQCD contribution. The term $\mathrm{M_{OC}}$, in a fixed-order computation, should be expanded to the same order as the fixed-order amplitude.

Expanding (5.37) to next-to-leading order in α_s, we have

$$\begin{aligned} \mathrm{M}_t &= \mathrm{M}_{t,B} + \frac{\alpha_s}{\pi}\mathrm{M}_{t,V} + \mathcal{O}(\alpha_s^2), \\ \mathrm{M_{OC}} &= \mathrm{M}_{\mathrm{OC}}^{(0)} + \frac{\alpha_s}{\pi}\mathrm{M}_{\mathrm{OC}}^{(1)} + \mathcal{O}(\alpha_s^2), \end{aligned} \tag{5.38}$$

with

$$\begin{aligned} \mathrm{M}_{\mathrm{OC}}^{(0)} &= \mathcal{B}_t^{(0)} G^{(0)}(\vec{0}; E), \\ \mathrm{M}_{\mathrm{OC}}^{(1)} &= \mathcal{B}_t^{(1)} G^{(0)}(\vec{0}; E) + \mathcal{B}_t^{(0)} G^{(1)}(\vec{0}; E). \end{aligned} \tag{5.39}$$

Inserting into the matched amplitude, we obtain

$$\mathrm{M}_t^{\mathrm{match}} = \Big[\mathcal{B}_t\, G(\vec{0}; \mathcal{E}) + (\mathrm{M}_{t,B} - \mathrm{M}_{\mathrm{OC}}^{(0)})\Big] + \frac{\alpha_s}{\pi}\Big[\mathrm{M}_{t,V} - \mathrm{M}_{\mathrm{OC}}^{(1)}\Big] + \mathcal{O}(\alpha_s^2). \tag{5.40}$$

The NLO-matched cross-section is obtained by squaring the matched amplitude and adding the corresponding real-radiation. Upon squaring the matched amplitude we obtain,

$$\begin{aligned} |\mathrm{M}_t^{\mathrm{match}}|^2 = &\Big|\mathcal{B}_t\, G(\vec{0}; \mathcal{E}) + (\mathrm{M}_{t,B} - \mathrm{M}_{\mathrm{OC}}^{(0)})\Big|^2 \\ &+ \frac{\alpha_s}{\pi}\ 2\mathrm{Re}\Big[\mathrm{M}_{t,B}^{\dagger}(M_{t,V} - \mathrm{M}_{\mathrm{OC}}^{(1)})\Big] \qquad (5.41) \\ &+ \frac{\alpha_s}{\pi}\ 2\mathrm{Re}\Big[(\mathcal{B}_t\, G(\vec{0}; \mathcal{E}) - \mathrm{M}_{\mathrm{OC}}^{(0)})^{\dagger}(\mathrm{M}_{t,V} - \mathrm{M}_{\mathrm{OC}}^{(1)})\Big] + \mathcal{O}(\alpha_s^2). \qquad (5.42) \end{aligned}$$

Expanding the $(\mathcal{B}_t\, G(\vec{0}; \mathcal{E}) - \mathrm{M}_{\mathrm{OC}}^{(0)})$ term, we note that the last line is formally of order α_s^2; i.e. beyond NLO accuracy. We do therefore not include it in our calculation. However, in the first line, we retrain the full $\mathcal{B}_t\, G(\vec{0}; \mathcal{E})$ term, which describes the threshold behavior. The fixed-order massless-quark contribution can be included by replacing the top-quark only amplitude M_t with the full amplitude and restoring overall factors extracted from the top-only amplitude.

5.3.3 Matched Cross-Section

We define our matched cross-section as follows:

$$\begin{aligned}
\sigma_{\text{LO}}^{\text{match}} &\equiv a_s^2(\mu_R) \int_{\tau_{min}}^1 \mathrm{d}\tau \frac{\mathrm{d}\mathcal{L}_{gg}(\mu_F)}{\mathrm{d}\tau} \mathcal{N}_{gg} \int \mathrm{d}\Phi_2 \left| \mathcal{M}_B + \mathbf{c} \left(\mathcal{B}(\mu)\, G(\vec{0}; \mathcal{E}, \mu) - \mathrm{M}_{\text{OC}}^{(0)} \right) \right|^2, \\
\sigma_{\text{NLO}}^{\text{match}} &\equiv \sigma_{\text{LO}}^{\text{match}} \\
&+ a_s^3(\mu_R) \int_{\tau_{min}}^1 \mathrm{d}\tau \frac{\mathrm{d}\mathcal{L}_{gg}(\mu_F)}{\mathrm{d}\tau} \mathcal{N}_{gg} \int \mathrm{d}\Phi_2\, 2\,\mathrm{Re} \left[\mathcal{M}_B^\dagger \left(\mathcal{M}_V(\mu_R) - \mathbf{c}\, \mathrm{M}_{\text{OC}}^{(1)}(\mu) \right) \right] \\
&+ a_s^3(\mu_R) \int_{\tau_{min}}^1 \mathrm{d}\tau \sum_{ij} \frac{\mathrm{d}\mathcal{L}_{ij}(\mu_F)}{\mathrm{d}\tau} \mathcal{N}_{ij} \int \mathrm{d}\Phi_3 \left| \mathcal{M}_{R,[ij]}(\mu_R) \right|^2 + \sigma_C\left(\mu_F, \mu_R\right),
\end{aligned} \tag{5.43}$$

where $\mathcal{N}_{ij}$ contains the flux factor and the average over spins and colors of the initial state partons of flavor i and j, e.g. $\mathcal{N}_{gg} = \frac{1}{2s}\frac{1}{64}\frac{1}{4}$, where we have introduced the luminosity factors $\mathcal{L}_{ij}$ defined as $\frac{\mathrm{d}\mathcal{L}_{ij}}{\mathrm{d}\tau} \equiv \int_\tau^1 \frac{\mathrm{d}x}{x} f_i(x, \mu_F)\, f_j(\frac{\tau}{x}, \mu_F)$, where $f_i(x, \mu_F)$ is the parton distribution function (PDF) of a parton with momentum fraction x and flavor i, and where μ_F is the factorization scale. The 2 and 3 particle phase-space integration measures are denoted by $\mathrm{d}\Phi_2$ and $\mathrm{d}\Phi_3$. The symbol $\mathbf{c} \equiv 32\pi\, \alpha_e\, Q_t^2\, T_R\, \delta^{a_1 a_2}$ collects constants which have been extracted in the definition of M_t. The real-radiation contributions with the factors of a_s extracted are denoted by $\mathcal{M}_{R,[ij]}$ and the collinear-subtraction counterterm is denoted by σ_C. We do not include resummation effects in the real-radiation because it is suppressed by a factor of β. The symbols $\mathrm{M}_{\text{OC}}^{(0)}$ and $\mathrm{M}_{\text{OC}}^{(1)}(\mu)$ denote the LO and NLO double-counted part of the amplitude as discussed above. Note that the explicit dependence of $\mathrm{M}_{\text{OC}}^{(1)}(\mu)$ on the scale μ stems from the renormalization of the Green's function $G(\vec{0}; E)$, while μ_R comes from the renormalization of UV divergences in $\mathcal{M}_V(\mu_R)$, and μ_F comes from initial-state collinear factorization.

For the numerical evaluation of Equation (5.43), we expand $\mathrm{M}_{\text{OC}}^{(0)}$ and $\mathrm{M}_{\text{OC}}^{(1)}$ to respectively $\mathcal{O}(\beta^3)$ and $\mathcal{O}(\beta^2)$ using the expressions stated in Section 5.3.1. At the two-loop order, the UV-renormalized and IR-subtracted fixed-order amplitude M_t has a Coulomb singularity, which is a logarithmic divergence in the limit $\beta \to 0$. This singularity is, however, subtracted by the expanded term M_{OC}, while a resummed (nonsingular) description of the Coulomb interactions is added back by the term $\mathcal{B}_t\, G(\vec{0}; \mathcal{E})$. For this purpose, we evaluate the Schrödinger Equation (5.27) numerically [264] to obtain $G(\vec{0}; \mathcal{E})$, where we include $\mathcal{O}(\alpha_s)$ corrections to the QCD potential [254, 255]. Unlike the calculation in [223], we also include $\mathcal{O}(\alpha_s)$ corrections to $\mathcal{B}_t$ as listed above.

5.4 Results

Our numerical results for the process $gg \to \gamma\gamma$ are calculated at a hadronic center-of-mass energy of 13 TeV, using the parton distribution functions `PDF4LHC15_nlo_100` [265–

268] interfaced via LHAPDF [269], along with the corresponding value for α_s. For the electromagnetic coupling, we use $\alpha = 1/137.035999139$. The mass of the top quark is fixed to $m_t = 173$ GeV. The top-quark width is set to zero in the fixed-order calculation and to $\Gamma_t = 1.498$ GeV in the numerical evaluation of the Green's function $G(\vec{0}; \mathcal{E})$ in accordance with [223]. We use the cuts $p_{T,\gamma_1}^{\min} = 40$ GeV, $p_{T,\gamma_2}^{\min} = 25$ GeV and $|\eta_\gamma| \leq 2.5$. No photon isolation cuts are applied.

The factorization and renormalization scale uncertainties are estimated by varying the scales μ_F and μ_R. Unless specified otherwise, the scale-variation bands represent the envelopes of a 7-point scale variation with $\mu_{R,F} = c_{R,F}\, m_{\gamma\gamma}/2$, where $c_R, c_F \in \{2, 1, 0.5\}$ and where the extreme variations $(c_R, c_F) = (2, 0.5)$ and $(c_R, c_F) = (0.5, 2)$ are omitted. The dependence on the scale μ introduced by renormalization of the Green's function $G(\vec{r}; \mathcal{E})$ in our NRQCD matched results is investigated separately.

5.4.1 Validation

We have validated the massless NLO cross-section by comparison to MCFM version 9.0 [270] and find agreement within the numerical uncertainties for all scale choices. We also compared against the results shown in [228] and find agreement for the central scale choice. We do, however, find a smaller scale-uncertainty band.

Besides the approach described in Section 5.2.1, the helicity amplitudes can also be computed by first performing the Lorentz-tensor decomposition using the form factor projectors given in [243] and then evaluating contractions between the corresponding Lorentz structures and external polarization vectors in 4 dimensions using the spinor-helicity representations. This amounts to obtaining helicity amplitudes defined in the t'Hooft-Veltman scheme [36]. We confirm numerically that the same finite remainders are obtained for all helicity configurations at a few chosen test points The unsubtracted helicity amplitudes do differ starting from the subleading power in ϵ.

As a further cross check, we evaluated our amplitude with $t \leftrightarrow u$ interchanged and confirm that the helicity amplitudes are permuted as expected.

Numerical values for the coefficients $\mathcal{A}^J_{t,\{\lambda_i\}}$ at leading-order in α_s up to $J = 4$ are given in [223]. We have used them as a check of our numerical calculation of the Born amplitude.

We also evaluated the massive two-loop amplitude at 615 phase-space points with $m_t = 173$ GeV in the ranges $0 < \cos(\theta) < 1$ and $0.001 \leq \beta \leq 0.2$, using the program pySecDec [161, 162]. The amplitude can numerically be fitted to a suitable ansatz in β and $\cos\theta$. We have compared the coefficients of terms proportional to $\ln(\beta)$ to the known analytical results based on expanding Equation (5.30) and find good agreement. Note that the coefficients of terms not proportional to $\ln(\beta)$ receive contributions from the unknown term $A^{(1)}(\theta)$ and can therefore not be checked this way.

5.4.2 Invariant-Mass Distribution of the Diphoton System

The distribution of the invariant mass of the photon pair is shown in Figure 5.3 for invariant masses up to 1 TeV, where we show purely fixed-order results at LO, at NLO

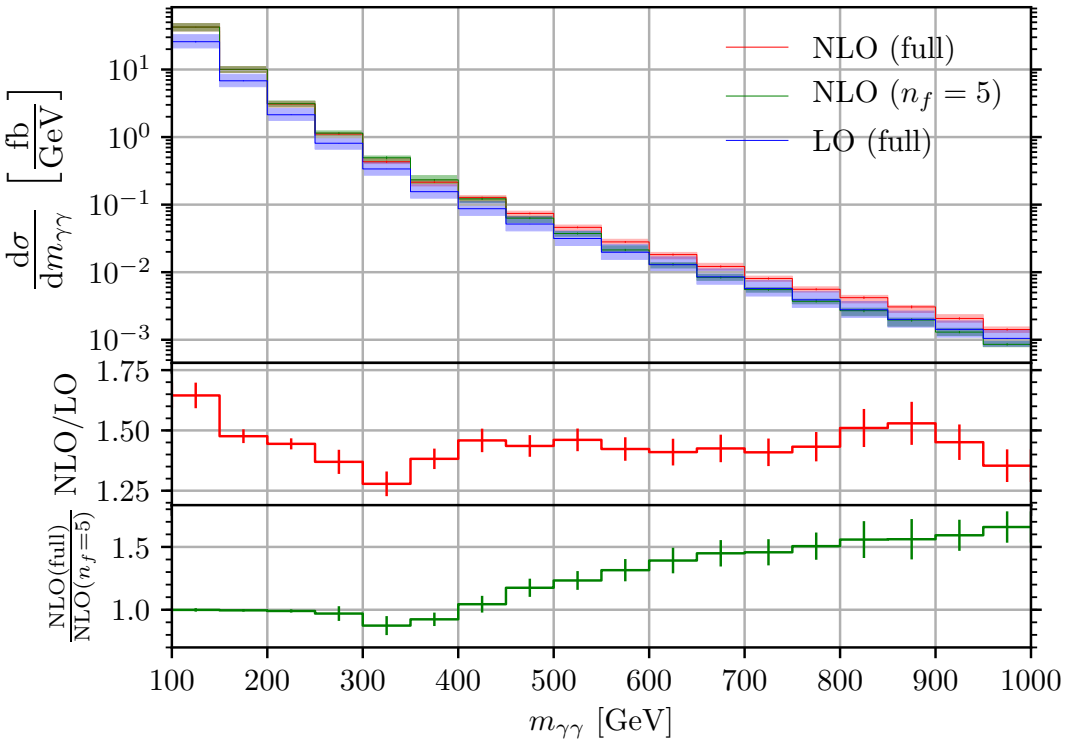

Figure 5.3: Diphoton invariant mass distribution (fixed order calculation), comparing the result with $n_f = 5$ to the result including massive top-quark loops. The shaded bands show the envelope of the 7-point scale variation as explained in the text. The lower panels shows the ratios NLO(full)/LO(full) and NLO(full)/NLO($n_f = 5$) evaluated at the central scale $\mu_R = \mu_F = m_{\gamma\gamma}/2$. The bars indicate the uncertainty due to the numerical evaluation of the phase-space and loop integrals.

with five massless flavors, and at NLO including massive top-quark loops. The ratio plots show the K-factor including the full quark-loop content and the ratio between the full and the five-flavor NLO cross-section. We observe that the scale uncertainties are reduced at NLO, and that the top-quark loops enhance the differential cross-section for $m_{\gamma\gamma}$ values far beyond the top-quark pair-production threshold, asymptotically approaching the $n_f = 6$ value [238].

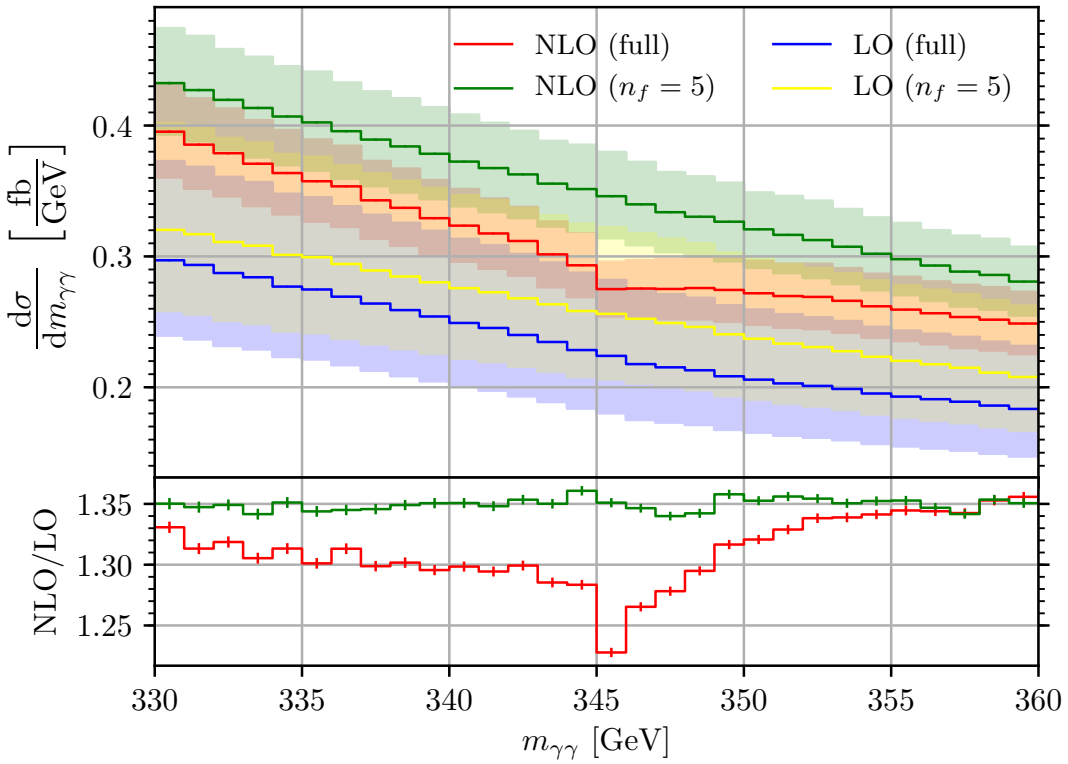

Figure 5.4: The threshold region of the diphoton invariant-mass distribution (fixed-order calculation), showing the $n_f = 5$ and the full result separately. The shaded bands indicate the scale uncertainties, while the bars indicate uncertainties due to the numerical evaluation of the phase-space and loop integrals. The ratio plot in the lower panel shows the ratios NLO(full)/LO(full) (red) and NLO($n_f = 5$)/LO($n_f = 5$) (green).

In Figure 5.4, we zoom into the threshold region, still showing fixed order results only. We can clearly see that after the top-quark pair-production threshold, the full result shows a dip and then changes slope, which is due to the fact that the two-loop amplitude contains the exchange of a Coulomb gluon (see top-left diagram of Figure 5.1) as explained in Section 5.3. In [223], it was suggested that this characteristic "dip-bump structure" could be used for a determination of the top-quark mass which is free of top-quark-reconstruction uncertainties, at least at the FCC where the statistical uncertainties for this process would be very small and the systematic uncertainty due

to the finite resolution of the photon energies and angles should be at least as good as at the LHC, where it is at the sub-percent level [271, 272].

In Figure 5.5, we show the $m_{\gamma\gamma}$ distribution in the threshold region, which results from a combination of the fixed-order NLO(QCD) calculation with the resummation of Coulomb-gluon exchanges as described in Section 5.2.5. The scale bands in this figure are produced by varying only μ, the scale associated to the renormalization of the Green's function. We observe that the dependence on the scale μ is considerably reduced at NLO compared to the leading-order matched cross-section. The scale band at NLO is comparable to the size of our numerical uncertainties. Further, our leading-order matched cross-section shows a milder dependence on μ than the one presented in [223]. This is due to the inclusion of NLO terms in the coefficient $\mathcal{B}_t(\beta)$, which have been omitted in [223].

We do not consider the effects from a color-octet $t\bar{t}$ state because the corresponding Green's function is monotonically increasing in the resonance region [262] and therefore not expected to move the position of the dip significantly.

Now let us address the prospects to measure the top-quark mass from the threshold behavior of the $m_{\gamma\gamma}$ distribution. In [223], it was argued that the characteristic dip-bump structure does not change its location in the $m_{\gamma\gamma}$ spectrum under scale variations, only the overall normalization is changing. It was also anticipated that the inclusion of the fixed-order two-loop amplitude would reduce this uncertainty. Indeed, we find that the NLO corrections reduce the scale uncertainties due to 7-point μ_R, μ_F-variations from about 20% at LO to just below the 10% level at NLO. However, the pronounced dip-bump structure present in the LO resummed calculation is partly washed out in the NLO NRQCD-improved calculation.

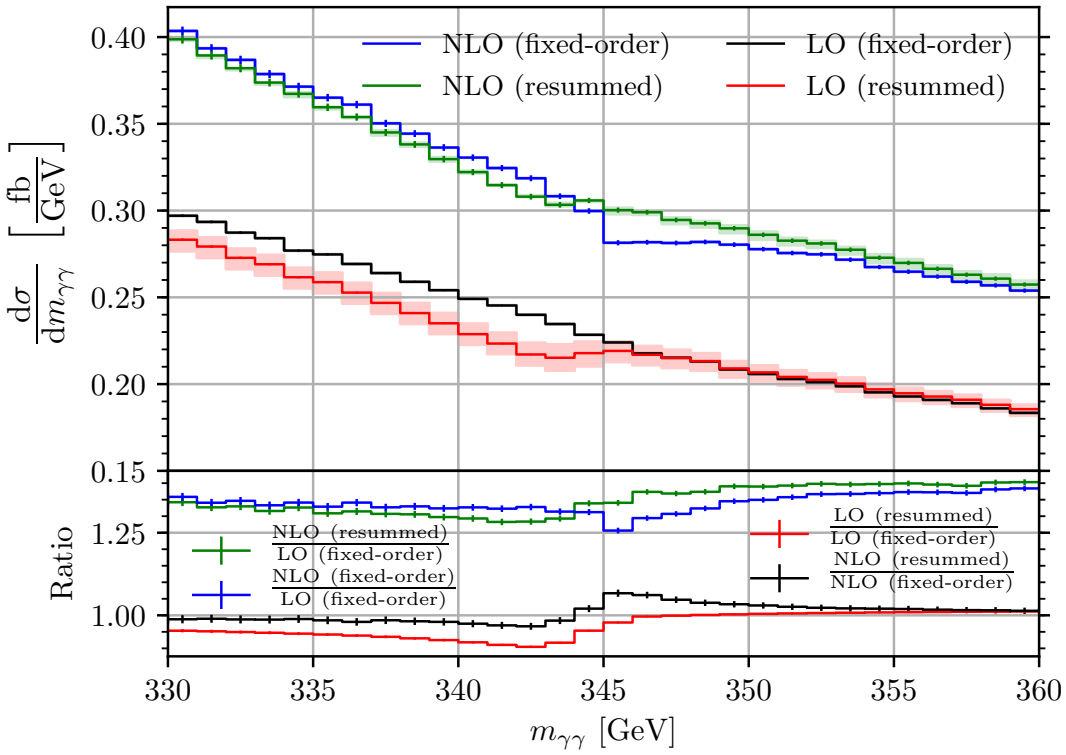

Figure 5.5: Zoom into the threshold region of the diphoton invariant mass distribution, comparing results with and without NRQCD. The shaded bands indicate the scale uncertainty by varying the scale μ by a factor of 2 around the central scale $\mu = 80$ GeV. The renormalization and the factorization scales are set to $\mu_R = \mu_F = m_{\gamma\gamma}/2$ and not varied in this plot. The bars indicate uncertainties due to the numerical evaluation of the phase-space and loop integrals.

6 Production of Two Z Bosons in Proton-Proton Collisions

Z-boson pair production is an important process to probe the electroweak sector of the Standard Model at the LHC, for example to assess anomalous gauge boson couplings. Direct Z-boson pair production is furthermore an important background to Higgs-boson production due to the electroweak Higgs-boson decays: In particular the interference of direct (without Higgs propagator) and indirect (via a virtual Higgs boson) production in gluon fusion gives a sizable negative contribution [273].

This Chapter is based on the publication [274], where we consider the hadronic process at NNLO-level in QCD excluding the massive top-quark contributions in the two-loop virtual corrections[1]. Unlike earlier calculations considering the same contributions [275, 276] which use the q_T-subtraction scheme [50], we apply the N-jettiness subtraction method [53, 55] for NNLO infrared subtractions. A subsequent publication where the effects of massive top-quark loops are included in our setup is planned for the near future. We did not yet succeed in getting the full integral reduction using publicly available tools. We have started a collaboration to obtain the reduction using the upcoming method of IBP reduction over finite fields and rational reconstruction [277–281].

The structure of this Chapter is as follows: We provide a summary of earlier calculations and a summary of contributing partonic subprocesses in Section 6.1. The form-factor decomposition of the amplitude is discussed in Section 6.2. Details about the infrared subtraction procedure are explained in Section 6.3. The results are presented in Section 6.4.

6.1 Overview

The perturbative orders of the subprocesses contributing to the inclusive hadronic ZZ production cross-section up to NNLO(QCD) accuracy are listed in Table 6.1. Sample Feynman diagrams are shown in Figure 6.1. Note that the gluon-fusion channel is loop induced and that its leading-order cross-section is suppressed by two powers of α_s compared to the leading order of the quark channel at partonic cross-section level. The partonic leading order of the gluon-fusion channel is therefore NNLO at hadron level while its partonic NLO correction is $\mathrm{N^3LO}$ at hadron level. We include only the hadronic NNLO contributions in our calculation; i.e. the partonic NLO contribution

[1]The corresponding two-loop integrals have currently only been calculated in expansions around certain kinematic limits but not in full generality. We list the available results in Section 6.1

of the gluon channel is *not* included. We do however find the gluon-fusion channel to give a sizable contribution as discussed in Section 6.4.2 such that including its NLO correction would be desirable in a subsequent publication.

subprocess	number of loops	powers of $g_S \propto \sqrt{\alpha_s}$ at matrix-element level	contributing order at cross-section level
$q\bar{q} \to ZZ$	0	0	LO
	1	2	NLO
	2	4	NNLO
$q\bar{q} \to ZZg$	0	1	NLO
	1	3	NNLO
$q\bar{q} \to ZZgg$	0	2	NNLO
$q\bar{q} \to ZZq\bar{q}$	0	2	NNLO
$gg \to ZZ$	1	2	NNLO
	2	4	N^3LO
$gg \to ZZg$	1	3	N^3LO

Table 6.1: Matrix elements and their perturbative orders contributing to the production cross-section of $pp \to ZZ + X$ up to NNLO in QCD. The contribution from the two-loop gluon-fusion channel which is formally N^3LO is also shown, but excluded from our calculation. Crossings of these matrix elements, e.g. $qg \to ZZqg$ or $qq \to ZZqq$, are not listed explicitly but contribute as well and are included in our calculation.

Recent measurements of Z-boson pair production at the LHC by ATLAS and CMS include [282–290]. The NLO QCD corrections to Z-boson pair production were calculated first for stable Z bosons in [291, 292] and later including leptonic decays in the narrow-width approximation [293]. Leptonic decays including spin correlations and off-shell effects have been taken into account in [117, 294]. The one-loop calculation for stable Z bosons in gluon fusion has been performed in [295, 296]. Leptonic decays, interference with Higgs boson production, and off-shell effects have been studied in [118, 297–303]. Associated production of two Z bosons with a jet was considered in [304]. Soft gluon resummation to the signal/background interference process $gg(\to H^{(*)}) \to ZZ$ was performed in [305]. Recently, the (massless) 2-loop amplitudes for $q\bar{q} \to VV'$ [306–309] and $gg \to VV'$ [310, 311] became available. They were used in the calculation of the NNLO corrections for Z-boson pair production, for on-shell Z bosons [275] later also including leptonic decays [276, 312]. The two-loop corrections to the gluon fusion channel were also calculated [273, 313] and combined with a parton shower [314]. Electroweak (EW) NLO corrections were calculated for stable vector bosons in [315–317]. Leptonic decays were included in [318]. NLO EW corrections including full off-shell effects have been computed in [319–321]. NLO QCD+EW corrections have been considered in [322] and were combined with an effective field theory framework in [323]. Very recently, partial N^3LO contributions from the quark-gluon fusion channel [324] and interference of four-lepton final states via ZZ and W^+W^- interference [312] have been studied. The effect of massive quark loops in the two-loop virtual amplitude (coming from diagrams like the one in the middle of the upper row in Figure 6.1c) has been estimated to

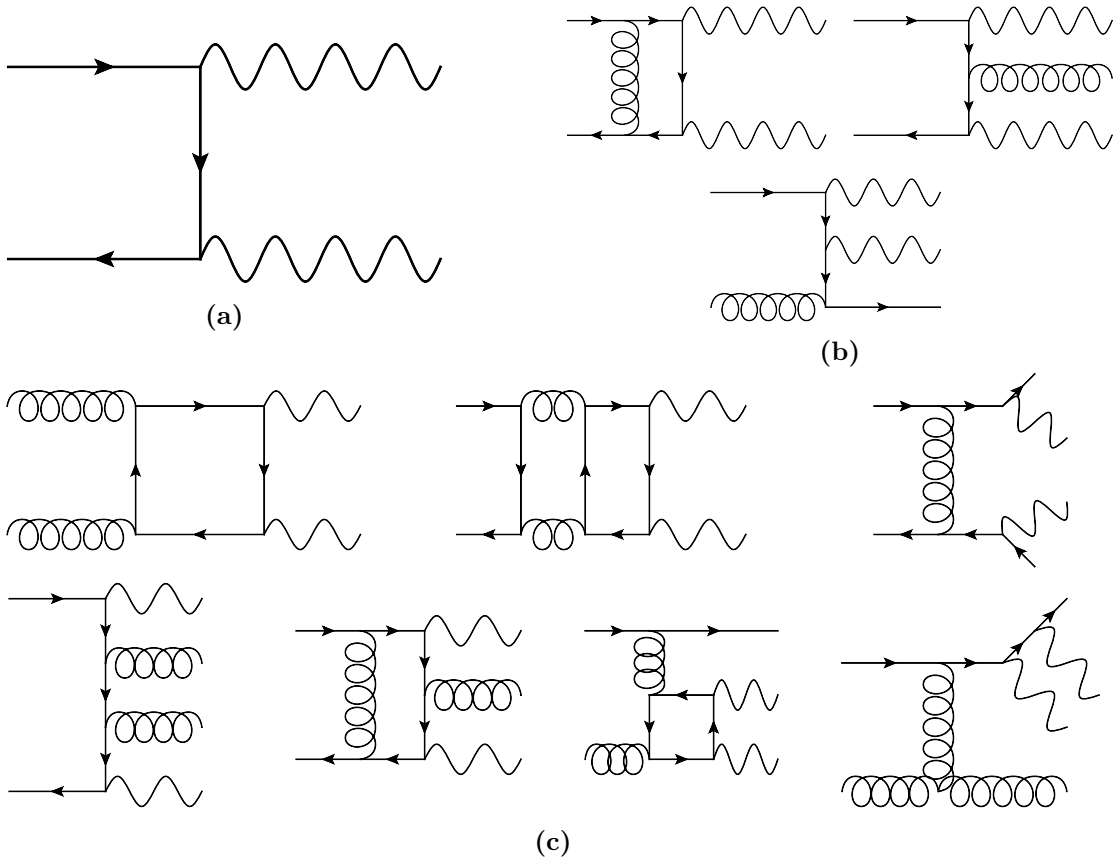

Figure 6.1: Diagrams contributing to the production cross-section of $pp \to ZZ + X$ at (a) leading order, (b) next-to-leading order, and (c) next-to-next-to leading order in QCD.

be a permille-level contribution to the total cross-section in [275]. Such contributions are currently only known in a heavy-top-quark expansion around $m_t \to \infty$ [325, 326] and an expansion around the top-quark pair-production threshold [327]. The tail of the invariant-mass distribution of the ZZ-system cannot be reliably predicted in this framework since the expansion breaks down at the top-quark-pair production threshold. In the high-invariant-mass region, however, the massive top loops become the dominant contribution to the interference of direct (without Higgs propagator) and indirect (via a virtual Higgs boson) production [273]. These calculations further indicate that the effect on the total cross-section may also be larger.

6.2 Form Factor Decomposition

The form-factor decompositions for the partonic subprocesses $q\bar{q} \to ZZ$ and $gg \to ZZ$ which are the only ones required at two-loop order (see Table 6.1), have been worked out in [309] and [310], respectively. Projection operators are also provided in ancillary files to these publications. We use these projectors for the two-loop calculations performed with our multi-loop amplitude generator described in Section 3.2. We have reproduced the vector-vector amplitude of `qqvvamp` [309] for di-Z production. We further confirm that, after renormalization and infrared subtraction, the helicity amplitudes of the axial-axial amplitude are indeed equal to the vector-vector amplitude and that the sum of the vector-axial and the axial-vector amplitudes is zero. In the following, we summarize the strategy of [309] to obtain the projection operators for the quark channel. The decomposition of the gluon channel is analogous and fully worked out in [310].

Considering all possible tensors and keeping only linear independent ones, the amplitude of the subprocess $q\bar{q} \to ZZ$ can be expressed as

$$\mathcal{Q}(p_1,p_2,p_3) = \bar{v}_i(p_2)\,\mathcal{Q}_{ij}^{\mu\nu}(p_1,p_2,p_3)\,u_j(p_1)\,\epsilon_\mu^*(p_3)\,\epsilon_\nu^*(p_4), \tag{6.1}$$

$$\begin{aligned}
\mathcal{Q}_{ij}^{\mu\nu}(p_1,p_2,p_3) \equiv\ & \mathcal{Q}_1\,p_1^\mu p_1^\nu\,[\not{p}_3]_{ij} + \mathcal{Q}_2\,p_1^\mu p_2^\nu\,[\not{p}_3]_{ij} + \mathcal{Q}_3\,p_1^\mu p_3^\nu\,[\not{p}_3]_{ij} \\
& + \mathcal{Q}_4\,p_2^\mu p_1^\nu\,[\not{p}_3]_{ij} + \mathcal{Q}_5\,p_2^\mu p_2^\nu\,[\not{p}_3]_{ij} + \mathcal{Q}_6\,p_2^\mu p_3^\nu\,[\not{p}_3]_{ij} \\
& + \mathcal{Q}_7\,p_3^\mu p_1^\nu\,[\not{p}_3]_{ij} + \mathcal{Q}_8\,p_3^\mu p_2^\nu\,[\not{p}_3]_{ij} + \mathcal{Q}_9\,p_3^\mu p_3^\nu\,[\not{p}_3]_{ij} \\
& + \mathcal{Q}_{10}\,p_1^\nu\,[\gamma^\mu]_{ij} + \mathcal{Q}_{11}\,p_2^\nu\,[\gamma^\mu]_{ij} + \mathcal{Q}_{12}\,p_3^\nu\,[\gamma^\mu]_{ij} \\
& + \mathcal{Q}_{13}\,p_1^\mu\,[\gamma^\nu]_{ij} + \mathcal{Q}_{14}\,p_2^\mu\,[\gamma^\nu]_{ij} + \mathcal{Q}_{15}\,p_3^\mu\,[\gamma^\nu]_{ij} \\
& + \mathcal{Q}_{16}\,[\gamma^\mu \not{p}_3 \gamma^\nu]_{ij} + \mathcal{Q}_{17}\,[\gamma^\nu \not{p}_3 \gamma^\mu]_{ij},
\end{aligned} \tag{6.2}$$

where p_1 and p_2 are the momenta of the incoming quark and antiquark, p_3 and $p_4 = p_1 + p_2 - p_3$ are the momenta of the outgoing Z bosons, and the $\mathcal{Q}_k$ are scalar *form factors*. Some form factors do not contribute to any physical observable due to transversality of the polarization vectors which is valid in Landau gauge,

$$p_3^\mu \epsilon_\mu(p_3) = p_4^\mu \epsilon_\mu(p_4) = 0. \tag{6.3}$$

The ten relevant tensor structures are [309] (see also [328, 329])

$$\begin{aligned}
T_1{}_{ij}^{\mu\nu} &= p_1^\mu p_1^\nu \,[\not{p}_3]_{ij}, & T_2{}_{ij}^{\mu\nu} &= p_1^\mu p_2^\nu \,[\not{p}_3]_{ij},\\
T_3{}_{ij}^{\mu\nu} &= p_2^\mu p_1^\nu \,[\not{p}_3]_{ij}, & T_4{}_{ij}^{\mu\nu} &= p_2^\mu p_2^\nu \,[\not{p}_3]_{ij},\\
T_5{}_{ij}^{\mu\nu} &= p_1^\nu \,[\gamma^\mu]_{ij}, & T_6{}_{ij}^{\mu\nu} &= p_2^\nu \,[\gamma^\mu]_{ij},\\
T_7{}_{ij}^{\mu\nu} &= p_1^\mu \,[\gamma^\nu]_{ij}, & T_8{}_{ij}^{\mu\nu} &= p_2^\mu \,[\gamma^\nu]_{ij},\\
T_9{}_{ij}^{\mu\nu} &= [\gamma^\mu \not{p}_3 \gamma^\nu]_{ij}, & T_{10}{}_{ij}^{\mu\nu} &= [\gamma^\nu \not{p}_3 \gamma^\mu]_{ij}.
\end{aligned} \tag{6.4}$$

This allows us to write the amputated amplitude as

$$\mathcal{Q}_{ij}^{\mu\nu} = \sum_{k=1}^{10} \mathcal{Q}'_k T_k{}_{ij}^{\mu\nu} + \mathrm{I}_{ij}^{\mu\nu}, \tag{6.5}$$

where the $\mathcal{Q}'_k$ correspond to a renumbered subset of the form factors $\mathcal{Q}$ and $\mathrm{I}_{ij}^{\mu\nu}$ is a tensor which vanished when contracted with a physical polarization vector in Landau gauge,

$$\epsilon_\mu(p_3)\,\mathrm{I}_{ij}^{\mu\nu} = \epsilon_\nu(p_4)\,\mathrm{I}_{ij}^{\mu\nu} = 0. \tag{6.6}$$

It is important to keep in mind that even though the tensor $\mathrm{I}_{ij}^{\mu\nu}$ does not contribute to physical observables, it is in general present. It can in particular pollute the extracted form factors if not properly taken care of by the projection operators.

The tensor $\mathrm{I}_{ij}^{\mu\nu}$ can be removed by application of polarization sums,

$$\left[\sum_{\text{pol.}} \epsilon_\mu(p_3)\epsilon_\rho^*(p_3)\right]\left[\sum_{\text{pol.}} \epsilon_\nu(p_4)\epsilon_\sigma^*(p_4)\right] \mathcal{Q}_{ij}^{\rho\sigma}, \tag{6.7}$$

where

$$\sum_{\text{pol.}} \epsilon_\mu(p_k)\epsilon_\nu^*(p_k) = -g^{\mu\nu} + \frac{p_k^\mu p_k^\nu}{p_k^2}. \tag{6.8}$$

Projection operators to extract the relevant form factors $\mathcal{Q}'_k$ from the amplitude can be constructed using the tensors in (6.4), the polarization sums for the incoming massless (anti-)fermion,

$$\sum_{\text{pol.}} u_i(p_1)\,\bar{u}_j(p_1) = [\not{p}_1]_{ij}, \quad \sum_{\text{pol.}} v_i(p_2)\,\bar{v}_j(p_2) = [\not{p}_2]_{ij}, \tag{6.9}$$

and the polarization sums for the Z bosons (6.8). The projection operators are given by

$$\begin{aligned}
\mathcal{P}_k{}_{ji}^{\mu\nu} \equiv &\left[\sum_{\text{pol.}} u_m(p_1)\,\bar{u}_j(p_1)\right]\left[\sum_{\text{pol.}} v_i(p_2)\,\bar{v}_n(p_2)\right]\\
&\left[\sum_{\text{pol.}} \epsilon_\mu(p_3)\epsilon_\rho^*(p_3)\right]\left[\sum_{\text{pol.}} \epsilon_\nu(p_4)\epsilon_\sigma^*(p_4)\right]\sum_{l=1}^{10} c_{kl}\, T_l{}_{nm}^{\rho\sigma}
\end{aligned} \tag{6.10}$$

where the coefficients c_{kl} are obtained by solving the system of equations

$$\mathcal{P}_{k\,ji}^{\mu\nu}\, T_{l\,\mu\nu}^{ij} \stackrel{!}{=} \delta_{kl}. \tag{6.11}$$

6.3 Infrared Subtraction with N-Jettiness Variables

We employ the N-jettiness subtraction scheme [52–55] to perform the evaluation of the NNLO cross-section. The definition of the N-jettiness variable reads [56, 57]

$$\tau_N \equiv \frac{2}{Q^2} \sum_k \min\left\{q_a \cdot p_k, q_b \cdot p_k, q_1 \cdot p_k, \ldots, q_N \cdot p_k\right\}, \tag{6.12}$$

where N denotes the number of jets desired in the final state and the sum runs over all QCD radiated particles, $q_a, q_b, q_1, \ldots, q_N$ are a fixed set of massless reference momenta for the two beam jets and the N observed jets, the p_k are the momenta of the external partons, and the dimensionful parameter Q^2 is a hard interaction scale. For the specific case of a colorless diboson system without additional partons in the final state, Equation (6.12) reduces to the 0-jettiness or beam thrust which in the leptonic frame reads [56, 330]

$$\mathcal{T}_0 \equiv Q\,\tau_0 = \sum_k \min\left\{e^{Y_{ZZ}} n_a \cdot p_k, e^{-Y_{ZZ}} n_b \cdot p_k\right\}, \tag{6.13}$$

where $n_a = (1,0,0,1)$ and $n_b = (1,0,0,-1)$ define the beam axis and the p_k are defined in the hadronic center-of-mass frame. In the context of N-jettiness subtractions, defining the N-jettiness variable in the leptonic reference frame (by taking the boost with rapidity Y_{ZZ} into account) ensures that the power corrections are independent of Y_{ZZ} [330].

Looking at the definition of 0-jettiness in (6.13), we observe that $\mathcal{T}_0$ approaches zero in the limit where the QCD emission p_k is soft or collinear to an initial state. For this reason, values of $\mathcal{T}_0$ close to zero indicate a final state containing the Z-boson pair and only IR (soft and collinear) parton emissions. The N-jettiness variable can therefore be used as a slicing parameter in any real-radiation phase space integral to separate infrared singular regions from hard and resolved ones. In that sense, the approach extends the slicing methods developed in the early 90's to compute higher-order corrections at NLO [49] to NNLO.

To separate singular and nonsingular regions, we split the single- and double-real radiation phase-space of the NNLO cross-section into contributions with the 0-jettiness below $\Delta\sigma_{NNLO}^{<}$ and above $\Delta\sigma_{NNLO}^{>}$ the parameter $\mathcal{T}_0^{cut}$ [53–55]

$$\sigma_{NNLO} \equiv \sigma_{NLO} + \Delta\sigma_{NNLO}^{<} + \Delta\sigma_{NNLO}^{>}, \tag{6.14}$$

where

$$\begin{aligned}\Delta\sigma^{<}_{NNLO} \equiv & \int \mathrm{d}\Phi_N \, |\mathcal{M}_{VV}|^2 \\ & + \int \mathrm{d}\Phi_{N+1} \, |\mathcal{M}_{RV}|^2 \, \theta(\mathcal{T}_0^{cut} - \mathcal{T}_0) + \int \mathrm{d}\Phi_{N+2} \, |\mathcal{M}_{RR}|^2 \, \theta(\mathcal{T}_0^{cut} - \mathcal{T}_0), \quad (6.15) \\ \Delta\sigma^{>}_{NNLO} \equiv & \int \mathrm{d}\Phi_{N+1} \, |\mathcal{M}_{RV}|^2 \, \theta(\mathcal{T}_0 - \mathcal{T}_0^{cut}) + \int \mathrm{d}\Phi_{N+2} \, |\mathcal{M}_{RR}|^2 \, \theta(\mathcal{T}_0 - \mathcal{T}_0^{cut}),\end{aligned}$$

with the double-virtual matrix-element $\mathcal{M}_{VV}$ with Born-level kinematics, the real-virtual matrix-element $\mathcal{M}_{RV}$ with one additional parton in the final state, and the double-real matrix-element $\mathcal{M}_{RR}$ with two additional final-state partons. We have suppressed any (infrared-safe) measurement function under the phase space integral in Equation (6.15). The contributions below and above the slicing parameter $\mathcal{T}_0^{cut}$ are individually finite in $D = 4$ spacetime dimensions. Contributions with Born-level kinematics necessarily have $\mathcal{T}_0 = 0$. Contributions with $\mathcal{T}_0 > \mathcal{T}_0^{cut}$ necessarily contain one or more well separated hadronic energy deposits and thus reproduce the ZZ+jet cross-section at NLO. The contributions with $\mathcal{T}_0 < \mathcal{T}_0^{cut}$ correspond to the limit of the ZZ+jet NLO cross-section where the jet is unresolved. The key advantage that allows the computation of the cross-section at NNLO below $\mathcal{T}_0^{cut}$ is the fact that in the limit where all QCD emission is soft or collinear, the cross-section can be approximately computed using the machinery of Soft-Collinear Effective Theory (SCET) [331–334]. In particular, the existence of a factorization theorem that gives an all-order description of N-jettiness for $\mathcal{T}_N$ less than some (small) value $\mathcal{T}_N^{cut}$ allows the cross-section to be schematically written in the form [53]

$$\sigma(\mathcal{T}_N < \mathcal{T}_N^{cut}) = \int H \otimes B \otimes B \otimes S \otimes \left[\prod_n^N J_n\right] + \cdots, \quad (6.16)$$

where H describes the effect of hard radiation from the purely virtual corrections to the process, B encodes the effect of radiation collinear to one of the two initial beam directions, S describes soft radiation and J_n contains the radiation collinear to hard final-state jets, and the ellipsis denotes terms which are power-suppressed for $\mathcal{T}_N \ll Q$.

As can be seen from Table 6.1, an NNLO infrared subtraction scheme is only required for the quark channel $q\bar{q} \to ZZ$ when computing the ZZ production cross-section to order NNLO(QCD). We have expanded formula (6.16) to second order in the strong coupling constant α_s to obtain the contribution $\Delta\sigma^{<}_{NNLO}$. This particularly includes contributions from the universal quark beam function at two loops [335], the 0-jettiness soft function at two-loops [336, 337], and the process dependent hard function which has been extracted from the two-loop amplitude computed in [309] via an interface to the program `qqvvamp`. We refer the reader to Reference [274] for a description of the procedure.

The $\Delta\sigma^{>}_{NNLO}$ contribution corresponds to an NLO calculation of the process ZZ+jet. It is obtained using the tree-level matrix elements from VBFNLO [115, 338] for the double-real emission phase space integral which we cross-checked with `MadGraph5` [100],

and the one-loop amplitudes for the real-virtual phase space generated with GoSam (see Section 3.1) which we cross-checked against OpenLoops [111]. The one-loop amplitudes were computed using Ninja, which calls OneLOop for the master integrals, and rescued using an implementation of Ninja in quadruple precision for unstable phase space points. We also include the loop-induced one-loop squared corrections in the $gg \to ZZ$ channel, which are formally of NNLO accuracy, keeping full dependence on the top-quark mass and on the Higgs mediated contributions using GoSam.

6.4 Results

We compute the inclusive production of two on-shell Z bosons in proton-proton collisions at a center-of-mass energy $\sqrt{s} = 13$ TeV. We use the MSTW2008 [339] and NNPDF-3.0 [268] sets of parton distribution functions via the LHAPDF [269] interface. The parton densities and α_s are evaluated with $N_f = 5$ massless quark flavors at each corresponding order; i.e. we use $(n+1)$-loop α_s at $\mathrm{N}^n\mathrm{LO}$, with $n = 0, 1, 2$. Remember that we do not include massive top-quark loops in the virtual two-loop contribution to the subprocess $q\bar{q} \to ZZ$. Using $N_f = 5$ flavors therefore introduces the chiral anomaly stemming from subdiagrams where one Z boson and two gluons are attached to a b-quark triangle. However, we neglect this anomalous contribution in our calculation as the anomaly must cancel once the top-quark loops are included, following the same strategy as advocated in [313]. The default renormalization (μ_R) and factorization (μ_F) scales are set to $\mu_R = \mu_F = m_Z$. We use the G_μ EW scheme where the EW input parameters have been set to $G_F = 1.16639 \times 10^{-5}$, $m_W = 80.399$ GeV and $m_Z = 91.1876$ GeV. The top quark and Higgs boson masses that are included in the RV one-loop contributions and in the loop-induced gg channel have been set to $m_t = 173.2$ GeV and $m_H = 125$ GeV, respectively.

6.4.1 Dependence of the NNLO Corrections on the N-jettiness Cut

In Figure 6.2, we present the NNLO contributions of the ZZ cross-section as a function of $\mathcal{T}_0^{cut}$. We observe that the phase space integrals for the contributions $\Delta\sigma^{<}_{NNLO}$ and $\Delta\sigma^{>}_{NNLO}$ are logarithmically divergent to the fourth power in $\log\left(\mathcal{T}_0^{cut}\right)$, and for typical values of $\mathcal{T}_0^{cut}$ in the range $10^{-2} - 10^{-3}$ GeV need to be known with better than permille-level accuracy to achieve an accurate determination of the NNLO contribution.

In order to study the independence of the NNLO contribution on the choice of slicing parameter $\mathcal{T}_0^{cut}$ in more detail, we present the sum of the NNLO contributions

$$\Delta\sigma_{NNLO} \equiv \Delta\sigma^{<}_{NNLO} + \Delta\sigma^{>}_{NNLO}$$

in Figure 6.3. Within the errors, we observe a plateau in the region $\mathcal{T}_0^{cut} = 10^{-1} \sim 10^{-3}$ GeV; i.e. the sum tends to a constant in that region. In addition, we observe the on-set of the power corrections (which we do not compute) to the N-jettiness SCET factorization theorem for larger values of $\mathcal{T}_0^{cut}$ ($\mathcal{T}_0^{cut} > 10^{-1}$ GeV). The fact that the on-set of power corrections shows up for fairly large values of $\mathcal{T}_0^{cut}$ with respect to other

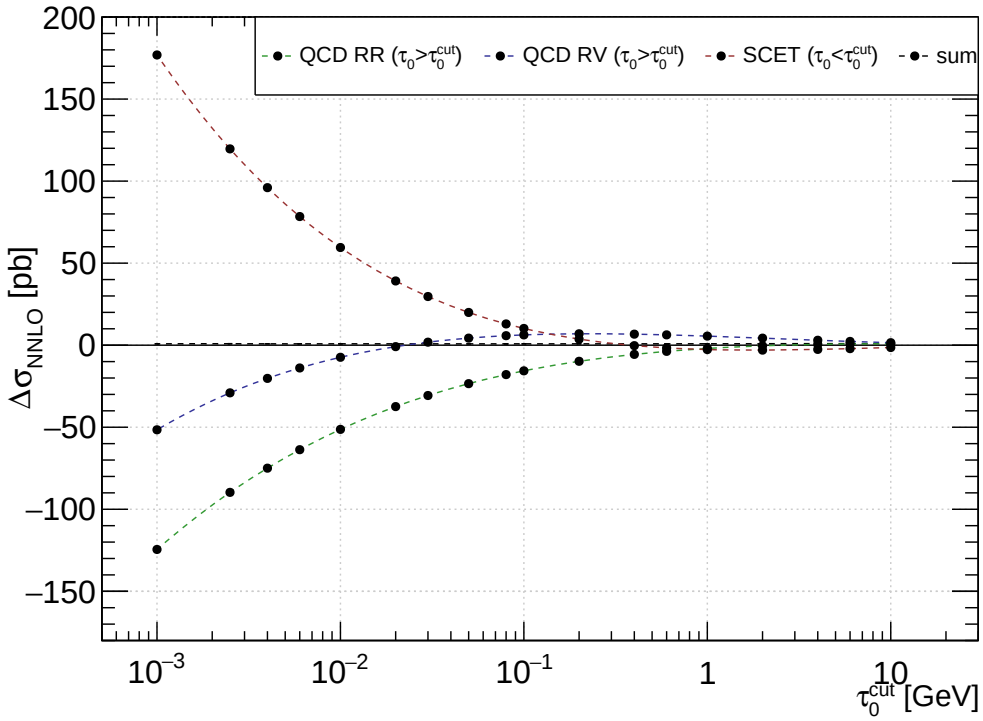

Figure 6.2: The NNLO contributions to the inclusive ZZ production cross-section computed with N-jettiness subtraction as a function of $\mathcal{T}_0^{cut}$. We show the cross-sections for $\Delta\sigma^{>}_{NNLO}$ from the double-real (dashed green) and real-virtual (dashed blue) phase space integrals and for $\Delta\sigma^{<}_{NNLO}$ from the SCET phase space integrals. Their sum is shown as the black dashed line.

processes [53, 54, 340] seems to indicate that for ZZ production their contribution is small. Nonetheless the leading power correction can be modeled after integration over the final-state phase space as [330, 341, 342]

$$\Delta\sigma^{NNLO}_{jettiness}(\mathcal{T}_0^{cut}) = \Delta\sigma^{NNLO} + c_3\,\frac{\mathcal{T}_0^{cut}}{Q}\,\log^3\left(\frac{\mathcal{T}_0^{cut}}{Q}\right) + c_2\,\frac{\mathcal{T}_0^{cut}}{Q}\,\log^2\left(\frac{\mathcal{T}_0^{cut}}{Q}\right) + ..., \quad (6.17)$$

where Q is an appropriate hard scale of the process and c_2, c_3 are unknown constants. We have performed a fit of the results of our Monte-Carlo runs to this functional form of the N-jettiness NNLO contribution and show the resulting fit as a black dotted line in Figure 6.3. The fit allows us to numerically extract the value of the NNLO contribution in the limit where $\mathcal{T}_0 \to 0$. This value can be compared to the reconstructed NNLO contribution for ZZ production obtained in [275][2], which is shown as a red line. We

[2]The NNLO contribution was reconstructed by subtracting the NLO ZZ cross-section and the contribution from the loop-induced gg-channel from the total NNLO ZZ cross-section quoted in Table 1 of [275].

use the extrapolated value for our result for the ZZ cross-section at NNLO shown in Table 6.2, which is in excellent agreement with the result $\sigma_{NNLO} = 16.91\,\text{pb}$ obtained in [275]. Due to the observed mild power corrections in this process, we do however choose to fix the value of the 0-jettiness slicing parameter to $\mathcal{T}_0^{cut} = 10^{-2}$ GeV for the histograms shown in Figure 6.5.

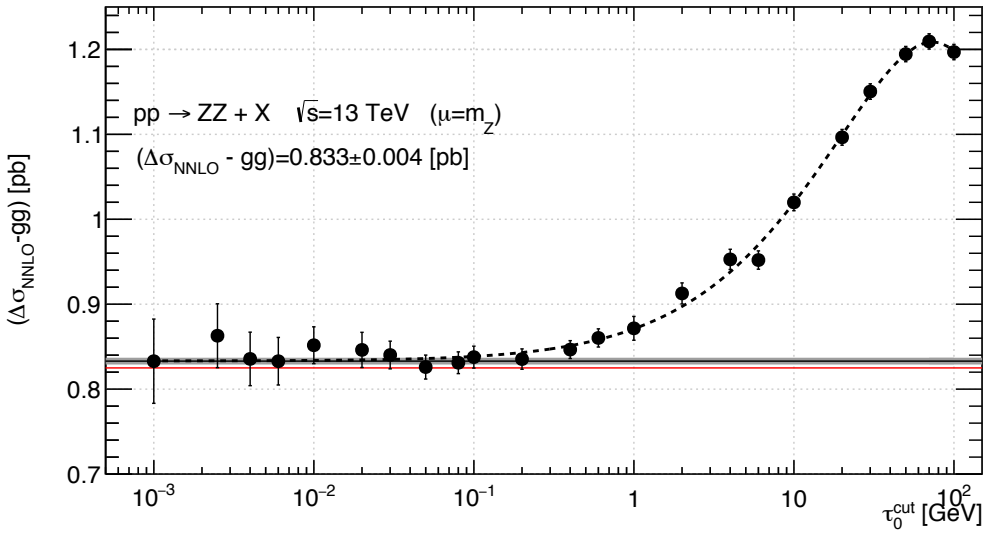

Figure 6.3: $\mathcal{T}_0^{cut}$ dependence of the NNLO contribution for ZZ production with the $\mathcal{T}_0^{cut}$ independent $gg \to ZZ$ contribution subtracted. The black dashed line shows the fit of the $\mathcal{T}_0^{cut}$ dependence of the NNLO contribution (black data points) to the analytic form in Equation (6.17). The $\mathcal{T}_0^{cut} \to 0$ limit is shown as a solid black line with a gray band showing the uncertainty on the fitted parameter. The red line represents the NNLO contribution reconstructed from the NNLO result obtained in [275].

As a consistency check we have also fitted a constant to the plateau region ($\mathcal{T}_0^{cut} < 10^{-2}$ GeV or $\mathcal{T}_0^{cut} < 10^{-1}$ GeV) and these fits yield compatible results for $\Delta\sigma^{NNLO}$. We have also fitted the leading power corrections using (6.17) including only results for $\mathcal{T}_0^{cut} < 1$ GeV. When fitting the leading power corrections with $\mathcal{T}_0^{cut} < 1$ GeV there is a strong correlation between c_3 and Q as well as c_2 and Q; fixing Q to values in the range $50 - 5000$ GeV we obtain compatible results for $\Delta\sigma^{NNLO}$. Including in the fit results up to $\mathcal{T}_0^{cut} < 10^2$ GeV as shown in Figure 6.3, we obtain a stable fit also when Q is treated as a free parameter.

6.4.2 Phenomenology

We compare our theoretical prediction with the ATLAS and CMS measurements at $\sqrt{s} = 13$ TeV [287, 288] in Table 6.2. In the same table, we also present an updated value

for the NNLO cross-section computed as described in the previous section but using the more recently determined NNPDF-3.0 [268] PDF sets and an updated value for the W-boson mass of $M_W = 80.385$ GeV; these settings are also used for our phenomenological results presented in the reminder of this section. We observe a significant improvement in the agreement with the data after the inclusion of the NNLO corrections.

In order to study the scale uncertainty of the cross-section in more detail, we present the renormalization and factorization scale dependence of the ZZ cross-section at LO, NLO, and NNLO in Figure 6.4. The scale uncertainty bands are largely non-overlapping which demonstrate that they are insufficient to estimate the missing higher order terms in the perturbative expansion for this process. This is however not unexpected since ZZ production at the LHC is an electroweak process which exhibits no renormalization scale dependence at LO. For this reason we obtain large NLO(QCD) corrections to the cross-section which are outside the LO scale band. Moreover, when going from NLO to NNLO, the loop-induced gluon fusion channel $gg \to ZZ$ opens up and due to the large gluon flux it represents a numerically significant contribution. Since this new channel contributes for the first time at NNLO its contribution cannot be captured by the scale variation of the NLO cross-section. Therefore, when increasing the perturbative order, we observe a systematic reduction of the factorization scale dependence of the cross-section (indicated by the thickness of the scale uncertainty band), while there is no significant reduction of the renormalization scale dependence. To show that this effect can be attributed to the gluon fusion channel opening up at NNLO, we also show the NNLO result excluding this channel.

The importance of new channels opening up at NNLO in the various kinematic regions can be studied by considering differential distributions. In Figure 6.5, we present the invariant mass of the ZZ-system and the average transverse momentum distribution $\langle \mathrm{p_{T,Z}} \rangle$ defined as $\langle \mathrm{p_{T,Z}} \rangle = (|p_T^{Z_1}| + |p_T^{Z_2}|)/2$. We present results for LO, NLO, NLO plus the loop-induced $gg \to ZZ$ channel, and NNLO. Figure 6.5a shows the ZZ invariant-mass distribution. In the first and second sub-panels, we show the effect of the NLO and NNLO corrections, respectively. We observe, in the first sub-panel, large NLO(QCD) corrections which vary between 40% at low m_{ZZ} and 60% at high m_{ZZ}, and change both the shape and the normalization of the predicted cross-section with respect to the LO result. Going to NNLO, we observe an approximately flat increase of the cross-section of about 18% with respect to the NLO result, where approximately 60% of this effect comes from the loop-induced $gg \to ZZ$ channel. The NNLO prediction is outside the scale uncertainty band of the NLO prediction. Similarly, in the transverse momentum distribution shown in Figure 6.5b, we observe large NLO corrections of approximately 30% at low $\langle \mathrm{p_{T,Z}} \rangle$, which can reach almost 100% at high $\langle \mathrm{p_{T,Z}} \rangle$. The shape of the NNLO corrections shown in the second sub-panel largely follows the contribution of the loop-induced $gg \to ZZ$ channel at low $\langle \mathrm{p_{T,Z}} \rangle$, and we observe a 30% effect at low $\langle \mathrm{p_{T,Z}} \rangle$ which decreases to about 18% at high $\langle \mathrm{p_{T,Z}} \rangle$. For both distributions we observe good convergence of the perturbative expansion, however the scale uncertainty bands do not overlap between the orders in the perturbative expansion that we have computed.

	σ_{LO} [pb]	σ_{NLO} [pb]	σ_{NNLO} [pb]
Our Result			
MSTW2008	$9.890^{+4.9\%}_{-6.1\%}$	$14.508^{+3.0\%}_{-2.4\%}$	$16.92^{+3.2\%}_{-2.6\%}$
NNPDF3.0	$9.845^{+5.2\%}_{-6.2\%}$	$14.100^{+2.9\%}_{-2.4\%}$	$16.69^{+3.1\%}_{-2.8\%}$
ATLAS [287]	$17.3 \pm 0.6(\text{stat.}) \pm 0.5(\text{syst.}) \pm 0.6(\text{lumi.})$		
CMS [288]	$17.2 \pm 0.5(\text{stat.}) \pm 0.7(\text{syst.}) \pm 0.4(\text{theo.}) \pm 0.4(\text{lumi.})$		

Table 6.2: Inclusive cross-section for ZZ production at the LHC run II $\sqrt{s} = 13$ TeV at LO, NLO and NNLO with $\mu_R = \mu_F = m_Z$, together with the measurements from ATLAS [287] and CMS [288]. Uncertainties in the theory calculation at each order are obtained by varying the renormalization and factorization scales in the range $0.5m_Z < \mu_R, \mu_F < 2m_Z$ with the constraint $0.5 < \mu_F/\mu_R < 2$. Uncertainties in the experimental measurements denote absolute statistical, systematic and luminosity uncertainties.

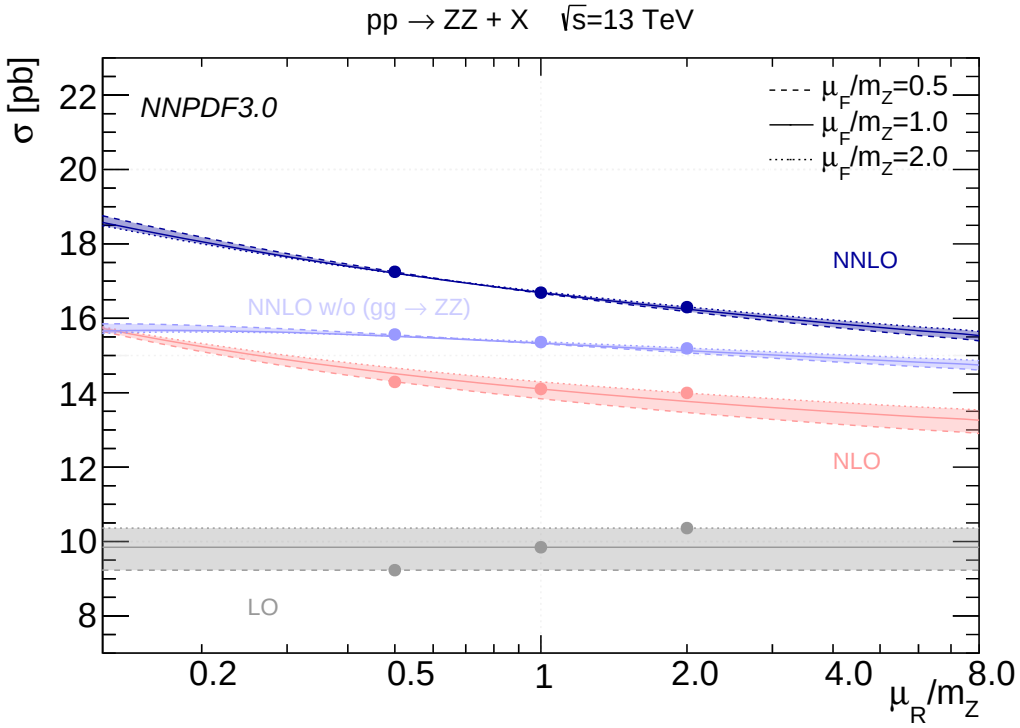

Figure 6.4: Renormalization and factorization scale dependence of the ZZ cross-section at LO, NLO, and NNLO for the central scale choice $\mu_R = \mu_F = m_Z$ and with NNPDF-3.0 PDFs. We also show the NNLO result without the gluon fusion contributions. The thickness of the bands shows the variation in the cross-section due to factorization scale while the slope shows the renormalization scale dependence.

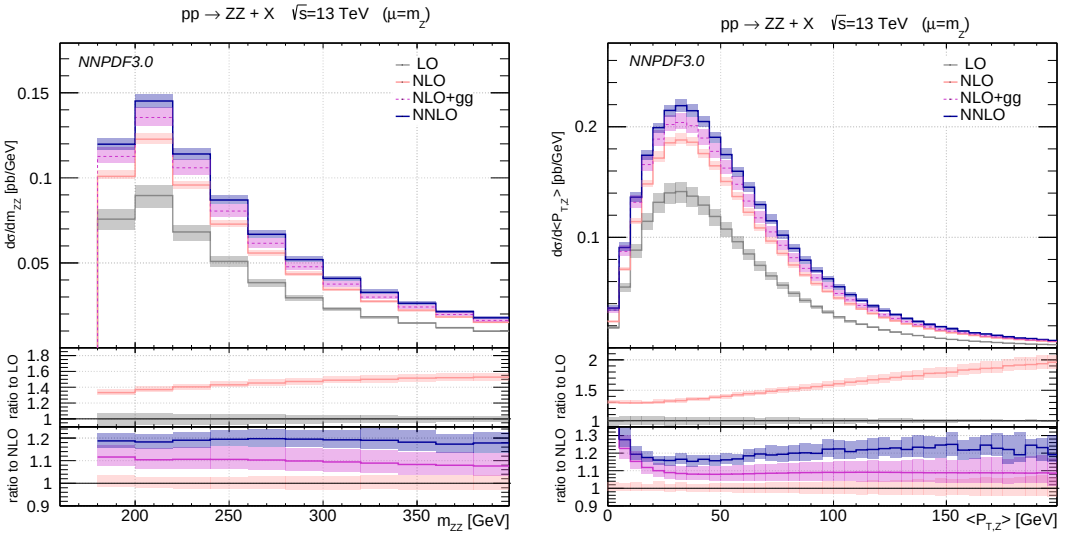

Figure 6.5: (a) ZZ invariant mass distribution and (b) averaged transverse momentum distribution $\langle p_{T,Z} \rangle$ of the Z-bosons computed at LO, NLO and NNLO. In the two sub panels we show respectively the NLO/LO and NNLO/NLO K-factors to visualize the size of the higher order effects. The result for the contribution from the loop-induced $gg \to ZZ$ subset of the full NNLO correction is also shown separately. Shaded bands represent the theory uncertainty due to the variation of the factorization and renormalization scales.

These results show that the inclusion of NNLO effects in ZZ production at the LHC is essential to obtain a reliable theoretical description of this process. In view of the numerical importance of the gluon-fusion channel, it is desirable to add the two-loop diagrams, including massive top-quark loops, to this channel, which will be left for a subsequent publication.

Part IV

Conclusion & Outlook

7 Conclusion & Outlook

The observations made at the LHC are currently consistent with the Standard Model of particle physics such that it is important to have a profound knowledge of the Standard Model prediction to spot small deviations in an experiment. We have discussed higher-order calculations in perturbation theory, which is one way to improve the accuracy of a theory prediction.

An important ingredient to higher-order calculations are the virtual corrections, which involves the evaluation of Feynman diagrams leading to loop integrals. We have presented tools targeted to automated multi-loop amplitude calculations. Specifically, we have developed a multi-loop extension of the program GoSam, which uses QGRAF to generate all necessary Feynman diagrams, `FORM` to insert the Feynman rules, `Reduze` to perform the integral reduction to a basis of master integrals and pySecDec to evaluate the master integrals. To be precise, our program numerically calculates form factors of the amplitude using user-defined projection operators. We also have implemented an algorithm for the treatment of the Dirac matrix γ_5 in the virtual amplitude. An automated treatment of the renormalization and the infrared subtraction is left for future work.

One of the steps in the calculation of higher-order virtual amplitudes is the evaluation of a basis-set of loop integrals - the master integrals. For that purpose, we have developed the program pySecDec, the successor of SecDec-3. While SecDec-3 is targeted to provide an automated cross-check of analytical calculations, pySecDec is designed such that it can also easily be embedded into amplitude calculations to provide numerical solutions of the master integrals. We have improved the performance of pySecDec with an existing quasi-Monte Carlo integration method based on shifted rank-1 lattice rules and refined the method to be adaptive, which further increases its performance. Another performance boost is obtained when running the quasi-Monte Carlo integrator on Graphics Processing Units (GPUs).

We have applied the aforementioned tools to calculate higher-order corrections to phenomenologically relevant processes at the LHC. We have calculated the production of two photons at the LHC in the gluon-fusion channel at NLO(QCD). We further have combined the fixed-order calculation with a resummation of enhanced terms around the top-quark production threshold, where the fixed-order calculation becomes unreliable due to the appearance of a Coulomb singularity. The resummation gives rise to a dip-bump structure of the differential diphoton invariant-mass distribution which can be exploited for top-quark mass measurements. We have combined the resummation with the fixed-order NLO calculation and find that the characteristic dip-bump structure is washed out but the change in slope is nevertheless still clearly visible. A detailed assessment whether this behavior is pronounced enough for a top-quark mass measure-

ment once all channels contributing to this observable are included deserves further study.

We further have introduced a framework for the calculation of the production of two Z bosons at the LHC at NNLO(QCD) with full top-quark-mass dependence. The calculation of the two-loop virtual corrections mediated by top-quark loops could not be finished yet due to the difficult reduction and is left for future work. The corresponding two-loop integrals have currently only been calculated in expansions around certain kinematic limits but not in full generality. Unlike earlier calculations of this process at the same level which use the q_T-subtraction scheme, we have applied the N-jettiness subtraction method for NNLO infrared subtractions. We have found good agreement with earlier theory-predictions and with recent ATLAS and CMS measurements of the total cross-section. The NNLO corrections increase the NLO result by about 18%, where almost 60% of this increase stems from the loop-induced $gg \to ZZ$ channel. In view of the numerical importance of this channel, it is desirable to add the two-loop diagrams including massive top-quark loops to this channel in future work, even though it is a $\mathrm{N^3LO}$ correction.

We hope that the tools we have developed and the considered applications prove useful for further advances in particle physics.

Appendix

A GoSam-Xloop Usage

This Appendix illustrates the basic usage of the multi-loop amplitude generator GoSam-Xloop. All basic information about the process to be generated is defined in a *runcard*. These runcards have basically the same syntax as in the public one-loop version. An example for the process $u\bar{u} \to ZZ$ is shown in Figure A.1. The format of the input cards is mostly equivalent to the input cards used in the one-loop version of the program. The main new feature is the extension of the `order` parameter which can now take more than two powers in the coupling. The syntax of the order parameter is `order=<coupling name>,<power tree>,<power 1loop>, <power 2loop>,....` Options that are specific to the one-loop or the tree level are replicated under the basename suffixed with `higher`, see e.g. the `filter` parameter in the example in Figure A.1. The extension `reduze` must be activated for higher-than-one-loop amplitudes. The extension `dot2tex` is required for drawing higher-than-one-loop diagrams in the info file `process.pdf`. These options are given as a nested list such that the extended GoSam can in principle be used for any number of loops.

In addition to the runcard, a file with projection operators in `FORM` syntax and and one file with the integral families for each requested loop order as required for Reduze must be provided. The integral families should be provided in files with names `integralfamilies-Xloop.yaml`, where `X` is to be replaced with the number of loops of the contained families. These files are directly forwarded to Reduze, we therefore refer the reader to the documentation of Reduze for a detailed description.

The projectors must be provided in a file with the name `projectors.hh`. It should `#define` the `FORM` preprocessor variable `NUMPROJ` to the number of projection operators provided. This number should be equal to the one given in the runcard. The projectors file should further provide two procedures, `#Procedure ApplyProjectors` and `#Procedure ExpandProjectors`. An example is shown in Figure A.2.

The procedure `ApplyProjectors` should contract all indices of the stripped amplitude while it may introduce an arbitrary number of dummy symbols with the name `ProjCoeffX`, where `X` can be any string such that the resulting name is a valid name for a `FORM` symbol. For each initial and each final state particle, the amplitude has an overall factor of `inplorentz(2s, i, k, m)` (`outlorentz` for final state), where `s` denotes the spin, `k` the momentum, and `m` the mass of the particle. The index `i` is a Lorentz (boson) or a spinor index (fermion). In cases where particle and antiparticle are distinct, the parameter `2s` is signed (negative for the antiparticle). Spinor chains should be expressed using the function `NCContainer(<gamma matrices>, i1, i2)`, where the indices `i1` and `i2` denote the open spinor indices of the `<gamma matrices>`, and `<gamma matrices>` should be expressed using `Sm(mu)` for γ^μ, `Sm5(mu)` for $\frac{1}{2}\left(\gamma^\mu\gamma_5 - \gamma_5\gamma^\mu\right)$, and `Gamma5` for γ_5. All indices should be denoted using the symbols `iDUMMYX` analogous to

```
process_name=uuzz_massive_l2
process_path=uuzz_massive_l2

in=u,u~,Z,Z
out=
order=QCD, none, none, 4

# only [u] (massless) and [t] (massive) running in the loops
qgraf.verbatim=true=iprop[D,C,S,B,H,0,0];

# keep only diagrams with at least one massive top quark propagator
filter.higher= lambda d: d.iprop(T)>0

one=gs
zero=mU,mD,mS,mC,mB,wT,wZ

model=smdiag

projectors.number=10

extensions=reduze,dot2tex
```

Figure A.1: GoSam-Xloop runcard for the process $u\bar{u} \to ZZ$ mediated by top and bottom quark loops and requiring at least one top-quark propagator. Only the two-loop QCD corrections are requested here.

`ProjCoeffX`. The shorthand notation for slashed momenta, `Sm(k1)` meaning $\not{k}_1 \equiv \gamma_\mu k_1^\mu$ is permitted.

The procedure `ExpandProjectors` should rewrite the dummy symbols `ProjCoeffX` in terms of external momenta and the spacetime dimension `dimS`. For efficiency, products of multiple numerators with multiple terms can be kept together by placing them into the functions `ProjNum` and `Dim`. Denominators should be packed into the functions `ProjDen` and `DenDim`. Note that kinematic replacements are only applied to the arguments of `ProjNum` and `ProjDen`. Screening factors that are independent of the kinematics from kinematic replacements by placing them into the functions `Den` and `DenDim` can mean an important performance gain.

When all input files are prepared, then the first step is having GoSam generate the process directory which is done with the command

```
$ gosam.py uuzz_massive_l2.rc
```

assuming that the runcard's filename is `uuzz_massive_l2.rc`. The remaining steps are automated with `make`; i.e. further processing is invoked with the command make in the process directory.

```
1  #Define NUMPROJ "3"
2
3  #Procedure ApplyProjectors
4
5  id
6  inplorentz( 1, iDUMMY1?, k1, 0 )*
7  inplorentz(-1, iDUMMY2?, k2, 0 )*
8  inplorentz( 2, iDUMMY3?, k3, mZ)*
9  inplorentz( 2, iDUMMY4?, k4, mZ) =
10 + ProjCoeff1 * NCContainer(Sm(k1)*Sm(k3)*Sm(k2),iDUMMY1,iDUMMY2)*k1(
       iDUMMY3)*k4(iDUMMY4)*k2.k4
11 + ProjCoeff2 * NCContainer(Sm(k1)*Sm(iDUMMY3)*Sm(k3)*Sm(k4)*Sm(k2),
       iDUMMY1,iDUMMY2)*k4(iDUMMY4)
12 ;
13
14 #EndProcedure
15
16
17 #Procedure ExpandProjectors
18
19 id ProjCoeff1 =
20      ProjLabel1 * 1/2*ProjNum( - 2*k1.k3)*ProjNum( - 4*k1.k3 - 2*k2.k3
           )*ProjDen( - 2*k1.k3 - 2*k2.k3)^2*DenDim( - 3 + dimS)
21   - ProjLabel2 * Dim( - 5 + dimS)*DenDim( - 3 + dimS)*DenDim( - 4 +
       dimS)
22   + ProjLabel3 * 1/2*ProjNum( - 2*dimS*k1.k3 - 4*k2.k3)*ProjDen( - 2*
       dimS*k1.k3 - 2*k2.k3)^2*DenDim( - 3 + dimS)
23 ;
24
25 id ProjCoeff2 =
26   - ProjLabel1 * 1/8*Dim( - 5 + dimS)*DenDim( - 3 + dimS)
27   - ProjLabel3 * 8*ProjDen( - 4*k1.k3*k2.k3 - 2*k1.k3*k3.k3 - 2*k2.k3
       *k3.k3)*DenDim( - 4 + dimS)
28 ;
29
30 #EndProcedure
```

Figure A.2: Illustration of the syntax of the projectors file for the process $u\bar{u} \to ZZ$. This code snippet does *not* resemble the projectors used for the studies in Chapter 6. The complete set of projectors required to form helicity amplitudes is quite lengthy and therefore only a dummy file is shown.

B pySecDec Usage

This Appendix illustrates the basic use cases of pySecDec with simple examples. It is meant as a quick guide to introduce the main features of pySecDec without going into detail. Examples and the full documentation are included in the distribution tarballs of pySecDec which can be downloaded from `https://github.com/mppmu/secdec/releases/`. The documentation is also available online at `https://secdec.readthedocs.io/`.

B.1 Computing a Parameter Integral

The first step is defining an integral and instructing pySecDec to generate the necessary `FORM` code, which is further processed to `C++` code and finally compiled to a library in subsequent steps. The function which performs this task for a parameter integral is `make_package`. The minimal arguments to the function `make_package` are a name for the integral, the symbols denoting the integration variables and the regulators, the orders to expand to in the regulators, and a list of polynomials to decompose.

Consider for example the parameter integral

$$\int_0^1 \mathrm{d}x\,\mathrm{d}y\ (x+y)^{(-2+\varepsilon)}\,. \tag{B.1}$$

A minimal `python` program that instructs pySecDec to perform that first step for the integral defined in Equation (B.1) is shown in Figure B.1a.

The second step is writing code for the numerical integration, which loads the compiled integral library, defines the integrator and its options, and finally invokes the numerical integration. A minimal example of an integration program is shown in Figure B.1b.

Assuming the generate and the integrate programs shown in Figure B.1 are stored in files which are located in the same directory and named `generate_easy.py` and `integrate_easy.py`, respectively, then invoking the command shown in Figure B.2 prints the numerical result to the screen.

```
1  $ python generate_easy.py && make -C easy && python integrate_easy.py
2  <skipped some output>
3  Numerical Result:
4   + (1.0000000000000000e+00 +/- 5.74471364670693638e-12)*eps^-1 +
        (3.06903035514056288e-01 +/- 2.82319349818331089e-03) + O(eps)
```

Figure B.2: Command and output to compute the easy example with pySecDec.

```
from pySecDec import
    make_package

make_package(

  name = 'easy',
  integration_variables =
      ['x','y'],
  regulators = ['eps'],

  requested_orders = [0],
  polynomials_to_decompose =
      ['(x+y)^(-2+eps)'],

)
```

(a) generate

```
from pySecDec.integral_interface
    import IntegralLibrary

# load c++ library
easy_integral =
    IntegralLibrary(
    'easy/easy_pylink.so')

# integrate
_, _, result = easy_integral()

# print result
print('Numerical Result:')
print(result)
```

(b) integrate

Figure B.1: Input files to compute a simple integral with pySecDec.

Note that code generation, building of the integral library, and numerical integration are three separate commands. If the integral depends on further parameters, then only the integrate program has to be invoked for each set of numerical values for these parameters; i.e. the compiled library can be used for different values of the parameters and also for different settings of the numerical integration.

B.2 Feynman Parametrizing a Loop Integral

pySecDec implements classes to Feynman parametrize a loop integral given as either an integral in momentum representation or as a graph. An Example how to obtain the Symanzik polynomials $\mathcal{U}$ and $\mathcal{F}$ of the one-loop bubble shown in Figure B.3 from either representation with pySecDec is shown in Figure B.4.

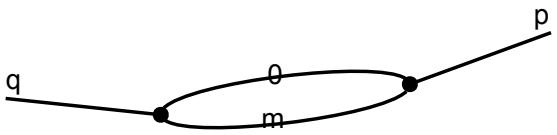

Figure B.3: A one-loop bubble with one massive line (mass m), one massless line and external legs with momenta p and q. A pdf file containing this pictorial representation is produced by the last command in Figure B.4b.

A loop integral in momentum representation as denoted in Equation (4.2) is entered as a list of `propagators`, a corresponding `powerlist` (optional, pySecDec assumes all propagator powers equal to one if absent), and a (possibly contracted or partially contracted) tensor `numerator` (optional, pySecDec assumes 1 if absent).

A graph is entered as lists of connections. Connections between two vertices are interpreted as quadratic propagators. These are entered in `internal_lines` and take the form [m,(v1,v2)], where v1 and v2 are the vertices to be connected and m is the mass of the corresponding propagator. A list of propagator powers can optionally be passed as well (all equal to one is assumed if omitted). Incoming and outgoing momenta are defined in the list `external_lines`, whose entries take the form (p,v), where p is the momentum coming in at the vertex v. Starting from the pictorial representation of a graph like the one-loop bubble shown in Figure B.3, the `internal_lines` and `external_lines` are constructed as follows: (i) Assign a label (integer or string) to each vertex. (ii) List all pairs of connections between the vertices (multiple connections should be entered multiple times); this list contains the `internal_lines`. (iii) List all incoming or outgoing momenta together with the appropriate vertices; these are the `external_lines`.

B.3 Computing a Loop Integral

Computing a loop integral is very similar to computing a generic regularized parameter integral as described in Appendix B.1. A not-Feynman-parametrized loop integral can be passed to pySecDec in two possible ways, as an integral in momentum representation or as a graph. Both input formats are discussed in Appendix B.2.

Consider for example the one-loop box with one off-shell leg (off-shellness s1) and one internal mass (with mass m and msq $\equiv$ m^2) shown in Figure B.5. Programs for the code generation using either input are shown in Figure B.6. In case the integral is passed to `loop_package` as a graph like shown in Figure B.6b, then the graphical representation shown in Figure B.5 is produced along with the other output.

The build process and a minimal program to perform the numerical integration is basically the same as in Appendix B.1 except that:

1. *easy* has to be replaced by *box1L* in the integration file of Figure B.1b (including the filename) and in the commands shown in Figure B.2.

2. Numerical values must be assigned to the `real_parameters` s, t, s1, and msq prior to numerical integration by changing line 7 of Figure B.1b to e.g.
   box1L_integral = foo(real_parameters=[4.0, −0.75, 1.25, 1.0]) .

The only subtlety about loop integrals compared to the easy example is the deformation of the contour to the complex plane. As shown in Section 4.4, the scaling parameters of the deformation λ_k must be small enough to form a valid contour. They must however also be large enough to result in a numerically stable integrand. The parameters λ_k are automatically adjusted according to heuristic algorithms to fulfill both requirements. These algorithms may fail which can result in the $\mathcal{F}$-polynomial obtaining an imaginary part of the wrong sign or the real part of the $\mathcal{U}$-polynomial becoming negative during numerical integration. pySecDec checks these conditions for every point and stops the integration if an invalid contour is detected with an appropriate error message. The minimum and maximum of the λ_k and the number of

samples used to optimize the contour can be set as arguments in the call that performs the integration; i.e. line 7 in Figure B.1b. A possible call would for example be

```
box1L_integral = foo(
    real_parameters = [4.0, -0.75, 1.25, 1.0],
    number_of_presamples = 10**6,
    deformation_parameters_maximum = 0.1,
    deformation_parameters_minimum = 1e-10
).
```

```
>>> from pySecDec.loop_integral import LoopIntegralFromPropagators

>>> one_loop_bubble = LoopIntegralFromPropagators(
...     propagators=['k^2-m^2',
...                  '(k-p)^2'],
...     loop_momenta=['k'])
...)

>>> one_loop_bubble.exponentiated_U
( + (1)*x0 + (1)*x1)**(2*eps - 2)

>>> one_loop_bubble.exponentiated_F
( + (m**2 - p**2)*x0*x1 + (m**2)*x0**2)**(-eps)

>>> one_loop_bubble.Gamma_factor
gamma(eps)
```

(a)

```
>>> from pySecDec.loop_integral import LoopIntegralFromGraph, plot_diagram

>>> bubble = LoopIntegralFromGraph(
... internal_lines=(['m',(1,2)],
...                 [ 0 ,(1,2)])
,
... external_lines=[('p',1),
...                 ('q',2)],
... replacement_rules=[('q','p')
]
...)

>>> bubble.exponentiated_U
( + (1)*x0 + (1)*x1)**(2*eps - 2)

>>> bubble.exponentiated_F
( + (m**2 - p**2)*x0*x1 + (m**2)*x0**2)**(-eps)

>>> bubble.Gamma_factor
gamma(eps)

>>> plot_diagram(
...   bubble.internal_lines,
...   bubble.external_lines,
...   filename='bubble1L',
...   Gstart=986089
... )
```

(b)

Figure B.4: Python commands to Feynman parametrize the one-loop bubble depicted in Figure B.3 with pySecDec where the loop integral is defined (a) in momentum representation or (b) as a graph. The last command in (b) creates a pdf file with the pictorial representation of the one-loop bubble shown in Figure B.3.

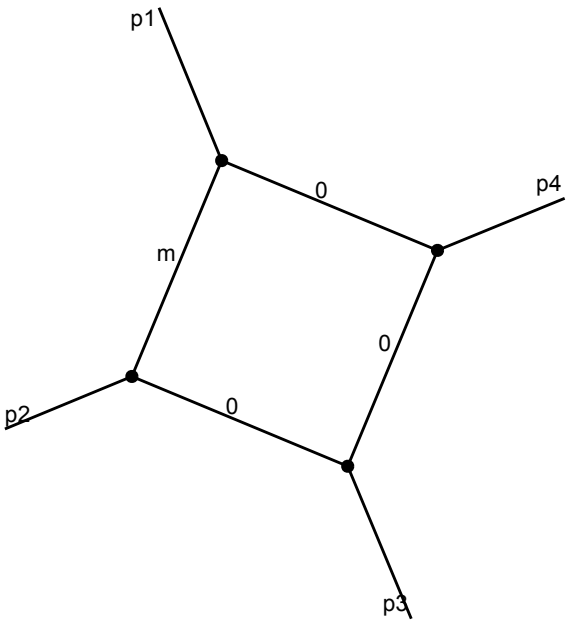

Figure B.5: A one-loop box with one internal mass m and external legs with momenta p1, p2, p3, and p4. This pictorial representation is produced along with the code to compute this integral when the loop-integral is passed to `loop_package` as a graph like shown in Figure B.6b.

```python
# define the loop integral
from pySecDec.loop_integral import LoopIntegralFromPropagators

li=LoopIntegralFromPropagators(
  loop_momenta = ['k1'],
  external_momenta = [
    'p1','p2',
    'p3','p4'
  ],
  propagators = [
    'k1^2-m^2',
    '(k1+p1)^2',
    '(k1+p1+p2)^2',
    '(k1+p1+p2+p3)^2'
  ],
 replacement_rules = [
    ('p1*p1', 's1'),
    ('p2*p2', 0),
    ('p3*p3', 0),
    ('p4*p4', 0),
    ('p3*p2', 't/2'),
    ('p1*p2', 's/2-s1/2'),
    ('p1*p4', 't/2-s1/2'),
    ('p2*p4', 's1/2-t/2-s/2'),
    ('p3*p4', 's/2'),
    ('m**2', 'msq')
  ]
)

# generate code
from pySecDec.loop_integral import loop_package
loop_package(
  name = 'box1L',
  loop_integral = li,
  real_parameters = ['s','t','s1','msq'],
  requested_order = 0
)
```

(a)

```python
# define the loop integral
from pySecDec.loop_integral import LoopIntegralFromGraph

li=LoopIntegralFromGraph(

  external_lines = [
    ['p1',1],['p2',2],
    ['p3',3],['p4',4]
  ],
  internal_lines = [
    ['m',[1,2]],
    [ 0 ,[2,3]],
    [ 0 ,[3,4]],
    [ 0 ,[4,1]]
  ],
  replacement_rules = [
    ('p1*p1', 's1'),
    ('p2*p2', 0),
    ('p3*p3', 0),
    ('p4*p4', 0),
    ('p3*p2', 't/2'),
    ('p1*p2', 's/2-s1/2'),
    ('p1*p4', 't/2-s1/2'),
    ('p2*p4', 's1/2-t/2-s/2'),
    ('p3*p4', 's/2'),
    ('m**2', 'msq')
  ]
)

# generate code
from pySecDec.loop_integral import loop_package
loop_package(
  name = 'box1L',
  loop_integral = li,
  real_parameters = ['s','t','s1','msq'],
  requested_order = 0
)
```

(b)

Figure B.6: Input files to generate code for the one-loop box depicted in Figure B.5 with pySecDec. The loop integral can be entered (a) as a graph or (b) as a list of propagators.

Acronyms

BLHA	Binoth Les Houches Accord
BSM	Beyond the Standard Model
CDF	Cumulative Distribution Function
CERN	conseil européen pour la recherche nucléaire
CPU	Central Processing Unit
EW	Electroweak
GPU	Graphics Processing Unit
IBP	Integration by Parts
IR	Infrared
KLN	Kinoshita Lee Nauenberg
LHC	Large Hadron Collider
LO	Leading Order
MC	Monte Carlo
NLO	Next-To-Leading Order
NNLO	Next-To-Next-To-Leading Order
NRQCD	non-relativistic Quantum Chromodynamics
OLP	one-loop provider
PDF	Parton Density Function
PNRQCD	potential-nonrelativistic Quantum Chromodynamics
QCD	Quantum Chromodynamics
QED	Quantum Electrodynamics
QFT	Quantum Field Theory
QMC	Quasi Monte Carlo
SCET	Soft-Collinear Effective Theory

SM	Standard Model (of particle physics)
UFO	Universal FeynRules Output
UV	Ultraviolet

List of Figures

List of Tables

Bibliography

[1] S. L. Glashow, *Partial Symmetries of Weak Interactions*, *Nucl. Phys.* **22** (1961) 579.

[2] S. Weinberg, *A Model of Leptons*, *Phys. Rev. Lett.* **19** (1967) 1264.

[3] A. Salam, *Weak and Electromagnetic Interactions*, *Conf. Proc.* **C680519** (1968) 367.

[4] S. L. Glashow, J. Iliopoulos and L. Maiani, *Weak Interactions with Lepton-Hadron Symmetry*, *Phys. Rev.* **D2** (1970) 1285.

[5] F. Englert and R. Brout, *Broken Symmetry and the Mass of Gauge Vector Mesons*, *Phys. Rev. Lett.* **13** (1964) 321.

[6] P. W. Higgs, *Broken symmetries, massless particles and gauge fields*, *Phys. Lett.* **12** (1964) 132.

[7] P. W. Higgs, *Broken Symmetries and the Masses of Gauge Bosons*, *Phys. Rev. Lett.* **13** (1964) 508.

[8] G. S. Guralnik, C. R. Hagen and T. W. B. Kibble, *Global Conservation Laws and Massless Particles*, *Phys. Rev. Lett.* **13** (1964) 585.

[9] P. W. Higgs, *Spontaneous Symmetry Breakdown without Massless Bosons*, *Phys. Rev.* **145** (1966) 1156.

[10] T. W. B. Kibble, *Symmetry breaking in nonAbelian gauge theories*, *Phys. Rev.* **155** (1967) 1554.

[11] D. J. Gross and F. Wilczek, *Ultraviolet Behavior of Nonabelian Gauge Theories*, *Phys. Rev. Lett.* **30** (1973) 1343.

[12] D. J. Gross and F. Wilczek, *Asymptotically Free Gauge Theories - I*, *Phys. Rev.* **D8** (1973) 3633.

[13] H. D. Politzer, *Reliable Perturbative Results for Strong Interactions?*, *Phys. Rev. Lett.* **30** (1973) 1346.

[14] H. Fritzsch, M. Gell-Mann and H. Leutwyler, *Advantages of the Color Octet Gluon Picture*, *Phys. Lett.* **47B** (1973) 365.

[15] W. Hollik, *Quantum field theory and the Standard Model*, in *High-energy physics. Proceedings, 17th European School, ESHEP 2009, Bautzen, Germany, June 14-27, 2009*, 2010, 1012.3883.

[16] J. Goldstone, *Field Theories with Superconductor Solutions*, *Nuovo Cim.* **19** (1961) 154.

[17] J. Goldstone, A. Salam and S. Weinberg, *Broken Symmetries*, *Phys. Rev.* **127** (1962) 965.

[18] M. E. Peskin and D. V. Schroeder, *An Introduction to quantum field theory*. Addison-Wesley, Reading, USA, 1995.

[19] ATLAS collaboration, G. Aad et al., *Observation of a new particle in the search for the Standard Model Higgs boson with the ATLAS detector at the LHC*, *Phys. Lett.* **B716** (2012) 1 [1207.7214].

[20] CMS collaboration, S. Chatrchyan et al., *Observation of a new boson at a mass of 125 GeV with the CMS experiment at the LHC*, *Phys. Lett.* **B716** (2012) 30 [1207.7235].

[21] T. Nakano and K. Nishijima, *Charge Independence for V-particles*, *Prog. Theor. Phys.* **10** (1953) 581.

[22] K. Nishijima, *Charge Independence Theory of V Particles*, *Prog. Theor. Phys.* **13** (1955) 285.

[23] M. Gell-Mann, *The interpretation of the new particles as displaced charge multiplets*, *Nuovo Cim.* **4** (1956) 848.

[24] M. C. Gonzalez-Garcia and M. Maltoni, *Phenomenology with Massive Neutrinos*, *Phys. Rept.* **460** (2008) 1 [0704.1800].

[25] F. Zwicky, *Die Rotverschiebung von extragalaktischen Nebeln*, *Helv. Phys. Acta* **6** (1933) 110.

[26] BaBar collaboration, J. P. Lees et al., *Measurement of an Excess of $\bar{B} \to D^{(*)}\tau^-\bar{\nu}_\tau$ Decays and Implications for Charged Higgs Bosons*, *Phys. Rev.* **D88** (2013) 072012 [1303.0571].

[27] LHCb collaboration, R. Aaij et al., *Measurement of Form-Factor-Independent Observables in the Decay $B^0 \to K^{*0}\mu^+\mu^-$*, *Phys. Rev. Lett.* **111** (2013) 191801 [1308.1707].

[28] LHCb collaboration, R. Aaij et al., *Test of lepton universality using $B^+ \to K^+\ell^+\ell^-$ decays*, *Phys. Rev. Lett.* **113** (2014) 151601 [1406.6482].

[29] LHCb collaboration, R. Aaij et al., *Measurement of the ratio of branching fractions $\mathcal{B}(\bar{B}^0 \to D^{*+}\tau^-\bar{\nu}_\tau)/\mathcal{B}(\bar{B}^0 \to D^{*+}\mu^-\bar{\nu}_\mu)$*, *Phys. Rev. Lett.* **115** (2015) 111803 [1506.08614].

[30] LHCb collaboration, R. Aaij et al., *Test of lepton universality with $B^0 \to K^{*0}\ell^+\ell^-$ decays*, *JHEP* **08** (2017) 055 [1705.05802].

[31] LHCb collaboration, R. Aaij et al., *Search for lepton-universality violation in $B^+ \to K^+\ell^+\ell^-$ decays*, 1903.09252.

[32] D. Buttazzo, A. Greljo, G. Isidori and D. Marzocca, *B-physics anomalies: a guide to combined explanations*, *JHEP* **11** (2017) 044 [1706.07808].

[33] LHCb collaboration, C. Langenbruch, *Lepton Flavour Universality tests in B decays as a probe for New Physics*, in *53rd Rencontres de Moriond on Electroweak Interactions and Unified Theories (Moriond EW 2018) La Thuile, Italy, March 10-17, 2018*, 2018, 1805.04370.

[34] Particle Data Group collaboration, M. Tanabashi et al., *Review of Particle Physics*, *Phys. Rev.* **D98** (2018) 030001.

[35] O. Brüning and L. Rossi, *The High Luminosity Large Hadron Collider*. WORLD SCIENTIFIC, 2015, 10.1142/9581.

[36] G. 't Hooft and M. J. G. Veltman, *Regularization and Renormalization of Gauge Fields*, *Nucl. Phys.* **B44** (1972) 189.

[37] G. Heinrich, *Colourful loops: Introduction to quantum chromodynamics and loop calculations*, 2018, available at: http://wwwth.mpp.mpg.de/members/gudrun/.

[38] M. Bohm, A. Denner and H. Joos, *Gauge theories of the strong and electroweak interaction*. Vieweg+Teubner Verlag, 2001, 10.1007/978-3-322-80160-9.

[39] G. Dissertori, I. G. Knowles and M. Schmelling, *High energy experiments and theory*. Oxford University Press, 2003.

[40] T. Kinoshita, *Mass singularities of feynman amplitudes*, *Journal of Mathematical Physics* **3** (1962) 650.

[41] T. D. Lee and M. Nauenberg, *Degenerate systems and mass singularities*, *Phys. Rev.* **133** (1964) B1549.

[42] S. Catani and M. H. Seymour, *A General algorithm for calculating jet cross-sections in NLO QCD*, *Nucl. Phys.* **B485** (1997) 291 [hep-ph/9605323].

[43] J. C. Collins, D. E. Soper and G. F. Sterman, *Factorization of Hard Processes in QCD*, *Adv. Ser. Direct. High Energy Phys.* **5** (1989) 1 [hep-ph/0409313].

[44] V. N. Gribov and L. N. Lipatov, *Deep inelastic e p scattering in perturbation theory*, *Sov. J. Nucl. Phys.* **15** (1972) 438.

[45] Y. L. Dokshitzer, *Calculation of the Structure Functions for Deep Inelastic Scattering and e+ e- Annihilation by Perturbation Theory in Quantum Chromodynamics.*, *Sov. Phys. JETP* **46** (1977) 641.

[46] G. Altarelli and G. Parisi, *Asymptotic Freedom in Parton Language*, *Nucl. Phys.* **B126** (1977) 298.

[47] S. Frixione, Z. Kunszt and A. Signer, *Three jet cross-sections to next-to-leading order*, *Nucl. Phys.* **B467** (1996) 399 [hep-ph/9512328].

[48] S. Frixione, *A General approach to jet cross-sections in QCD*, *Nucl. Phys.* **B507** (1997) 295 [hep-ph/9706545].

[49] W. T. Giele, E. W. N. Glover and D. A. Kosower, *Higher order corrections to jet cross-sections in hadron colliders*, *Nucl. Phys.* **B403** (1993) 633 [hep-ph/9302225].

[50] S. Catani and M. Grazzini, *An NNLO subtraction formalism in hadron collisions and its application to Higgs boson production at the LHC*, *Phys. Rev. Lett.* **98** (2007) 222002 [hep-ph/0703012].

[51] R. Bonciani, S. Catani, M. Grazzini, H. Sargsyan and A. Torre, *The q_T subtraction method for top quark production at hadron colliders*, *Eur. Phys. J.* **C75** (2015) 581 [1508.03585].

[52] J. Gao, C. S. Li and H. X. Zhu, *Top Quark Decay at Next-to-Next-to Leading Order in QCD*, *Phys. Rev. Lett.* **110** (2013) 042001 [1210.2808].

[53] R. Boughezal, C. Focke, X. Liu and F. Petriello, *W-boson production in association with a jet at next-to-next-to-leading order in perturbative QCD*, *Phys. Rev. Lett.* **115** (2015) 062002 [1504.02131].

[54] R. Boughezal, C. Focke, W. Giele, X. Liu and F. Petriello, *Higgs boson production in association with a jet at NNLO using jettiness subtraction*, *Phys. Lett.* **B748** (2015) 5 [1505.03893].

[55] J. Gaunt, M. Stahlhofen, F. J. Tackmann and J. R. Walsh, *N-jettiness Subtractions for NNLO QCD Calculations*, *JHEP* **09** (2015) 058 [1505.04794].

[56] I. W. Stewart, F. J. Tackmann and W. J. Waalewijn, *Factorization at the LHC: From PDFs to Initial State Jets*, *Phys. Rev.* **D81** (2010) 094035 [0910.0467].

[57] I. W. Stewart, F. J. Tackmann and W. J. Waalewijn, *N-Jettiness: An Inclusive Event Shape to Veto Jets*, *Phys. Rev. Lett.* **105** (2010) 092002 [1004.2489].

[58] F. Jegerlehner, *Facts of life with gamma(5)*, *Eur. Phys. J.* **C18** (2001) 673 [hep-th/0005255].

[59] S. A. Larin, *The Renormalization of the axial anomaly in dimensional regularization*, *Phys. Lett.* **B303** (1993) 113 [hep-ph/9302240].

[60] P. Breitenlohner and D. Maison, *Dimensional Renormalization and the Action Principle*, *Commun. Math. Phys.* **52** (1977) 11.

[61] V. V. Sudakov, *Vertex parts at very high-energies in quantum electrodynamics*, *Sov. Phys. JETP* **3** (1956) 65.

[62] S. Frixione and B. R. Webber, *Matching NLO QCD computations and parton shower simulations*, *JHEP* **06** (2002) 029 [hep-ph/0204244].

[63] P. Nason, *A New method for combining NLO QCD with shower Monte Carlo algorithms*, *JHEP* **11** (2004) 040 [hep-ph/0409146].

[64] S. Frixione, P. Nason and C. Oleari, *Matching NLO QCD computations with Parton Shower simulations: the POWHEG method*, *JHEP* **11** (2007) 070 [0709.2092].

[65] G. Cullen, N. Greiner, G. Heinrich, G. Luisoni, P. Mastrolia, G. Ossola et al., *Automated One-Loop Calculations with GoSam*, *Eur. Phys. J.* **C72** (2012) 1889 [1111.2034].

[66] G. Cullen et al., *GOSAM-2.0: a tool for automated one-loop calculations within the Standard Model and beyond*, *Eur. Phys. J.* **C74** (2014) 3001 [1404.7096].

[67] C. Degrande, C. Duhr, B. Fuks, D. Grellscheid, O. Mattelaer and T. Reiter, *UFO - The Universal FeynRules Output*, *Comput. Phys. Commun.* **183** (2012) 1201 [1108.2040].

[68] A. Semenov, *LanHEP - a package for automatic generation of Feynman rules from the Lagrangian. Updated version 3.1*, 1005.1909.

[69] P. Nogueira, *Automatic Feynman graph generation*, *J. Comput. Phys.* **105** (1993) 279.

[70] J. A. M. Vermaseren, *New features of FORM*, math-ph/0010025.

[71] M. Tentyukov and J. A. M. Vermaseren, *The Multithreaded version of FORM*, *Comput. Phys. Commun.* **181** (2010) 1419 [hep-ph/0702279].

[72] J. Kuipers, T. Ueda, J. A. M. Vermaseren and J. Vollinga, *FORM version 4.0*, *Comput. Phys. Commun.* **184** (2013) 1453 [1203.6543].

[73] J. Kuipers, T. Ueda and J. A. M. Vermaseren, *Code Optimization in FORM*, *Comput. Phys. Commun.* **189** (2015) 1 [1310.7007].

[74] B. Ruijl, T. Ueda and J. Vermaseren, *FORM version 4.2*, 1707.06453.

[75] G. Cullen, M. Koch-Janusz and T. Reiter, *Spinney: A Form Library for Helicity Spinors*, *Comput. Phys. Commun.* **182** (2011) 2368 [1008.0803].

[76] T. Reiter, *Optimising Code Generation with haggies*, *Comput. Phys. Commun.* **181** (2010) 1301 [0907.3714].

[77] G. Ossola, C. G. Papadopoulos and R. Pittau, *Reducing full one-loop amplitudes to scalar integrals at the integrand level*, *Nucl. Phys.* **B763** (2007) 147 [hep-ph/0609007].

[78] P. Mastrolia, G. Ossola, C. G. Papadopoulos and R. Pittau, *Optimizing the Reduction of One-Loop Amplitudes*, *JHEP* **06** (2008) 030 [0803.3964].

[79] R. K. Ellis, W. T. Giele, Z. Kunszt and K. Melnikov, *Masses, fermions and generalized D-dimensional unitarity*, *Nucl. Phys.* **B822** (2009) 270 [0806.3467].

[80] G. Heinrich, G. Ossola, T. Reiter and F. Tramontano, *Tensorial Reconstruction at the Integrand Level*, *JHEP* **10** (2010) 105 [1008.2441].

[81] T. Binoth, J. P. Guillet, G. Heinrich, E. Pilon and T. Reiter, *Golem95: A Numerical program to calculate one-loop tensor integrals with up to six external legs*, *Comput. Phys. Commun.* **180** (2009) 2317 [0810.0992].

[82] G. Cullen, J. P. Guillet, G. Heinrich, T. Kleinschmidt, E. Pilon, T. Reiter et al., *Golem95C: A library for one-loop integrals with complex masses*, *Comput. Phys. Commun.* **182** (2011) 2276 [1101.5595].

[83] J. P. Guillet, G. Heinrich and J. F. von Soden-Fraunhofen, *Tools for NLO automation: extension of the golem95C integral library*, *Comput. Phys. Commun.* **185** (2014) 1828 [1312.3887].

[84] P. Mastrolia, G. Ossola, T. Reiter and F. Tramontano, *Scattering AMplitudes from Unitarity-based Reduction Algorithm at the Integrand-level*, *JHEP* **08** (2010) 080 [1006.0710].

[85] H. van Deurzen, *Associated Higgs Production at NLO with GoSam*, *Acta Phys. Polon.* **B44** (2013) 2223.

[86] P. Mastrolia, E. Mirabella and T. Peraro, *Integrand reduction of one-loop scattering amplitudes through Laurent series expansion*, *JHEP* **06** (2012) 095 [1203.0291].

[87] H. van Deurzen, G. Luisoni, P. Mastrolia, E. Mirabella, G. Ossola and T. Peraro, *Multi-leg One-loop Massive Amplitudes from Integrand Reduction via Laurent Expansion*, *JHEP* **03** (2014) 115 [1312.6678].

[88] T. Peraro, *Ninja: Automated Integrand Reduction via Laurent Expansion for One-Loop Amplitudes*, *Comput. Phys. Commun.* **185** (2014) 2771 [1403.1229].

[89] J. Fleischer and T. Riemann, *A Complete algebraic reduction of one-loop tensor Feynman integrals*, *Phys. Rev.* **D83** (2011) 073004 [1009.4436].

[90] J. Fleischer, T. Riemann and V. Yundin, *New developments in PJFry*, 1210.4095.

[91] A. van Hameren, *OneLOop: For the evaluation of one-loop scalar functions*, *Comput. Phys. Commun.* **182** (2011) 2427 [1007.4716].

[92] G. J. van Oldenborgh, *FF: A Package to evaluate one loop Feynman diagrams*, *Comput. Phys. Commun.* **66** (1991) 1.

[93] R. K. Ellis and G. Zanderighi, *Scalar one-loop integrals for QCD*, *JHEP* **02** (2008) 002 [0712.1851].

[94] C. W. Bauer, F. J. Tackmann and J. Thaler, *GenEvA. I. A New framework for event generation*, *JHEP* **12** (2008) 010 [0801.4026].

[95] C. W. Bauer, F. J. Tackmann and J. Thaler, *GenEvA. II. A Phase space generator from a reweighted parton shower*, *JHEP* **12** (2008) 011 [0801.4028].

[96] G. Bevilacqua, M. Czakon, M. V. Garzelli, A. van Hameren, Y. Malamos, C. G. Papadopoulos et al., *NLO QCD calculations with HELAC-NLO*, *Nucl. Phys. Proc. Suppl.* **205-206** (2010) 211 [1007.4918].

[97] G. Bevilacqua, M. Czakon, M. V. Garzelli, A. van Hameren, A. Kardos, C. G. Papadopoulos et al., *HELAC-NLO*, *Comput. Phys. Commun.* **184** (2013) 986 [1110.1499].

[98] M. Bahr et al., *Herwig++ Physics and Manual*, *Eur. Phys. J.* **C58** (2008) 639 [0803.0883].

[99] J. Bellm et al., *Herwig 7.0/Herwig++ 3.0 release note*, *Eur. Phys. J.* **C76** (2016) 196 [1512.01178].

[100] J. Alwall, R. Frederix, S. Frixione, V. Hirschi, F. Maltoni, O. Mattelaer et al., *The automated computation of tree-level and next-to-leading order differential cross sections, and their matching to parton shower simulations*, *JHEP* **07** (2014) 079 [1405.0301].

[101] S. Alioli, P. Nason, C. Oleari and E. Re, *A general framework for implementing NLO calculations in shower Monte Carlo programs: the POWHEG BOX*, *JHEP* **06** (2010) 043 [1002.2581].

[102] T. Sjöstrand, S. Ask, J. R. Christiansen, R. Corke, N. Desai, P. Ilten et al., *An Introduction to PYTHIA 8.2*, *Comput. Phys. Commun.* **191** (2015) 159 [1410.3012].

[103] T. Gleisberg, S. Hoeche, F. Krauss, M. Schonherr, S. Schumann, F. Siegert et al., *Event generation with SHERPA 1.1*, *JHEP* **02** (2009) 007 [0811.4622].

[104] N. Fischer, S. Prestel, M. Ritzmann and P. Skands, *Vincia for Hadron Colliders*, *Eur. Phys. J.* **C76** (2016) 589 [1605.06142].

[105] M. Moretti, T. Ohl and J. Reuter, *O'Mega: An Optimizing matrix element generator*, hep-ph/0102195.

[106] W. Kilian, T. Ohl and J. Reuter, *WHIZARD: Simulating Multi-Particle Processes at LHC and ILC*, *Eur. Phys. J.* **C71** (2011) 1742 [0708.4233].

[107] C. F. Berger, Z. Bern, L. J. Dixon, F. Febres Cordero, D. Forde, H. Ita et al., *An Automated Implementation of On-Shell Methods for One-Loop Amplitudes*, *Phys. Rev.* **D78** (2008) 036003 [0803.4180].

[108] J. Kublbeck, M. Bohm and A. Denner, *Feyn Arts: Computer Algebraic Generation of Feynman Graphs and Amplitudes*, *Comput. Phys. Commun.* **60** (1990) 165.

[109] T. Hahn, *Generating Feynman diagrams and amplitudes with FeynArts 3*, *Comput. Phys. Commun.* **140** (2001) 418 [hep-ph/0012260].

[110] V. Hirschi, R. Frederix, S. Frixione, M. V. Garzelli, F. Maltoni and R. Pittau, *Automation of one-loop QCD corrections*, *JHEP* **05** (2011) 044 [1103.0621].

[111] F. Cascioli, P. Maierhofer and S. Pozzorini, *Scattering Amplitudes with Open Loops*, *Phys. Rev. Lett.* **108** (2012) 111601 [1111.5206].

[112] A. Denner, J.-N. Lang and S. Uccirati, *NLO electroweak corrections in extended Higgs Sectors with RECOLA2*, *JHEP* **07** (2017) 087 [1705.06053].

[113] A. Denner, J.-N. Lang and S. Uccirati, *Recola2: REcursive Computation of One-Loop Amplitudes 2*, *Comput. Phys. Commun.* **224** (2018) 346 [1711.07388].

[114] K. Arnold et al., *VBFNLO: A Parton level Monte Carlo for processes with electroweak bosons*, *Comput. Phys. Commun.* **180** (2009) 1661 [0811.4559].

[115] J. Baglio et al., *VBFNLO: A Parton Level Monte Carlo for Processes with Electroweak Bosons – Manual for Version 2.7.0*, 1107.4038.

[116] J. Baglio et al., *Release Note - VBFNLO 2.7.0*, 1404.3940.

[117] J. M. Campbell and R. K. Ellis, *An Update on vector boson pair production at hadron colliders*, *Phys. Rev.* **D60** (1999) 113006 [hep-ph/9905386].

[118] J. M. Campbell, R. K. Ellis and C. Williams, *Vector boson pair production at the LHC*, *JHEP* **07** (2011) 018 [1105.0020].

[119] J. M. Campbell, R. K. Ellis and W. T. Giele, *A Multi-Threaded Version of MCFM*, *Eur. Phys. J.* **C75** (2015) 246 [1503.06182].

[120] T. Binoth et al., *A Proposal for a standard interface between Monte Carlo tools and one-loop programs*, *Comput. Phys. Commun.* **181** (2010) 1612 [1001.1307].

[121] S. Alioli et al., *Update of the Binoth Les Houches Accord for a standard interface between Monte Carlo tools and one-loop programs*, *Comput. Phys. Commun.* **185** (2014) 560 [1308.3462].

[122] S. Laporta, *High precision calculation of multiloop Feynman integrals by difference equations*, *Int. J. Mod. Phys.* **A15** (2000) 5087 [hep-ph/0102033].

[123] A. V. Kotikov, *Differential equations method: New technique for massive Feynman diagrams calculation*, *Phys. Lett.* **B254** (1991) 158.

[124] A. V. Kotikov, *Differential equation method: The Calculation of N point Feynman diagrams*, *Phys. Lett.* **B267** (1991) 123.

[125] E. Remiddi, *Differential equations for Feynman graph amplitudes*, *Nuovo Cim.* **A110** (1997) 1435 [hep-th/9711188].

[126] T. Gehrmann and E. Remiddi, *Differential equations for two loop four point functions*, *Nucl. Phys.* **B580** (2000) 485 [hep-ph/9912329].

[127] M. Argeri and P. Mastrolia, *Feynman Diagrams and Differential Equations*, *Int. J. Mod. Phys.* **A22** (2007) 4375 [0707.4037].

[128] J. M. Henn, *Multiloop integrals in dimensional regularization made simple*, *Phys. Rev. Lett.* **110** (2013) 251601 [1304.1806].

[129] J. M. Henn, *Lectures on differential equations for Feynman integrals*, *J. Phys.* **A48** (2015) 153001 [1412.2296].

[130] C. Bogner, S. Borowka, T. Hahn, G. Heinrich, S. P. Jones, M. Kerner et al., *Loopedia, a Database for Loop Integrals*, *Comput. Phys. Commun.* **225** (2018) 1 [1709.01266].

[131] E. Panzer, *On hyperlogarithms and Feynman integrals with divergences and many scales*, *JHEP* **03** (2014) 071 [1401.4361].

[132] A. von Manteuffel, E. Panzer and R. M. Schabinger, *A quasi-finite basis for multi-loop Feynman integrals*, *JHEP* **02** (2015) 120 [1411.7392].

[133] A. von Manteuffel, E. Panzer and R. M. Schabinger, *On the Computation of Form Factors in Massless QCD with Finite Master Integrals*, *Phys. Rev.* **D93** (2016) 125014 [1510.06758].

[134] A. von Manteuffel and R. M. Schabinger, *Numerical Multi-Loop Calculations via Finite Integrals and One-Mass EW-QCD Drell-Yan Master Integrals*, *JHEP* **04** (2017) 129 [1701.06583].

[135] T. Binoth and G. Heinrich, *An automatized algorithm to compute infrared divergent multiloop integrals*, *Nucl. Phys.* **B585** (2000) 741 [hep-ph/0004013].

[136] G. Heinrich, *Sector Decomposition*, *Int. J. Mod. Phys.* **A23** (2008) 1457 [0803.4177].

[137] S. Becker and S. Weinzierl, *Direct numerical integration for multi-loop integrals*, *Eur. Phys. J.* **C73** (2013) 2321 [1211.0509].

[138] E. de Doncker, F. Yuasa, K. Kato, T. Ishikawa, J. Kapenga and O. Olagbemi, *Regularization with Numerical Extrapolation for Finite and UV-Divergent Multi-loop Integrals*, *Comput. Phys. Commun.* **224** (2018) 164 [1702.04904].

[139] M. K. Mandal and X. Zhao, *Evaluating multi-loop Feynman integrals numerically through differential equations*, *JHEP* **03** (2019) 190 [1812.03060].

[140] C. Anastasiou and A. Daleo, *Numerical evaluation of loop integrals*, *JHEP* **10** (2006) 031 [hep-ph/0511176].

[141] M. Czakon, *Automatized analytic continuation of Mellin-Barnes integrals*, *Comput. Phys. Commun.* **175** (2006) 559 [hep-ph/0511200].

[142] J. Gluza, K. Kajda, T. Riemann and V. Yundin, *Numerical Evaluation of Tensor Feynman Integrals in Euclidean Kinematics*, *Eur. Phys. J.* **C71** (2011) 1516 [1010.1667].

[143] I. Dubovyk, J. Gluza, T. Riemann and J. Usovitsch, *Numerical integration of massive two-loop Mellin-Barnes integrals in Minkowskian regions*, *PoS* **LL2016** (2016) 034 [1607.07538].

[144] M. Prausa, *Mellin–Barnes meets Method of Brackets: a novel approach to Mellin–Barnes representations of Feynman integrals*, *Eur. Phys. J.* **C77** (2017) 594 [1706.09852].

[145] A. Freitas, *Numerical multi-loop integrals and applications*, *Prog. Part. Nucl. Phys.* **90** (2016) 201 [1604.00406].

[146] S. Borowka, T. Gehrmann and D. Hulme, *Systematic approximation of multi-scale Feynman integrals*, *JHEP* **08** (2018) 111 [1804.06824].

[147] S. Moch, J. A. M. Vermaseren and A. Vogt, *On γ_5 in higher-order QCD calculations and the NNLO evolution of the polarized valence distribution*, *Phys. Lett.* **B748** (2015) 432 [1506.04517].

[148] A. von Manteuffel and C. Studerus, *Reduze 2 - Distributed Feynman Integral Reduction*, 1201.4330.

[149] C. Studerus, *Reduze-Feynman Integral Reduction in C++*, *Comput. Phys. Commun.* **181** (2010) 1293 [0912.2546].

[150] C. Anastasiou and A. Lazopoulos, *Automatic integral reduction for higher order perturbative calculations*, *JHEP* **07** (2004) 046 [hep-ph/0404258].

[151] A. V. Smirnov, *Algorithm FIRE – Feynman Integral REduction*, *JHEP* **10** (2008) 107 [0807.3243].

[152] A. V. Smirnov and V. A. Smirnov, *FIRE4, LiteRed and accompanying tools to solve integration by parts relations*, *Comput. Phys. Commun.* **184** (2013) 2820 [1302.5885].

[153] A. V. Smirnov, *FIRE5: a C++ implementation of Feynman Integral REduction*, *Comput. Phys. Commun.* **189** (2015) 182 [1408.2372].

[154] A. V. Smirnov and F. S. Chuharev, *FIRE6: Feynman Integral REduction with Modular Arithmetic*, 1901.07808.

[155] R. N. Lee, *Presenting LiteRed: a tool for the Loop InTEgrals REDuction*, 1212.2685.

[156] R. N. Lee, *LiteRed 1.4: a powerful tool for reduction of multiloop integrals*, *J. Phys. Conf. Ser.* **523** (2014) 012059 [1310.1145].

[157] P. Maierhöfer, J. Usovitsch and P. Uwer, *Kira—A Feynman integral reduction program*, *Comput. Phys. Commun.* **230** (2018) 99 [1705.05610].

[158] P. Maierhöfer and J. Usovitsch, *Kira 1.2 Release Notes*, 1812.01491.

[159] F. V. Tkachov, *A Theorem on Analytical Calculability of Four Loop Renormalization Group Functions*, *Phys. Lett.* **100B** (1981) 65.

[160] K. G. Chetyrkin and F. V. Tkachov, *Integration by Parts: The Algorithm to Calculate beta Functions in 4 Loops*, *Nucl. Phys.* **B192** (1981) 159.

[161] S. Borowka, G. Heinrich, S. Jahn, S. P. Jones, M. Kerner, J. Schlenk et al., *pySecDec: a toolbox for the numerical evaluation of multi-scale integrals*, *Comput. Phys. Commun.* **222** (2018) 313 [1703.09692].

[162] S. Borowka, G. Heinrich, S. Jahn, S. P. Jones, M. Kerner and J. Schlenk, *A GPU compatible quasi-Monte Carlo integrator interfaced to pySecDec*, *Comput. Phys. Commun.* **240** (2019) 120 [1811.11720].

[163] C. Bogner and S. Weinzierl, *Resolution of singularities for multi-loop integrals*, *Comput. Phys. Commun.* **178** (2008) 596 [0709.4092].

[164] A. V. Smirnov and M. N. Tentyukov, *Feynman Integral Evaluation by a Sector decomposiTion Approach (FIESTA)*, *Comput. Phys. Commun.* **180** (2009) 735 [0807.4129].

[165] A. V. Smirnov, V. A. Smirnov and M. Tentyukov, *FIESTA 2: Parallelizeable multiloop numerical calculations*, *Comput. Phys. Commun.* **182** (2011) 790 [0912.0158].

[166] A. V. Smirnov, *FIESTA 3: cluster-parallelizable multiloop numerical calculations in physical regions*, *Comput. Phys. Commun.* **185** (2014) 2090 [1312.3186].

[167] A. V. Smirnov, *FIESTA4: Optimized Feynman integral calculations with GPU support*, *Comput. Phys. Commun.* **204** (2016) 189 [1511.03614].

[168] J. Carter and G. Heinrich, *SecDec: A general program for sector decomposition*, *Comput. Phys. Commun.* **182** (2011) 1566 [1011.5493].

[169] S. Borowka, J. Carter and G. Heinrich, *Numerical Evaluation of Multi-Loop Integrals for Arbitrary Kinematics with SecDec 2.0*, *Comput. Phys. Commun.* **184** (2013) 396 [1204.4152].

[170] S. Borowka, G. Heinrich, S. P. Jones, M. Kerner, J. Schlenk and T. Zirke, *SecDec-3.0: numerical evaluation of multi-scale integrals beyond one loop*, *Comput. Phys. Commun.* **196** (2015) 470 [1502.06595].

[171] A. Meurer, C. P. Smith, M. Paprocki, O. Čertík, S. B. Kirpichev, M. Rocklin et al., *Sympy: symbolic computing in python*, *PeerJ Computer Science* **3** (2017) e103.

[172] P. Gonnet, *Increasing the reliability of adaptive quadrature using explicit interpolants*, *ACM Trans. Math. Softw.* **37** (2010) 26:1 [1006.3962].

[173] M. Galassi, J. Davies, J. Theiler, B. Gough, G. Jungman, P. Alken et al., *GNU Scientific Library Reference Manual - Third Edition*. Network Theory Ltd., 3rd ed., 2009.

[174] T. Hahn, *CUBA: A Library for multidimensional numerical integration*, *Comput. Phys. Commun.* **168** (2005) 78 [hep-ph/0404043].

[175] T. Hahn, *Concurrent Cuba*, *J. Phys. Conf. Ser.* **608** (2015) 012066 [1408.6373].

[176] Z. Li, J. Wang, Q.-S. Yan and X. Zhao, *Efficient numerical evaluation of Feynman integrals*, *Chin. Phys.* **C40** (2016) 033103 [1508.02512].

[177] V. A. Smirnov, *Feynman integral calculus*. Springer-Verlag Berlin Heidelberg, 2006, 10.1007/3-540-30611-0.

[178] O. I. Zavialov, *Renormalized Quantum Field Theory*. Springer Netherlands, 1990, 10.1007/978-94-009-2585-4.

[179] H. Cheng and T. T. Wu, *EXPANDING PROTONS: SCATTERING AT HIGH-ENERGIES*. 1987.

[180] T. Kaneko and T. Ueda, *A Geometric method of sector decomposition*, *Comput. Phys. Commun.* **181** (2010) 1352 [0908.2897].

[181] T. Kaneko and T. Ueda, *Sector Decomposition Via Computational Geometry*, *PoS* **ACAT2010** (2010) 082 [1004.5490].

[182] J. Schlenk and T. Zirke, *Calculation of Multi-Loop Integrals with SecDec-3.0*, *PoS* **RADCOR2015** (2016) 106 [1601.03982].

[183] J. K. Schlenk, *Techniques for higher order corrections and their application to LHC phenomenology*, dissertation, Technische Universität München, München, 2016.

[184] S. Jahn, *Numerical evaluation of multi-loop integrals*, *PoS* **LL2018** (2018) 019 [1811.11722].

[185] I. Dubovyk, A. Freitas, J. Gluza, T. Riemann and J. Usovitsch, *30 years, some 700 integrals, and 1 dessert, or: Electroweak two-loop corrections to the $Z\bar{b}b$ vertex*, *PoS* **LL2016** (2016) 075 [1610.07059].

[186] J. Fleischer, A. V. Kotikov and O. L. Veretin, *Analytic two loop results for selfenergy type and vertex type diagrams with one nonzero mass*, *Nucl. Phys.* **B547** (1999) 343 [hep-ph/9808242].

[187] D. E. Soper, *Techniques for QCD calculations by numerical integration*, *Phys. Rev.* **D62** (2000) 014009 [hep-ph/9910292].

[188] T. Binoth, J. P. Guillet, G. Heinrich, E. Pilon and C. Schubert, *An Algebraic/numerical formalism for one-loop multi-leg amplitudes*, *JHEP* **10** (2005) 015 [hep-ph/0504267].

[189] C. Anastasiou, S. Beerli and A. Daleo, *Evaluating multi-loop Feynman diagrams with infrared and threshold singularities numerically*, *JHEP* **05** (2007) 071 [hep-ph/0703282].

[190] S. C. Borowka, *Evaluation of multi-loop multi-scale integrals and phenomenological two-loop applications*, dissertation, Technische Universität München, München, 2014.

[191] A. Pak, *The Toolbox of modern multi-loop calculations: novel analytic and semi-analytic techniques*, *J. Phys. Conf. Ser.* **368** (2012) 012049 [1111.0868].

[192] B. D. McKay and A. Piperno, *Practical graph isomorphism, ii*, *Journal of Symbolic Computation* **60** (2014) 94 .

[193] S. P. Jones and B. Ruijl, *Numerical Methods and the 4-point 2-loop Higgs amplitudes*, *J. Phys. Conf. Ser.* **1085** (2018) 052009 [1806.02593].

[194] S. Jahn, *Integral symmetries with pySecDec*, *PoS* **CORFU2017** (2018) 132.

[195] J. Dick, F. Y. Kuo and I. H. Sloan, *High-dimensional integration: The quasi-monte carlo way*, *Acta Numerica* **22** (2013) 133–288.

[196] D. Nuyens and R. Cools, *Fast algorithms for component-by-component construction of rank-1 lattice rules in shift-invariant reproducing kernel hilbert spaces*, *Mathematics of Computation* **75** (2006) 903.

[197] N. M. Korobov, *Number-theoretic methods in approximate analysis*, *Fizmatgiz* **Moscow** (1963).

[198] D. P. Laurie, *Periodizing transformations for numerical integration*, *Journal of Computational and Applied Mathematics* **66** (1996) 337 .

[199] F. Y. Kuo, I. H. Sloan and H. Woźniakowski, *Periodization strategy may fail in high dimensions*, *Numerical Algorithms* **46** (2007) 369.

[200] F. J. Hickernell, *Obtaining $o(n^{-2+\varepsilon})$ convergence for lattice quadrature rules*, in *Monte Carlo and Quasi-Monte Carlo Methods 2000* (K.-T. Fang, H. Niederreiter and F. J. Hickernell, eds.), (Berlin, Heidelberg), pp. 274–289, Springer Berlin Heidelberg, 2002, DOI: 10.1007/978-3-642-56046-0_18.

[201] A. Sidi, *A new variable transformation for numerical integration*, in *Numerical Integration IV: Proceedings of the Conference at the Mathematical Research Institute, Oberwolfach, November 8–14, 1992, editors H. Brass and G. Hämmerlin*, (Basel), pp. 359–373, Birkhäuser Basel, 1993, DOI: 10.1007/978-3-0348-6338-4_27.

[202] A. Sidi, *Extension of a class of periodizing variable transformations for numerical integration*, *J. Math. Comp.* **75** (2006) 327.

[203] E. de Doncker, A. Almulihi and F. Yuasa, *High-speed evaluation of loop integrals using lattice rules*, *J. Phys. Conf. Ser.* **1085** (2018) 052005.

[204] G. P. Lepage, *A New Algorithm for Adaptive Multidimensional Integration*, *J. Comput. Phys.* **27** (1978) 192.

[205] S. Borowka, N. Greiner, G. Heinrich, S. Jones, M. Kerner, J. Schlenk et al., *Higgs Boson Pair Production in Gluon Fusion at Next-to-Leading Order with Full Top-Quark Mass Dependence*, *Phys. Rev. Lett.* **117** (2016) 012001 [1604.06447].

[206] S. Borowka, N. Greiner, G. Heinrich, S. P. Jones, M. Kerner, J. Schlenk et al., *Full top quark mass dependence in Higgs boson pair production at NLO*, *JHEP* **10** (2016) 107 [1608.04798].

[207] S. P. Jones, M. Kerner and G. Luisoni, *Next-to-Leading-Order QCD Corrections to Higgs Boson Plus Jet Production with Full Top-Quark Mass Dependence*, *Phys. Rev. Lett.* **120** (2018) 162001 [1802.00349].

[208] M. Kerner, *Next-to-Leading Order QCD Corrections to Vector Boson Pair Production in Association with two Jets at the LHC*, Ph.D. thesis, KIT, Karlsruhe, TP, 2014.

[209] L. Chen, G. Heinrich, S. Jahn, S. P. Jones, M. Kerner, J. Schlenk et al., *Photon pair production in gluon fusion: Top quark effects at NLO with threshold matching*, 1911.09314.

[210] CMS collaboration, S. Chatrchyan et al., *Measurement of differential cross sections for the production of a pair of isolated photons in pp collisions at $\sqrt{s} = 7$ TeV*, *Eur. Phys. J.* **C74** (2014) 3129 [1405.7225].

[211] ATLAS collaboration, M. Aaboud et al., *Measurements of integrated and differential cross sections for isolated photon pair production in pp collisions at $\sqrt{s} = 8$ TeV with the ATLAS detector*, *Phys. Rev.* **D95** (2017) 112005 [1704.03839].

[212] D. A. Dicus and S. S. D. Willenbrock, *Photon Pair Production and the Intermediate Mass Higgs Boson*, *Phys. Rev.* **D37** (1988) 1801.

[213] L. J. Dixon and M. S. Siu, *Resonance continuum interference in the diphoton Higgs signal at the LHC*, *Phys. Rev. Lett.* **90** (2003) 252001 [hep-ph/0302233].

[214] S. P. Martin, *Shift in the LHC Higgs Diphoton Mass Peak from Interference with Background*, *Phys. Rev.* **D86** (2012) 073016 [1208.1533].

[215] D. de Florian, N. Fidanza, R. J. Hernández-Pinto, J. Mazzitelli, Y. Rotstein Habarnau and G. F. R. Sborlini, *A complete $O(\alpha_S^2)$ calculation of the signal-background interference for the Higgs diphoton decay channel*, *Eur. Phys. J.* **C73** (2013) 2387 [1303.1397].

[216] S. P. Martin, *Interference of Higgs Diphoton Signal and Background in Production with a Jet at the LHC*, *Phys. Rev.* **D88** (2013) 013004 [1303.3342].

[217] L. J. Dixon and Y. Li, *Bounding the Higgs Boson Width Through Interferometry*, *Phys. Rev. Lett.* **111** (2013) 111802 [1305.3854].

[218] J. Campbell, M. Carena, R. Harnik and Z. Liu, *Interference in the $gg \to h \to \gamma\gamma$ On-Shell Rate and the Higgs Boson Total Width*, *Phys. Rev. Lett.* **119** (2017) 181801 [1704.08259].

[219] L. Cieri, F. Coradeschi, D. de Florian and N. Fidanza, *Transverse-momentum resummation for the signal-background interference in the $H \to \gamma\gamma$ channel at the LHC*, *Phys. Rev.* **D96** (2017) 054003 [1706.07331].

[220] ATLAS collaboration, M. Aaboud et al., *Search for resonances in diphoton events at $\sqrt{s}$=13 TeV with the ATLAS detector*, *JHEP* **09** (2016) 001 [1606.03833].

[221] CMS collaboration, A. M. Sirunyan et al., *Search for physics beyond the standard model in high-mass diphoton events from proton-proton collisions at $\sqrt{s} = 13$ TeV*, *Phys. Rev.* **D98** (2018) 092001 [1809.00327].

[222] S. R. Dugad, P. Jain, S. Mitra, P. Sanyal and R. K. Verma, *The top threshold effect in the $\gamma\gamma$ production at the LHC*, *Eur. Phys. J.* **C78** (2018) 715 [1605.07360].

[223] S. Kawabata and H. Yokoya, *Top-quark mass from the diphoton mass spectrum*, *Eur. Phys. J.* **C77** (2017) 323 [1607.00990].

[224] T. Binoth, J. P. Guillet, E. Pilon and M. Werlen, *A Full next-to-leading order study of direct photon pair production in hadronic collisions*, *Eur. Phys. J.* **C16** (2000) 311 [hep-ph/9911340].

[225] C. Balazs, E. L. Berger, P. M. Nadolsky and C. P. Yuan, *Calculation of prompt diphoton production cross-sections at Tevatron and LHC energies*, *Phys. Rev.* **D76** (2007) 013009 [0704.0001].

[226] Z. Bern, A. De Freitas and L. J. Dixon, *Two loop amplitudes for gluon fusion into two photons*, *JHEP* **09** (2001) 037 [hep-ph/0109078].

[227] Z. Bern, L. J. Dixon and C. Schmidt, *Isolating a light Higgs boson from the diphoton background at the CERN LHC*, *Phys. Rev.* **D66** (2002) 074018 [hep-ph/0206194].

[228] F. Maltoni, M. K. Mandal and X. Zhao, *Top-quark effects in diphoton production through gluon fusion at next-to-leading order in QCD*, *Phys. Rev.* **D100** (2019) 071501 [1812.08703].

[229] M. Czakon, *Tops from Light Quarks: Full Mass Dependence at Two-Loops in QCD*, *Phys. Lett.* **B664** (2008) 307 [0803.1400].

[230] S. Caron-Huot and J. M. Henn, *Iterative structure of finite loop integrals*, *JHEP* **06** (2014) 114 [1404.2922].

[231] M. Becchetti and R. Bonciani, *Two-Loop Master Integrals for the Planar QCD Massive Corrections to Di-photon and Di-jet Hadro-production*, *JHEP* **01** (2018) 048 [1712.02537].

[232] A. von Manteuffel and L. Tancredi, *A non-planar two-loop three-point function beyond multiple polylogarithms*, *JHEP* **06** (2017) 127 [1701.05905].

[233] J. Broedel, C. Duhr, F. Dulat, B. Penante and L. Tancredi, *Elliptic polylogarithms and Feynman parameter integrals*, *JHEP* **05** (2019) 120 [1902.09971].

[234] U. Aglietti, R. Bonciani, G. Degrassi and A. Vicini, *Analytic Results for Virtual QCD Corrections to Higgs Production and Decay*, *JHEP* **01** (2007) 021 [hep-ph/0611266].

[235] C. Anastasiou, S. Beerli, S. Bucherer, A. Daleo and Z. Kunszt, *Two-loop amplitudes and master integrals for the production of a Higgs boson via a massive quark and a scalar-quark loop*, *JHEP* **01** (2007) 082 [hep-ph/0611236].

[236] S. Catani, L. Cieri, D. de Florian, G. Ferrera and M. Grazzini, *Diphoton production at hadron colliders: a fully-differential QCD calculation at NNLO*, *Phys. Rev. Lett.* **108** (2012) 072001 [1110.2375].

[237] S. Catani, L. Cieri, D. de Florian, G. Ferrera and M. Grazzini, *Diphoton production at the LHC: a QCD study up to NNLO*, *JHEP* **04** (2018) 142 [1802.02095].

[238] J. M. Campbell, R. K. Ellis, Y. Li and C. Williams, *Predictions for diphoton production at the LHC through NNLO in QCD*, *JHEP* **07** (2016) 148 [1603.02663].

[239] M. Grazzini, S. Kallweit and M. Wiesemann, *Fully differential NNLO computations with MATRIX*, *Eur. Phys. J.* **C78** (2018) 537 [1711.06631].

[240] L. Chen, *A prescription for projectors to compute helicity amplitudes in D dimensions*, 1904.00705.

[241] R. Karplus and M. Neuman, *The scattering of light by light*, *Phys. Rev.* **83** (1951) 776.

[242] Z. Bern, A. De Freitas, L. J. Dixon, A. Ghinculov and H. L. Wong, *QCD and QED corrections to light by light scattering*, *JHEP* **11** (2001) 031 [hep-ph/0109079].

[243] T. Binoth, E. W. N. Glover, P. Marquard and J. J. van der Bij, *Two loop corrections to light by light scattering in supersymmetric QED*, *JHEP* **05** (2002) 060 [hep-ph/0202266].

[244] Z. Bern and A. G. Morgan, *Massive loop amplitudes from unitarity*, *Nucl. Phys.* **B467** (1996) 479 [hep-ph/9511336].

[245] C. Bernicot, *Light-light amplitude from generalized unitarity in massive QED*, 0804.0749.

[246] M. Argeri, S. Di Vita, P. Mastrolia, E. Mirabella, J. Schlenk, U. Schubert et al., *Magnus and Dyson Series for Master Integrals*, *JHEP* **03** (2014) 082 [1401.2979].

[247] G. Luisoni, P. Nason, C. Oleari and F. Tramontano, *$HW^{\pm}$/HZ + 0 and 1 jet at NLO with the POWHEG BOX interfaced to GoSam and their merging within MiNLO*, *JHEP* **10** (2013) 083 [1306.2542].

[248] W. E. Caswell and G. P. Lepage, *Effective Lagrangians for Bound State Problems in QED, QCD, and Other Field Theories*, *Phys. Lett.* **167B** (1986) 437.

[249] G. T. Bodwin, E. Braaten and G. P. Lepage, *Rigorous QCD analysis of inclusive annihilation and production of heavy quarkonium*, *Phys. Rev.* **D51** (1995) 1125 [hep-ph/9407339].

[250] A. Pineda and J. Soto, *Effective field theory for ultrasoft momenta in NRQCD and NRQED*, *Nucl. Phys. Proc. Suppl.* **64** (1998) 428 [hep-ph/9707481].

[251] M. Beneke and V. A. Smirnov, *Asymptotic expansion of Feynman integrals near threshold*, *Nucl. Phys.* **B522** (1998) 321 [hep-ph/9711391].

[252] K. Melnikov, M. Spira and O. I. Yakovlev, *Threshold effects in two photon decays of Higgs particles*, *Z. Phys.* **C64** (1994) 401 [hep-ph/9405301].

[253] K. Melnikov and O. I. Yakovlev, *Top near threshold: All alpha-S corrections are trivial*, *Phys. Lett.* **B324** (1994) 217 [hep-ph/9302311].

[254] W. Fischler, *Quark - anti-Quark Potential in QCD*, *Nucl. Phys.* **B129** (1977) 157.

[255] A. Billoire, *How Heavy Must Be Quarks in Order to Build Coulombic q anti-q Bound States*, *Phys. Lett.* **92B** (1980) 343.

[256] M. Beneke, *A Quark mass definition adequate for threshold problems*, *Phys. Lett.* **B434** (1998) 115 [hep-ph/9804241].

[257] A. H. Hoang and T. Teubner, *Top quark pair production at threshold: Complete next-to-next-to-leading order relativistic corrections*, *Phys. Rev.* **D58** (1998) 114023 [hep-ph/9801397].

[258] M. Beneke, A. Signer and V. A. Smirnov, *A Two loop application of the threshold expansion: The Bottom quark mass from b anti-b production*, in *Radiative corrections: Application of quantum field theory to phenomenology. Proceedings, 4th International Symposium, RADCOR'98, Barcelona, Spain, September 8-12, 1998*, pp. 223–234, 1999, hep-ph/9906476.

[259] A. H. Hoang, A. V. Manohar, I. W. Stewart and T. Teubner, *The Threshold t anti-t cross-section at NNLL order*, *Phys. Rev.* **D65** (2002) 014014 [hep-ph/0107144].

[260] A. Petrelli, M. Cacciari, M. Greco, F. Maltoni and M. L. Mangano, *NLO production and decay of quarkonium*, *Nucl. Phys.* **B514** (1998) 245 [hep-ph/9707223].

[261] K. Hagiwara, Y. Sumino and H. Yokoya, *Bound-state Effects on Top Quark Production at Hadron Colliders*, *Phys. Lett.* **B666** (2008) 71 [0804.1014].

[262] Y. Kiyo, J. H. Kuhn, S. Moch, M. Steinhauser and P. Uwer, *Top-quark pair production near threshold at LHC*, *Eur. Phys. J.* **C60** (2009) 375 [0812.0919].

[263] A. H. Hoang and C. J. Reisser, *Electroweak absorptive parts in NRQCD matching conditions*, *Phys. Rev.* **D71** (2005) 074022 [hep-ph/0412258].

[264] Y. Kiyo, A. Pineda and A. Signer, *New determination of inclusive electromagnetic decay ratios of heavy quarkonium from QCD*, *Nucl. Phys.* **B841** (2010) 231 [1006.2685].

[265] J. Butterworth et al., *PDF4LHC recommendations for LHC Run II*, *J. Phys.* **G43** (2016) 023001 [1510.03865].

[266] S. Dulat, T.-J. Hou, J. Gao, M. Guzzi, J. Huston, P. Nadolsky et al., *New parton distribution functions from a global analysis of quantum chromodynamics*, *Phys. Rev.* **D93** (2016) 033006 [1506.07443].

[267] L. A. Harland-Lang, A. D. Martin, P. Motylinski and R. S. Thorne, *Parton distributions in the LHC era: MMHT 2014 PDFs*, *Eur. Phys. J.* **C75** (2015) 204 [1412.3989].

[268] NNPDF collaboration, R. D. Ball et al., *Parton distributions for the LHC Run II*, *JHEP* **04** (2015) 040 [1410.8849].

[269] A. Buckley, J. Ferrando, S. Lloyd, K. Nordström, B. Page, M. Rüfenacht et al., *LHAPDF6: parton density access in the LHC precision era*, *Eur. Phys. J.* **C75** (2015) 132 [1412.7420].

[270] J. Campbell and T. Neumann, *Precision Phenomenology with MCFM*, 1909.09117.

[271] ATLAS collaboration, G. Aad et al., *Electron and photon energy calibration with the ATLAS detector using LHC Run 1 data*, *Eur. Phys. J.* **C74** (2014) 3071 [1407.5063].

[272] CMS collaboration, V. Khachatryan et al., *Performance of Photon Reconstruction and Identification with the CMS Detector in Proton-Proton Collisions at sqrt(s) = 8 TeV*, *JINST* **10** (2015) P08010 [1502.02702].

[273] F. Caola, M. Dowling, K. Melnikov, R. Röntsch and L. Tancredi, *QCD corrections to vector boson pair production in gluon fusion including interference effects with off-shell Higgs at the LHC*, *JHEP* **07** (2016) 087 [1605.04610].

[274] G. Heinrich, S. Jahn, S. P. Jones, M. Kerner and J. Pires, *NNLO predictions for Z-boson pair production at the LHC*, *JHEP* **03** (2018) 142 [1710.06294].

[275] F. Cascioli, T. Gehrmann, M. Grazzini, S. Kallweit, P. Maierhöfer, A. von Manteuffel et al., *ZZ production at hadron colliders in NNLO QCD*, *Phys. Lett.* **B735** (2014) 311 [1405.2219].

[276] M. Grazzini, S. Kallweit and D. Rathlev, *ZZ production at the LHC: fiducial cross sections and distributions in NNLO QCD*, *Phys. Lett.* **B750** (2015) 407 [1507.06257].

[277] A. von Manteuffel and R. M. Schabinger, *A novel approach to integration by parts reduction*, *Phys. Lett.* **B744** (2015) 101 [1406.4513].

[278] T. Peraro, *Scattering amplitudes over finite fields and multivariate functional reconstruction*, *JHEP* **12** (2016) 030 [1608.01902].

[279] S. Abreu, F. Febres Cordero, H. Ita, B. Page and M. Zeng, *Planar Two-Loop Five-Gluon Amplitudes from Numerical Unitarity*, *Phys. Rev.* **D97** (2018) 116014 [1712.03946].

[280] J. M. Henn and B. Mistlberger, *Four-graviton scattering to three loops in $\mathcal{N} = 8$ supergravity*, 1902.07221.

[281] J. Klappert and F. Lange, *Reconstructing Rational Functions with* `FireFly`, 1904.00009.

[282] CMS collaboration, S. Chatrchyan et al., *Measurement of W^+W^- and ZZ production cross sections in pp collisions at sqrt(s) = 8 TeV*, *Phys. Lett.* **B721** (2013) 190 [1301.4698].

[283] CMS collaboration, V. Khachatryan et al., *Measurements of the* Z Z *production cross sections in the* 2l2ν *channel in proton–proton collisions at* $\sqrt{s} = 7$ *and* 8 TeV *and combined constraints on triple gauge couplings*, *Eur. Phys. J.* **C75** (2015) 511 [1503.05467].

[284] ATLAS collaboration, G. Aad et al., *Measurement of the ZZ Production Cross Section in pp Collisions at $\sqrt{s}$ = 13 TeV with the ATLAS Detector*, *Phys. Rev. Lett.* **116** (2016) 101801 [1512.05314].

[285] ATLAS collaboration, M. Aaboud et al., *Measurement of the ZZ production cross section in proton-proton collisions at $\sqrt{s} = 8$ TeV using the $ZZ \to \ell^-\ell^+\ell'^-\ell'^+$ and $ZZ \to \ell^-\ell^+\nu\bar{\nu}$ channels with the ATLAS detector*, *JHEP* **01** (2017) 099 [1610.07585].

[286] CMS collaboration, V. Khachatryan et al., *Measurement of the ZZ production cross section and $Z \to \ell^+\ell^-\ell'^+\ell'^-$ branching fraction in pp collisions at $\sqrt{s}$=13 TeV*, *Phys. Lett.* **B763** (2016) 280 [1607.08834].

[287] ATLAS collaboration, M. Aaboud et al., *$ZZ \to \ell^+\ell^-\ell'^+\ell'^-$ cross-section measurements and search for anomalous triple gauge couplings in 13 TeV pp collisions with the ATLAS detector*, *Phys. Rev.* **D97** (2018) 032005 [1709.07703].

[288] CMS collaboration, A. M. Sirunyan et al., *Measurements of the* pp $\to$ ZZ *production cross section and the* $\mathrm{Z} \to 4\ell$ *branching fraction, and constraints on anomalous triple gauge couplings at* $\sqrt{s} = 13$ *TeV*, *Eur. Phys. J.* **C78** (2018) 165 [1709.08601].

[289] ATLAS collaboration, *Search for heavy ZZ resonances in the* $\ell^+\ell^-\ell^+\ell^-$ *and* $\ell^+\ell^-\nu\bar{\nu}$ *final states using proton–proton collisions at* $\sqrt{s} = 13$ *TeV with the ATLAS detector*, Tech. Rep. ATLAS-CONF-2017-058, CERN, Geneva, Jul, 2017.

[290] CMS collaboration, A. M. Sirunyan et al., *Measurement of differential cross sections for Z boson pair production in association with jets at* $\sqrt{s} = 8$ *and 13 TeV*, *Phys. Lett.* **B789** (2019) 19 [1806.11073].

[291] J. Ohnemus and J. F. Owens, *An Order-*α_s *calculation of hadronic ZZ production*, *Phys. Rev.* **D43** (1991) 3626.

[292] B. Mele, P. Nason and G. Ridolfi, *QCD radiative corrections to Z boson pair production in hadronic collisions*, *Nucl. Phys.* **B357** (1991) 409.

[293] J. Ohnemus, *Hadronic ZZ,* W^-W^+*, and* $W^\pm Z$ *production with QCD corrections and leptonic decays*, *Phys. Rev.* **D50** (1994) 1931 [hep-ph/9403331].

[294] L. J. Dixon, Z. Kunszt and A. Signer, *Vector boson pair production in hadronic collisions at order* α_s *: Lepton correlations and anomalous couplings*, *Phys. Rev.* **D60** (1999) 114037 [hep-ph/9907305].

[295] D. A. Dicus, C. Kao and W. W. Repko, *Gluon Production of Gauge Bosons*, *Phys. Rev.* **D36** (1987) 1570.

[296] E. W. N. Glover and J. J. van der Bij, *Z boson pair production via gluon fusion*, *Nucl. Phys.* **B321** (1989) 561.

[297] T. Matsuura and J. J. van der Bij, *Characteristics of leptonic signals for Z boson pairs at hadron colliders*, *Z. Phys.* **C51** (1991) 259.

[298] C. Zecher, T. Matsuura and J. J. van der Bij, *Leptonic signals from off-shell Z boson pairs at hadron colliders*, *Z. Phys.* **C64** (1994) 219 [hep-ph/9404295].

[299] T. Binoth, N. Kauer and P. Mertsch, *Gluon-induced QCD Corrections to* $pp \to ZZ \to \ell\bar{\ell}\ell'\bar{\ell}'$, in *Proceedings, 16th International Workshop on Deep Inelastic Scattering and Related Subjects (DIS 2008): London, UK, April 7-11, 2008*, p. 142, 2008, 0807.0024, DOI: 10.3360/dis.2008.142.

[300] N. Kauer, *Interference effects for* $H \to WW/ZZ \to \ell\bar{\nu}_\ell\bar{\ell}\nu_\ell$ *searches in gluon fusion at the LHC*, *JHEP* **12** (2013) 082 [1310.7011].

[301] F. Cascioli, S. Höche, F. Krauss, P. Maierhöfer, S. Pozzorini and F. Siegert, *Precise Higgs-background predictions: merging NLO QCD and squared quark-loop corrections to four-lepton + 0,1 jet production*, *JHEP* **01** (2014) 046 [1309.0500].

[302] J. M. Campbell, R. K. Ellis and C. Williams, *Bounding the Higgs width at the LHC using full analytic results for* $gg \to e^- e^+ \mu^- \mu^+$, *JHEP* **04** (2014) 060 [1311.3589].

[303] N. Kauer, C. O'Brien and E. Vryonidou, *Interference effects for* $H \to W\,W \to \ell\nu q\overline{q}'$ *and* $H \to ZZ \to \ell\overline{\ell} q\overline{q}$ *searches in gluon fusion at the LHC*, *JHEP* **10** (2015) 074 [1506.01694].

[304] T. Binoth, T. Gleisberg, S. Karg, N. Kauer and G. Sanguinetti, *NLO QCD corrections to ZZ+ jet production at hadron colliders*, *Phys. Lett.* **B683** (2010) 154 [0911.3181].

[305] C. S. Li, H. T. Li, D. Y. Shao and J. Wang, *Soft gluon resummation in the signal-background interference process of* $gg(\to h^*) \to ZZ$, *JHEP* **08** (2015) 065 [1504.02388].

[306] T. Gehrmann, A. von Manteuffel, L. Tancredi and E. Weihs, *The two-loop master integrals for* $q\overline{q} \to VV$, *JHEP* **06** (2014) 032 [1404.4853].

[307] F. Caola, J. M. Henn, K. Melnikov and V. A. Smirnov, *Non-planar master integrals for the production of two off-shell vector bosons in collisions of massless partons*, *JHEP* **09** (2014) 043 [1404.5590].

[308] F. Caola, J. M. Henn, K. Melnikov, A. V. Smirnov and V. A. Smirnov, *Two-loop helicity amplitudes for the production of two off-shell electroweak bosons in quark-antiquark collisions*, *JHEP* **11** (2014) 041 [1408.6409].

[309] T. Gehrmann, A. von Manteuffel and L. Tancredi, *The two-loop helicity amplitudes for* $q\overline{q}' \to V_1 V_2 \to 4$ *leptons*, *JHEP* **09** (2015) 128 [1503.04812].

[310] A. von Manteuffel and L. Tancredi, *The two-loop helicity amplitudes for* $gg \to V_1 V_2 \to 4$ leptons, *JHEP* **06** (2015) 197 [1503.08835].

[311] F. Caola, J. M. Henn, K. Melnikov, A. V. Smirnov and V. A. Smirnov, *Two-loop helicity amplitudes for the production of two off-shell electroweak bosons in gluon fusion*, *JHEP* **06** (2015) 129 [1503.08759].

[312] S. Kallweit and M. Wiesemann, *ZZ production at the LHC: NNLO predictions for* $2\ell 2\nu$ *and* 4ℓ *signatures*, *Phys. Lett.* **B786** (2018) 382 [1806.05941].

[313] F. Caola, K. Melnikov, R. Röntsch and L. Tancredi, *QCD corrections to ZZ production in gluon fusion at the LHC*, *Phys. Rev.* **D92** (2015) 094028 [1509.06734].

[314] S. Alioli, F. Caola, G. Luisoni and R. Röntsch, *ZZ production in gluon fusion at NLO matched to parton-shower*, *Phys. Rev.* **D95** (2017) 034042 [1609.09719].

[315] E. Accomando, A. Denner and A. Kaiser, *Logarithmic electroweak corrections to gauge-boson pair production at the LHC*, *Nucl. Phys.* **B706** (2005) 325 [hep-ph/0409247].

[316] A. Bierweiler, T. Kasprzik and J. H. Kühn, *Vector-boson pair production at the LHC to $\mathcal{O}(\alpha^3)$ accuracy*, *JHEP* **12** (2013) 071 [1305.5402].

[317] J. Baglio, L. D. Ninh and M. M. Weber, *Massive gauge boson pair production at the LHC: a next-to-leading order story*, *Phys. Rev.* **D88** (2013) 113005 [1307.4331].

[318] S. Gieseke, T. Kasprzik and J. H. Kühn, *Vector-boson pair production and electroweak corrections in HERWIG++*, *Eur. Phys. J.* **C74** (2014) 2988 [1401.3964].

[319] B. Biedermann, *Full NLO electroweak corrections to Z-boson pair production at the Large Hadron Collider*, *PoS* **DIS2017** (2018) 168 [1707.01029].

[320] B. Biedermann, A. Denner, S. Dittmaier, L. Hofer and B. Jäger, *Electroweak corrections to $pp \to \mu^+\mu^- e^+ e^- + X$ at the LHC: a Higgs background study*, *Phys. Rev. Lett.* **116** (2016) 161803 [1601.07787].

[321] B. Biedermann, A. Denner, S. Dittmaier, L. Hofer and B. Jäger, *Next-to-leading-order electroweak corrections to the production of four charged leptons at the LHC*, *JHEP* **01** (2017) 033 [1611.05338].

[322] S. Kallweit, J. M. Lindert, S. Pozzorini and M. Schönherr, *NLO QCD+EW predictions for $2\ell 2\nu$ diboson signatures at the LHC*, *JHEP* **11** (2017) 120 [1705.00598].

[323] M. Chiesa, A. Denner and J.-N. Lang, *Anomalous triple-gauge-boson interactions in vector-boson pair production with RECOLA2*, *Eur. Phys. J.* **C78** (2018) 467 [1804.01477].

[324] M. Grazzini, S. Kallweit, M. Wiesemann and J. Y. Yook, *ZZ production at the LHC: NLO QCD corrections to the loop-induced gluon fusion channel*, *JHEP* **03** (2019) 070 [1811.09593].

[325] K. Melnikov and M. Dowling, *Production of two Z-bosons in gluon fusion in the heavy top quark approximation*, *Phys. Lett.* **B744** (2015) 43 [1503.01274].

[326] J. M. Campbell, R. K. Ellis, M. Czakon and S. Kirchner, *Two loop correction to interference in $gg \to ZZ$*, *JHEP* **08** (2016) 011 [1605.01380].

[327] R. Gröber, A. Maier and T. Rauh, *Top quark mass effects in $gg \to ZZ$ at two loops and off-shell Higgs interference*, 1908.04061.

[328] A. Denner and T. Sack, *Electroweak radiative corrections to $e^+e^- \to Z^0Z^0$*, *Nucl. Phys.* **B306** (1988) 221.

[329] K. P. O. Diener, B. A. Kniehl and A. Pilaftsis, *Loop effects of exotic leptons on vector boson pair production at e+ e- colliders*, *Phys. Rev.* **D57** (1998) 2771 [hep-ph/9709361].

[330] I. Moult, L. Rothen, I. W. Stewart, F. J. Tackmann and H. X. Zhu, *Subleading Power Corrections for N-Jettiness Subtractions*, *Phys. Rev.* **D95** (2017) 074023 [1612.00450].

[331] C. W. Bauer, S. Fleming and M. E. Luke, *Summing Sudakov logarithms in $B \to X_s\gamma$ in effective field theory*, *Phys. Rev.* **D63** (2000) 014006 [hep-ph/0005275].

[332] C. W. Bauer, S. Fleming, D. Pirjol and I. W. Stewart, *An Effective field theory for collinear and soft gluons: Heavy to light decays*, *Phys. Rev.* **D63** (2001) 114020 [hep-ph/0011336].

[333] C. W. Bauer and I. W. Stewart, *Invariant operators in collinear effective theory*, *Phys. Lett.* **B516** (2001) 134 [hep-ph/0107001].

[334] C. W. Bauer, D. Pirjol and I. W. Stewart, *Soft collinear factorization in effective field theory*, *Phys. Rev.* **D65** (2002) 054022 [hep-ph/0109045].

[335] J. R. Gaunt, M. Stahlhofen and F. J. Tackmann, *The Quark Beam Function at Two Loops*, *JHEP* **04** (2014) 113 [1401.5478].

[336] R. Kelley, M. D. Schwartz, R. M. Schabinger and H. X. Zhu, *The two-loop hemisphere soft function*, *Phys. Rev.* **D84** (2011) 045022 [1105.3676].

[337] P. F. Monni, T. Gehrmann and G. Luisoni, *Two-Loop Soft Corrections and Resummation of the Thrust Distribution in the Dijet Region*, *JHEP* **08** (2011) 010 [1105.4560].

[338] F. Campanario, M. Kerner, L. D. Ninh and D. Zeppenfeld, *Next-to-leading order QCD corrections to ZZ production in association with two jets*, *JHEP* **07** (2014) 148 [1405.3972].

[339] A. D. Martin, W. J. Stirling, R. S. Thorne and G. Watt, *Update of parton distributions at NNLO*, *Phys. Lett.* **B652** (2007) 292 [0706.0459].

[340] R. Boughezal, J. M. Campbell, R. K. Ellis, C. Focke, W. Giele, X. Liu et al., *Color singlet production at NNLO in MCFM*, *Eur. Phys. J.* **C77** (2017) 7 [1605.08011].

[341] R. Boughezal, X. Liu and F. Petriello, *Power Corrections in the N-jettiness Subtraction Scheme*, *JHEP* **03** (2017) 160 [1612.02911].

[342] I. Moult, L. Rothen, I. W. Stewart, F. J. Tackmann and H. X. Zhu, *N-jettiness subtractions for $gg \to H$ at subleading power*, *Phys. Rev.* **D97** (2018) 014013 [1710.03227].

Acknowledgments

I would like to thank the following people for their support and encouragement which made my time at the Max Planck Institute both productive and enjoyable:

Gudrun Heinrich for guidance and support in all matters concerning the PhD project, introduction to the phenomenology community.

Professor Hollik for providing me the opportunity to conduct my research in the phenomenology group at the Max Planck Institute for Physics and Johannes Henn as well as Giulia Zanderighi for continued support of this PhD project after Professor Hollik's retirement. Professor Hollik for useful discussions and suggestions concerning this Thesis. The members of my advisory panel Gudrun Heinrich, Professor Hollik, and Stefan Kluth.

The SecDec collaboration, Sophia Borowka, Gudrun Heinrich, Stephen Jones, Matthias Kerner, Florian Langer, Andres Põldaru, Johannes Schlenk, Tom Zirke, and the GoSam collaboration, Mauro Chiesa, Nicolas Greiner, Gudrun Heinrich, Stephen Jones, Matthias Kerner, Gionata Luisoni, Pierpaolo Mastrolia, Giovanni Ossola, Tiziano Peraro, Johannes Schlenk, Ludovic Scyboz, Francesco Tramontano, for successful teamwork. I also want to thank Hiroshi Yokoya for the collaboration concerning the diphoton project. Special thanks also to Ben Ruijl for the help with finding problems in a preliminary implementation of Pak's sorting (see Section 4.5).

Thomas Hahn for support with the computing facilities of the theory group. Oliver Schulz on behalf of the GERDA group for kindly allowing us to use their GPU servers and especially Oliver for fruitful discussions.

Current and former members of the phenomenology and the amplitudes group, Henning Bahl, Thomas Hahn, Nicolas Greiner, Stephan Hessenberger, Stephen Jones, Matthias Kerner, Daniele Lombardi, Gionata Luisoni, Viktor Papara, Cyril Pietsch, Joao Pires, Sorana Scholtes, Ulrich Schubert, Ludovic Scyboz, Johann-Felix Graf von Soden-Fraunhofen, Jan Winter, Tom Zirke, Taushif Ahmed, Matteo Capozi, Long Chen, Dimitrii Chicherin, Christoph Dlapa, Gudrun Heinrich, Leila Maestri, Kai Yan, Yang Zhang, and Simone Zoia for helpful discussions and a great working environment.

The theory secretaries Sarah Fischer, Monika Goldammer, Rosita Jurgeleit, and Anette Moessinger, as well as the administrative staff, particularly Corina Brunnlechner, Clemens Drab, Dieter Fischer, Karin Gebhardt, and Jana Pietsch for assistance in many organisational matters.

My office mates Matthias Kerner and Amando Hala for many interesting and helpful discussions.

Thomas Hahn, Stefan Kluth, Raphael Kneißl, and Stefan Stonjek for useful discussions and entertaining coffee breaks.

I am grateful to have been able to take part in the curriculum of the International Max Planck Research School (IMPRS) on Elementary Particle Physics. It was a pleasure to take part in the active social life of the institute.

Finally, I want to acknowledge the infinite support of my family. This Thesis would never have been written without it.